STUDIA UNIVERSITATIS
BABEŞ-BOLYAI

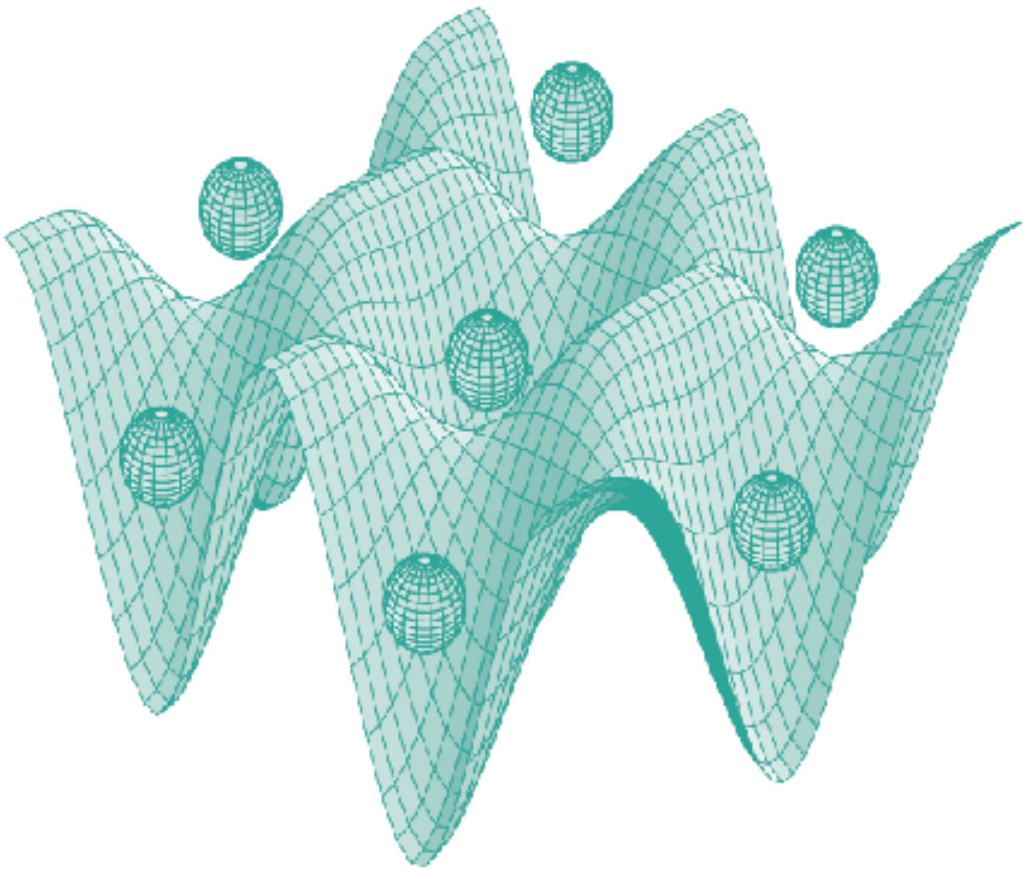

PHYSICA

2/2008

ANUL LIII **2008**

S T U D I A

UNIVERSITATIS BABEŞ–BOLYAI

PHYSICA

2

Desktop Editing Office: 51st B.P. Hasdeu Street, Cluj-Napoca, Romania, phone + 40 264 405352

SUMAR - SOMMAIRE - CONTENTS - INHALT

STUDIA UNIVERSITATIS BABEŞ-BOLYAI, PHYSICA, LIII, 2, 2008

EPR STUDY OF RADIATION INDUCED PARAMAGNETIC SPECIES IN ALUMINOSILICATE COMPOUNDS

EMILIA S. VANEA, V. SIMON*

ABSTRACT. Electron paramagnetic resonance (EPR) spectroscopy was used to characterize paramagnetic centres occurring in gamma ray irradiated aluminosilicate systems containing rare earth and/or iron that may be used for biomedical applications. The investigated samples were obtained following the sol-gel route. After drying at 110°C the samples were heat-treated at 500°C or 1200°C. Usually the sterilisation of such biomedical compounds is realized with gamma rays. For this reason the samples were gamma irradiated and investigated with respect to possible occurrence of nocuous irradiation effects. The EPR studies demonstrate that various radiation-induced defects, like surface defects and peroxy-centres, are present in the analysed systems. A higher concentration of defects was detected for samples treated at 500°C, as compared to samples treated at 1200°C.

Key words: aluminosilicate compounds; gamma irradiation; paramagnetic centres; EPR.

1. Introduction

Glass systems are very often used as bone repairing and substituting materials in many dental and orthopedic applications due to their excellent biocompatibility and osteointegration [1]. Aluminosilicate systems containing radioactivable isotopes like yttrium, dysprosium, samarium or rhenium are of interest for in situ radiotherapy [2]. Aluminosilicate glass microspheres containing radioactive yttrium are currently employed with success to treat liver cancer. Aluminosilicate glasses containing holmium were tested in human mammary carcinoma [3] and glass microspheres with praseodim are considered to treat kidney diseases and save health tissues from undesirable exposure to high dose radiation [4].

Moreover, the simultaneous application of radiotherapy and hyperthermia considerably enhances the therapeutic effects of the two cancer treatment methods [5]. The addition of iron oxides can introduce a ferrimagnetic phase proper for local heating by magnetic hysteresis. To reduce the risk of infections and associated complications it is necessary to sterilize all medical implants after fabrication and prior to their use t [6, 7]. Despite the availability of a wide range of sterilisation techniques, it is generally agreed that no single sterilisation process is capable of sterilising without adverse effects, all processes having their own advantages and disadvantages [8-10]. Radiation sterilisation utilises ionising radiation, using either

* *Babes-Bolyai University, Faculty of Physics & Institute for Interdisciplinary Experimental Research, Cluj-Napoca, Romania. Corresponding author: viosimon@phys.ubbcluj.ro*

gamma rays from a cobalt-60 (^{60}Co) isotope source or accelerated electrons. Gamma irradiation is the most popular form of radiation sterilisation, the capability of ionising radiation to kill microorganisms being established early in the past century [11]. This method is a very easy, rapid and efficient sterilization way, but as every sterilization method, has its own inconvenient.

This article briefly describes the gamma irradiation effects on aluminosilicate compounds of biomedical interest for sterilisation purpose. In the present work we report the studies of paramagnetic defect centres in silica–based sol-gel materials that were produced at room temperature containing rare earth (yttrium or dysprosium) and iron. A promising technique that can be used to describe and explain the radiation-induced paramagnetic centres is the Electron Paramagnetic Resonance (EPR).

2. Materials and Methods

The composition of the investigated aluminosilicate systems is given in Table 1.

Table 1

Sample composition

Code	Components (mol %)				
	SiO_2	Al_2O_3	Fe_2O_3	Dy_2O_3	Y_2O_3
S1	60	20	20		
S2	60	20	10	10	
S3	60	20	10		10

The compounds were synthesized by means of sol-gel method using as starting materials silica acid and aluminium, iron, yttrium and dysprosium nitrates. After the gel formation, the samples were filtrated, dried at 110ºC for couple of hours and then heat-treated at 500°C for one hour and 1200°C for 24 hours, respectively. In order to check the bioactivity, an amount of each sample was immersed in simulated body fluid (SBF) for forty days at 37 °C. Both unimmersed and SBF immersed samples were exposed to gamma rays for a few weeks, using a ^{60}Co source with a debit dose of 10 Gy/h. The irradiation dose was close to 8 kGy. Electron resonance spectra of the sol-gel materials were recorded by means of EPR spectrometer, ADANI type, operating at 9.4 GHz (X band). The magnetic field was modulated at 100 KHz and the spectra were displayed as the first derivate of the absorption curve. All spectra were recorded at room temperature.

3. Results and discussions

The EPR spectra of the examined aluminosilicate compounds are presented in Figure 1.

Various radiation-induced defects like surface defects and peroxy-centres are present in the analysed systems [12]. The description of radiation-induced centres in amorphous silica based materials according to notation given by Ikeya [13] will be used in our further considerations (Table 2).

Table 2

Possible defects observed by EPR in silica based materials [12, 13]

E_1' centres	≡Si•Si≡ Electron trapped in the oxygen vacancy	g = 2.00179; 2.00053; 2.00030
Oxygen hole centre (OHC)	≡SI–O–(–O •)–Si≡ Interstitial oxygen ion O^- bonds whit O^{2-}	g = 2.0014; 2.0074; 2.023
Nonbonding oxygen hole centre (NBOHC)	≡Si–O • Proton is released from Si-OH and a hole is trapped at the remaining oxygen	g = 2.004; 2.008; 2.021

Beside the typical Fe^{3+} EPR lines (at $g_{eff} \approx 4.3$ corresponding to the isolated Fe^{3+} ion and at $g_{eff} \approx 2$ attributed to the Fe^{3+} species that participate to dipole-dipole interactions), additional signals occurring from paramagnetic defects were detected mainly for 110°C dried and 500°C heat-treated samples (Fig. 1 a, b). For the crystallised samples resulted after the heat treated applied at 1200°C (Fig. 1 c, d) the EPR spectra reveal a very weak signal at $g_{eff} \approx 2.01$ due to a low number of lattice defects associated with oxygen or cation vacancies, that denotes a very good stability of the crystalline compounds. The analysis indicates that for the samples treated at 500°C the defects concentration is meaningful greater than for the samples treated at 1200°C.

The most important and studied radiation-induced point defects in amorphous silicon dioxide (SiO_2) are the E' centres [14], arising from the hyperfine interaction of the unpaired electron with a ^{29}Si nucleus (nuclear spin I=1/2) [15]. Under irradiation the peroxy radical can convert to an E' centre due to irradiation-induced release of oxygen [16, 17]. E' centres cannot be detected by EPR because of saturation even at very low power microwaves (0.01 mW) [13]. Regarding the g factor (Fig.1 b, f) of the samples treated at 500°C, the presence of peroxy-centres, OHC ($g_1 \approx 2.037$) and NBOHC ($g_2 \approx 2.02$; $g_3 \approx 2.0179$; $g_4 \approx 2.009$) can be assumed in good agreement with the results obtained before (Table 2). For the samples treated at 1200°C the radiation induced defects cannot be showed by EPR, explaining the very good stability of the crystalline compounds. The immersion in SBF doesn't influence the presence of defects in radiation-exposed materials (Fig.1 e-h).

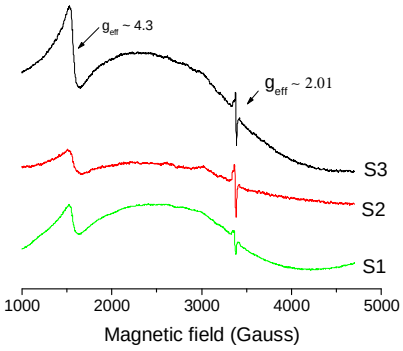
g_{eff} ~ 4.3
g_{eff} ~ 2.01
S3
S2
S1
1000
2000
3000
4000
5000
Magnetic field (Gauss)

a

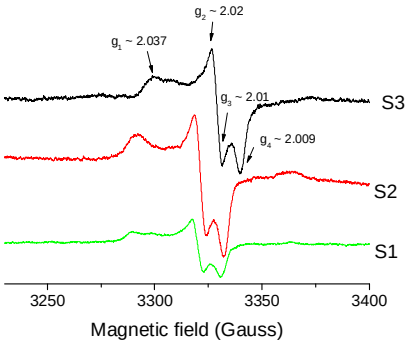
g_2 ~ 2.02
g_1 ~ 2.037
g_3 ~ 2.01
g_4 ~ 2.009
S3
S2
S1
3250
3300
3350
3400
Magnetic field (Gauss)

b

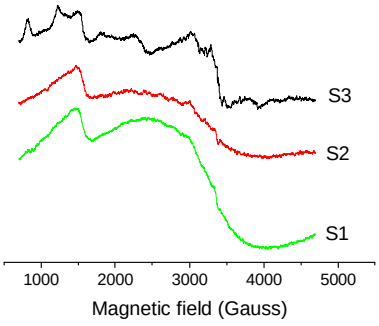
S3
S2
S1
1000
2000
3000
4000
5000
Magnetic field (Gauss)

c

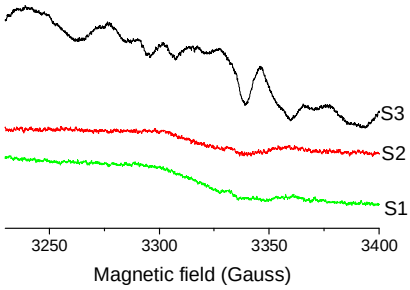
S3
S2
S1
3250
3300
3350
3400
Magnetic field (Gauss)

d

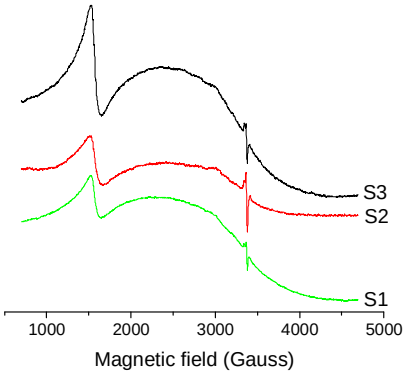
S3
S2
S1
1000
2000
3000
4000
5000
Magnetic field (Gauss)

e

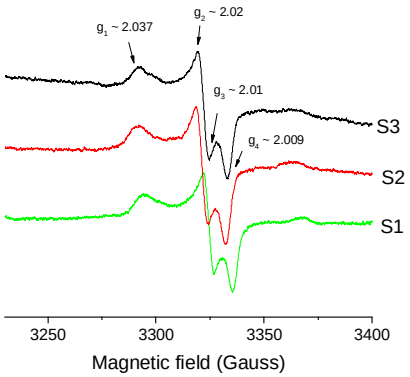
g_2 ~ 2.02
g_1 ~ 2.037
g_3 ~ 2.01
g_4 ~ 2.009
S3
S2
S1
3250
3300
3350
3400
Magnetic field (Gauss)

f

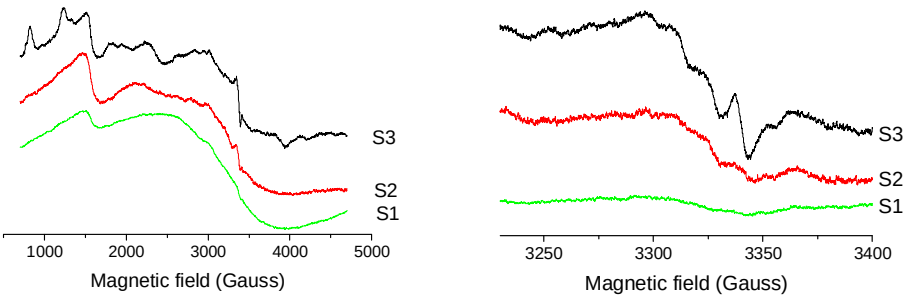

g h

Figure 1. The EPR spectra recorded, after gamma irradiation, of the samples heat-treated at 500°C before (a, b) and after SBF immersion (e, f) and at 1200°C before (c, d) and after SBF immersion (g, h).

4. Conclusions

The effect of gamma irradiation on new biomedical aluminosilicate compounds was investigated. The exposure to gamma rays was selected on the basis of the premise of using this technique for sterilisation purpose. The number of defects in aluminosilicate compounds, which can be responsible for cytotoxicity, depends on the sample structure. The samples treated at 500°C the defects concentration is meaningful greater than for the samples treated at 1200°C, denoting that the greater the crystallisation degree the better the stability of the irradiated samples against the occurrence of radiation defects. There is no difference concerning the EPR line shape for the samples category that was immersed in SBF before gamma exposure. The EPR spectroscopy was exploited as a suitable method for searching the defects responsible for cytotoxicity in the materials tested.

REFERENCES

[1]. I. D. Xynos, A. I. Edgar, L. D. K. Buttery, L. L. Hench, J. M. Polak, J. Biomed. Mater. Res, 55, 151 (2001).
[2]. J.E. White, D.E. Day, Key Eng. Mat., 94-95, 181 (1994)
[3]. R.F. Brown, L.C. Lindesmith, D.E. Day, Int. J. Rad. Appl. Instrum B, 18, 783 (1991)
[4]. S.W. Lee, W.D. Reece, Phys. Med. Biol., 50, 151 (2005)

[5]. M. Kawashita, H. Takaoka, T. Kokubo, T. Yao, S. Hamada, T. Shinjo, J. Ceram. Soc. Jpn., 109, 39 (2001)
[6]. J. M. Anderson, B. Bevacqua, A. N. Cranin, D. Whittlesey, Implants and Devices in Biomaterials Science, Academic Press, London, 1996, p. 415–420
[7] M. Baciut, G. Baciut, V. Simon, C. Albon, V. Coman, P. Prodan, St. I. Florian, S. Bran, J. Optoelectr. Adv. Mat., 9, 2547 (2007)
[8]. M. Goldman, L. Pruitt, J. Biomed Mater Res., 40, 378 (1998)
[9]. E. M. Noah, J. Chen, X. Jiao, I. Heschel, N. Pallua, Biomaterials. 23, 2855 (2002)
[10]. M. Takechi, Y. Miyamoto, Y. Momota, T. Yuasa, S. Tatehara, M. Nagayama, K. Ishikawa, J. Biomed. Mater. Res. B Appl Biomater., 69, 58 (2004)
[11]. J. W. Dorpema, Radiat. Phys. Chem., 35, 357 (1990).
[12]. D. Cacaina, H. Ylänen, D. A. Udvar, S. Simon, J. Optoelectr. Adv. Mater., 9, 675 (2007)
[13]. M. Ikeya, New Applications of Electron Spin Resonance: Dating, Dosimetry and Microscopy, World Scientific Publ., Singapore, 1993.
[14]. D.L. Griscom, in Defects in SiO_2 and related dielectrics: Science and Technology, Eds. G. Pacchioni, L. Skuja and D.L. Griscom, Kluwer Academic Publishers, 2000, p. 117.
[15]. D. L. Griscom, Nucl. Instrum. Methods Phys. Res. B 1, 481 (1984)
[16]. L. Zhang, V. A. Mashkov, R. G. Leisure, Phys. Rev. Lett. 74, 9, 1605, (1995)
[17]. G. Buscarino, S. Agnello, F. M. Gelardi, J. Non-Cryst. Solids, 351, 1787 (2005).

STUDIA UNIVERSITATIS BABEŞ-BOLYAI, PHYSICA, LIII, 2, 2008

THERMAL INVESTIGATION OF NANOCRYSTALLINE BONE PHASES

M. TĂMĂŞAN[1], S. SIMON[1], M. BĂCIUŢ[2], G. BĂCIUŢ[2], V. COMAN[3], V. SIMON[1]

ABSTRACT. The present study was carried out with the intention of thermally analyse bone samples of different origins and of determining heat treatment temperatures proper for developing a method to obtain hydroxyapatite (HAP) powder usable for biomedical applications. Bones studied here were deer antler, human skull, cattle, pig, fish, hen and turkey. The results show that the removal of the organic matrix can be achieved by heat treatments applied above 500^{o}C. At the same time it was evidenced that the organic matrix has sensibly different content in the investigated samples, depending on the bone nature.

Keywords: DTA, DSC, natural hydroxyapatite.

Introduction

The study of the effect of heat treatment on different types of bones has been a constant preoccupation of many researchers, since the calcined bone can be used as an osteoreproductive biomaterial for filling osteal defects [1-5]. The X-ray diffraction [1] and electron microscopy data [3] reveal that both the microstructure (crystallite size and microstrain) and the ultrastructure (inherent tissue architecture) are not altered by heat treatment at 400-500°C. Heating a bone at temperatures above 500°C causes complete destruction and removal of organic components [3, 6-8]. Further heating, over 600 to 700°C, leads to recrystallisation of the bone mineral by a rapid growth of bioapatite nanocrystals and disappearance of structural distortions [1, 9].

Hydroxyapatite (HAP) is one of the inorganic components of the hard tissues such as bones and teeth. HAP is a calcium phosphate-based bioceramic ($Ca_{10}(PO_4)_6(OH)_2$), and has been used in medicine and dentistry because of its excellent biocompatibility with human tissue [1]. HAP is known to be bioactive, osteoconductive, non-toxic, non-inflammatory and non-immunogenic agent [10, 11]. Considering the numerous application of HAP in biomedical fields, various synthesis techniques have been developed [12].

[1] *Babeş Bolyai University, Faculty of Physics and Institute for Interdisciplinary Experimental Research, 400084 Cluj-Napoca, Romani*
[2] *Iuliu Haţieganu University of Medicine and Pharmacy, Department of Cranio-Maxillofacial Surgery, 400029 Cluj-Napoca, Romania*
[3] *Raluca Ripan Institute for Research in Chemistry, 400294 Cluj-Napoca, Romania*

Previous X-ray diffraction (XRD) analyses carried out on untreated and heat-treated powdered bones [14] indicate an apparent similarity concerning the structure of the non-treated bone samples; a weak narrowing of all diffraction peaks for 500ºC treated samples was observed as an effect of increasing of the crystallinity of the samples. After 2 hours of heat treatment at 1200^{o}C the bone architecture was plenty affected, the inorganic phase of the bones is now organised in a well-defined crystalline structure similar to that of the pure mineral hydroxyapatite.

The surface morphology of the samples, previously analyzed by scanning electron microscopy [15], is different for the bones with different origins; the deer antler shows high porosity and fibrousity, which can be easily correlated with its properties of fast and complete regeneration. The microstructure of untreated bones is characterized by large pores and seems to be fibrous. High porosity is generally accepted to influence faster resorption in biomaterials transplanted in vital bone for defect reconstruction. It is also a favourable parameter of a biomaterial for promoting osteoconduction in living bone.

As a complementary study, the present investigation was made with the intention to thermally analyse bone samples of different origins and to determine heat treatment temperatures proper for developing a method to obtain hydroxyapatite using as primary material natural bones.

Experimental

The bone samples studied in this work originate from deer antler, human skull, cattle, pig, fish, hen and turkey. The study is a part of a greater research focused on the remarkable properties of the deer antler, which has a unique natural mode of rapid and complete bone regeneration.

The bones were deproteinated for use in osteoimplantation by a first degreasing with acetone for 48 h and with ethylic ether for 30 min and then by heating at 40ºC in the oven until the complete removal of the solvent. This was the initial batch of samples analyzed.

Because differential thermal analysis (DTA) combined with thermogravimetry (TG) is a reliable technique in the study of biomaterials and is often used in the structural characterization of different nanostructured materials [13], in order to establish the thermal stability of the bones we investigate them by differential thermal analyses DTA/TG and DSC methods. The measurements were carried out on Shimadzu type derivatographs DTG-60H (differential thermal and thermo gravimetric analyses) and DSC-60 (differential scanning calorimeter). The heating rate for DCS runs is 10ºC/min on a temperature range of 25-500º, while DTA/TG analysis was performed with a heating rate of 10ºC/min for a temperature range of 25-1200ºC. Alumina open crucibles were used for DTA/TG analysis and aluminium open crucibles for the DSC analyses. The measurements were made in a dynamic nitrogen and air atmosphere at a flow rate of 70ml/min each.

Results and discussion

The profile of the DSC plots of as prepared samples (Fig. 1) reveal at ~70ºC a small endothermic peak and a major exothermic peak at ~350ºC, followed by a smaller one at ~450ºC (except for the fish bone, which does not present the small exothermic peak). The first endothermic peak is related with the dehydration process (mostly water molecules removed from surfaces of the samples), while the exothermic events are related with the degradation and the combustion of the organic phase of the bones.

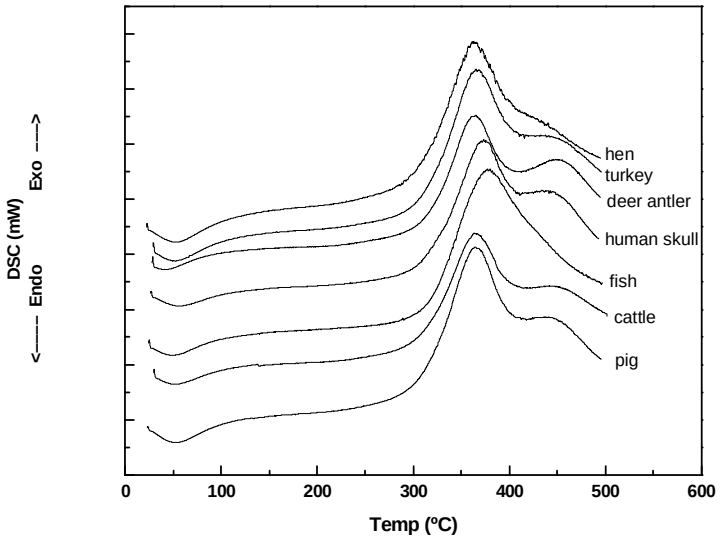

Fig. 1. DSC curves of bone samples of different origins (pig, cattle, fish, human skull, deer antler, turkey, hen)

Complementary analyses DTA/TG (differential thermal analysis/thermogravimetry) are to be seen in Figures 2 – 8. With the aid of thermogravimetric plot we can evaluate the content of the surface water and the organic content in each type of bone, by means of mass loss analysis. The calculation of the loss of mass which accompanied each event – the evaporation of the condensation water and the degradation of the organic phase of the bone (for all the samples except the fish one being a two-step process, one of degradation and one of combustion) – was represented in Table 1. These results are in good agreement with the supposition that around one third of bone is composed of organic compounds, of which 90 to 95% is collagen, the rest being non-collagenous proteins. Collagen is a fibrous protein that provides the bone with strength and flexibility. Due to its excellent biocompatibility with human tissue, the natural hydroxyapatite, resulting after heat

treatments applied on bones at temperatures higher than those corresponding to organic matrix removal, is a potential source for bone grafting, already used in dental implants, orthopaedics and maxilofacial surgery.

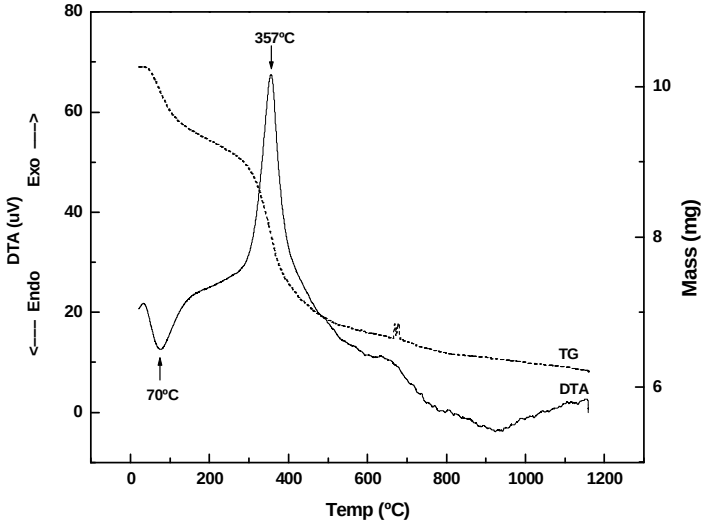

Fig. 2. DTA/TG plots of hen bone

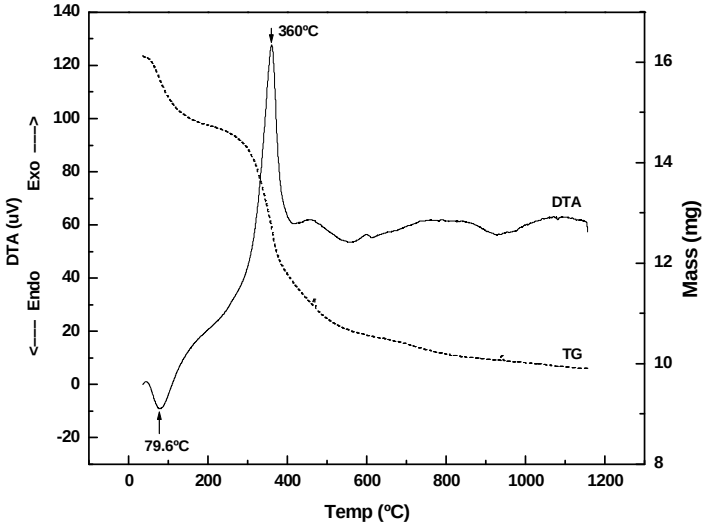

Fig. 3. DTA/TG plots of turkey bone

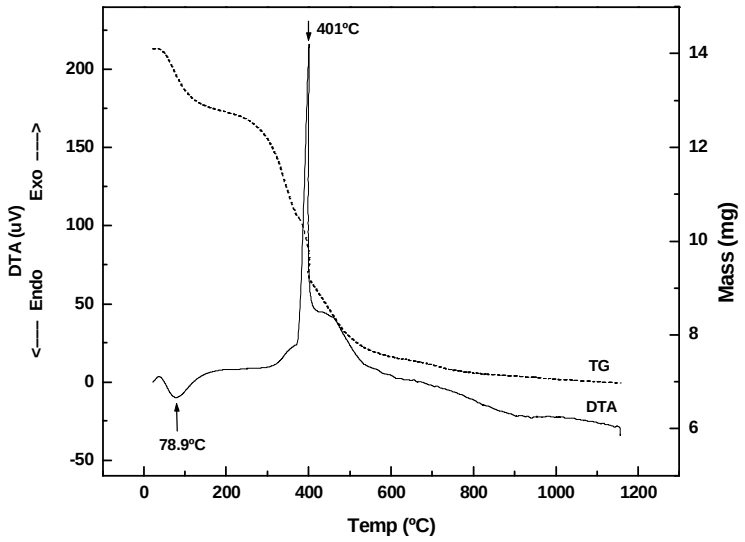

Fig. 4. DTA/TG plots of deer antler

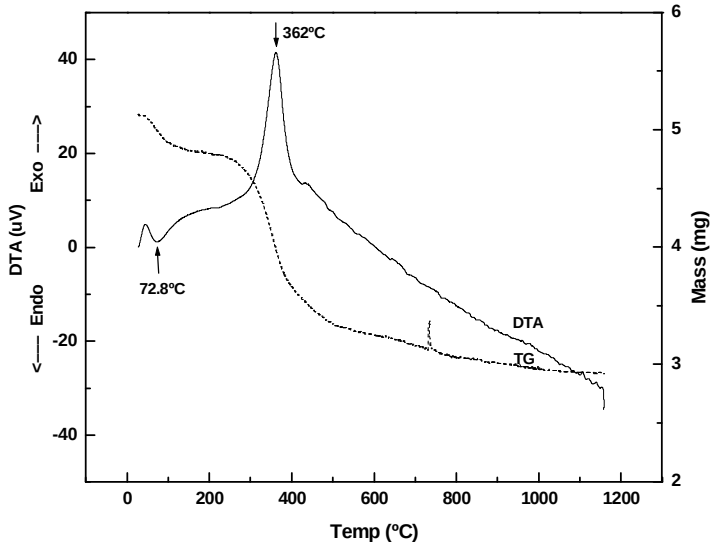

Fig. 5. DTA/TG plots of human skull bone

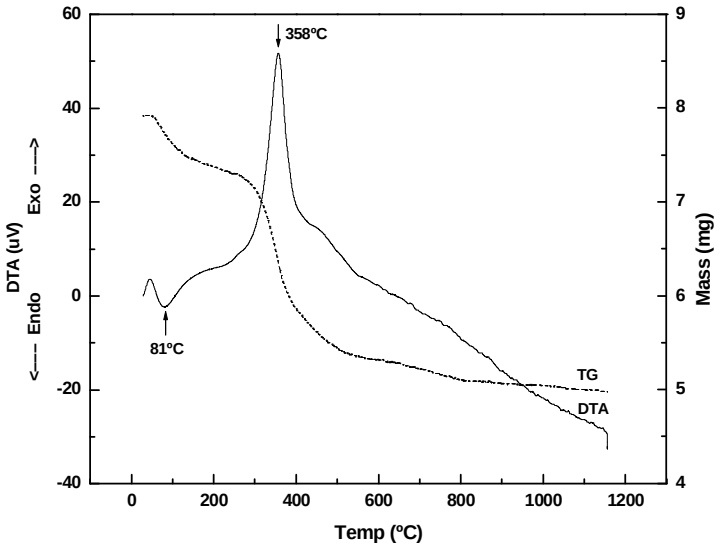

Fig. 6. DTA/TG plots of cattle bone

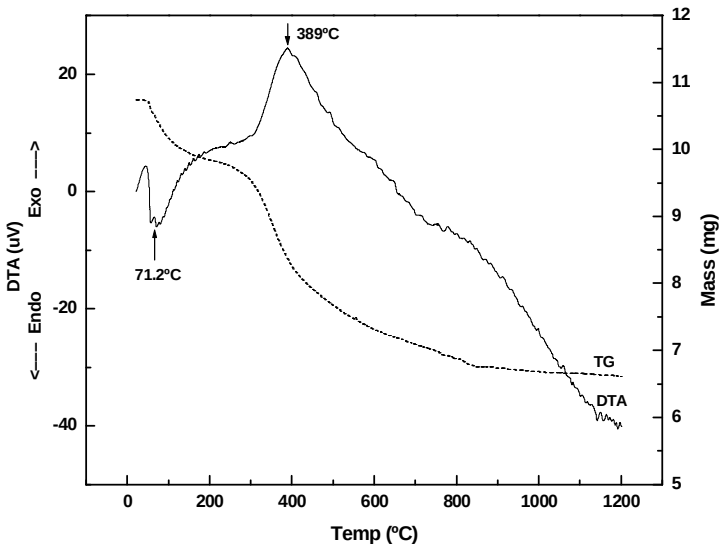

Fig. 7. DTA/TG plots of pig bone

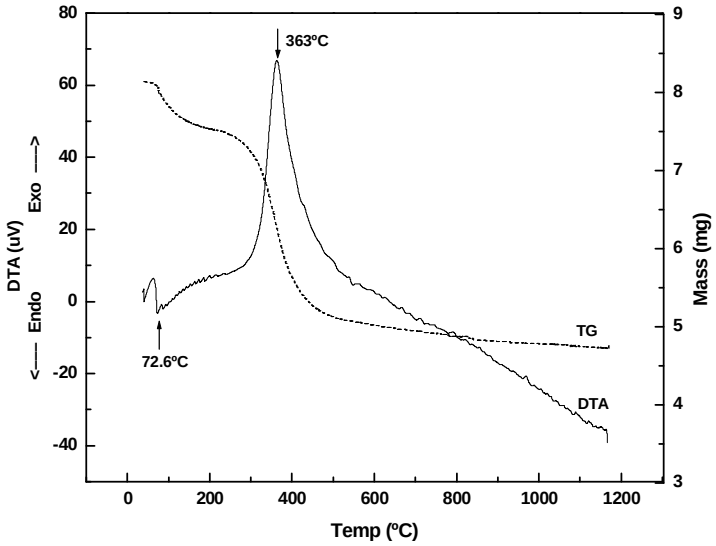

Fig. 8. DTA/TG plots of fish bone

Table 1

Peak temperatures and mass losses evaluated from TG plot

Sample	**Peak I**		**Mass loss I (%)**	**Peak II**		**Mass loss II (%)**
	Type	T_{peak} (ºC)		Type	T_{peak} (ºC)	
deer antler	endo	78.9	9.58	exo	401	33.74
cattle		81	7.05		358	24.26
pig		71.2	6.2		389	26.17
human skull		72.8	5.2		362	30.3
fish		72.6	6.5		363	30.15
turkey		79.6	8.07		360	27.1
hen		70	8.8		357	21

Conclusions

Differential thermal analyses combined with thermogravimetry results obtained for the investigated bone samples indicate that the dehydration of the surface attached water molecules takes place around 70ºC. The organic phase of the bones suffers degradation and combustion processes in the temperature range of 300-500ºC. The DCS and DTA data apparently show that bone samples of different origin have a similar thermal behaviour, but complementary TG diagrams reveal differences with respect to the content of organic matter. The deer antler, human skull and fish bones contain over 30 % organic matter, while in the other bones this content is about 21 - 27%.

Acknowledgments

The study was supported by the scientific research project CEEX 73 / 2006 of the Romanian Excellence Research Program.

REFERENCES

1. K. D. Rogers, P. Daniels, Biomaterials, 23, 2577 (2002)
2. J. C. Hiller, T.J.U. Thompson, M.P. Evison, A.T. Chamberlain, T.J. Wess, Biomaterials, 24, 5091 (2003)
3. S. Guizzardi, M. Raspanti, D. Martini, R. Scandroglio, P. Govoni, A. Ruggeri, Biomaterials, 15, 433 (1994)
4. S. Guizzardi, C. Montanari, S. Migliaccio, R. Strochi, R. Solmi, D. Martini, A. Ruggeri, J. Biomed Mater. Res. (Appl. Biomater.) 53, 227 (2000)
5. D. Tadic, M. Epple, Biomaterials 25, 987 (2004)
6. R. Legros, N. Balmain, G. Bonel, J. Chem. Res. (S), 8 (1986)
7. F. Peters, K. Schwarz, M. Epple, Thermochimica Acta 361, 131 (2000)
8. L. D. Mkukuma, J. M. S. Skakle, I. R. Gibson, C. T. Imrie, R. M. Aspden, D. W. L. Hukins, Calcif. Tissue Int. 75, 321 (2004)
9. S. N. Danilchenko, V. A. Pokrovskiy, V. M. Bogatyrov, L. F. Sukhodub, B. Sulkio-Cleff, Cryst. Res. Technol. 40, 692 (2005)
10. L. L. Hench, J. Wilson, Science, 226, 630 (1984)
11. J. Currey, Nature, 414, 699 (2001)
12. K. Prabakaran and S. Rajeswari, Trends Biomater. Artif. Organs, 20, 20 (2006)
13. B. S. Vasile, C. Ghitulica, N. Popescu-Pogrion, S. Constantinescu, I. Mercioniu, R. Stan, E. Andronescu, J. Optoelectr. Adv. Mater., 9, 3774 (2007)
14. S. Simon, H. Mocuta, M. Băciuţ, G. Băciuţ, V. Coman, P. Prodan, Şt. I. Florian, Studia, Physica, LII, 2, 63-69 (2007)
15. M. Băciuţ, G. Băciuţ, V. Simon, C. Albon, V. Coman, P. Prodan, Şt. I. Florian, S. Bran, J. Optoelectr. Adv. Mater., 9, 2547 (2007)

STUDIA UNIVERSITATIS BABEŞ-BOLYAI, PHYSICA, LIII, 2, 2008

PHOSPHATE BUFFERED SALINE-INDUCED CHANGES IN RED BLOOD CELLS MEMBRANE FLUCTUATIONS

LUIZA BUIMAGA-IARINCA[1], VASILE V. MORARIU[1]

ABSTRACT. Phosphate Buffered Saline (PBS) is a buffer solution commonly used in biological research because as it is supposed to be a normal environment for the cells. We proved that red blood cells (RBC) fluctuations cease to be normal fluctuations when RBCs are suspended in PBS. The investigation was performed by Detrended Fluctuation Analysis (DFA).

Keywords: Fluctuations, Cell membranes, Artificial suspension medium

Introduction

Membrane fluctuations are common for many cells. The best known example is the, so called, flickering of human red blood cells. The simplest way to investigate it is by recording RBC fluctuations. These cells are quite suitable for investigation of the fluctuations as they are not nucleated cells and have reasonable large diameters, 6–8 μm. Their fluctuation is a low frequency (0.3-30 Hz) phenomenon being easily recorded with an optical microscope.

Cells preserve all their physiological characteristics as long as they are kept in their natural medium. However in biological experiments it is common to use Phosphate Buffered Saline (PBS) as an artificial suspension medium. This is considered to be a reasonable substitute for sanguine plasma [1]. It consists of a solution containing sodium chloride, sodium phosphate, and some times in addition, potassium chloride and potassium phosphate.

We have shown that although the PBS is commonly used in experiments, the cells properties do not remain unchanged. The fluctuation parameters for cellular membrane are drastically modified when the RBC is suspended in PBS compared to sanguine plasma. The method we have used in order to evidence the cell membrane fluctuation changes is Detrended Fluctuation Analysis.

[1] *National Institute for Research and Development of Isotopic and Molecular Technologies, P.O. Box 700, Donath Str. 71-103, 400293 Cluj-Napoca 5, Romania; Tel. +4-0264-584037, Fax: +4-0264-420042*

Detrended Fluctuation Analysis

The method of detrended fluctuation analysis has proven useful in revealing the extent of long-range correlations in time series [2]. Briefly, the time series to be analyzed (with N data) is first integrated. Next, the integrated time series is divided into boxes of equal length, n. In each box of length n, a least squares line is fit to the data (representing the *trend* in that box). The y coordinate of the straight line segments is denoted by $y_n(k)$. Next, we detrend the integrated time series, $y(k)$, by subtracting the local trend, $y_n(k)$, in each box. The root-mean-square fluctuation of this integrated and detrended time series is calculated by

$$F(n) = \sqrt{\frac{1}{N}\sum_{k=1}^{N}[y(k) - y_n(k)]^2} \qquad (2)$$

This computation is repeated over all time scales (box sizes) to characterize the relationship between $F(n)$, the average fluctuation, and the box size, n. Typically, $F(n)$ will increase with box size. A linear relationship on a log-log plot indicates the presence of power law (fractal) scaling. Under such conditions, the fluctuations can be characterized by a scaling exponent, the slope of the line relating log $F(n)$ to log n.

The slope of the graph has been termed α, the scaling exponent, which vary from 0.5 (white noise or uncorrelated random data) to 1.5 (Brownian noise). The behavior is regarded as an $1/f$ noise when $\alpha = 1$ and it extends over at least orderes of magnitude. The behavior is no longer determined by a power law as α increase above 1 to 1.5. In our case the log-log plot is not linear and, instead, the relationship between $logF(n)$ and $log(n)$ appears to have two distinct linear segments, the slopes of both lines are calculated separately and termed α_1 and α_2, respectively. The value of α_1 proved to be superior to α_2 in terms of prognostic ability [3].

Experimental

1 litre of Phosphate-buffered saline (PBS buffer) was prepared from 8 g of NaCl, 0.2 g of KCl, 1.44 g of Na_2HPO_4 and 0.24 g of KH_2PO_4 dissolved in 800 ml of distilled H_2O. We adjusted the pH to 7.4 with HCl and added H_2O to 1 liter.

The fluctuations of the erythrocyte membrane were analyzed on diluted cell suspension, obtained from human blood collected on anticoagulant (sodium citrate 3.8%). The blood was centrifuged 10 minutes at 3000 rot/min. The plasma was isolated and ultra-centrifuged 5 minutes at 7000 rot/min in order to remove the remaining blood platelets.

In the experiment in which we have used integral blood, the erythrocytes were re-suspended in plasma. For the experiment where phosphate buffered serum (PBS pH 7.4) was used, the RBCs were washed three times with PBS and re-suspended in PBS.

In order to avoid erythrocyte aggregation and to analyze single cells we used cells suspensions at high dilution.

Experiments were performed on 20 μl sample volumes, using Rosenthal counting cell with 0.2 mm optical depth. The images set (1000 images) were captured sequentially at 0.2 sec interval using a CCD camera (PixelLINK A-741. CMOS sensor) mounted on an optical microscope equipped with a 40x objective.

The sequential images were processed using ImageJ [3], a free soft offered by the National Institutes of Health, Bethesda, Maryland, USA. Images were processed as in Fig.1.

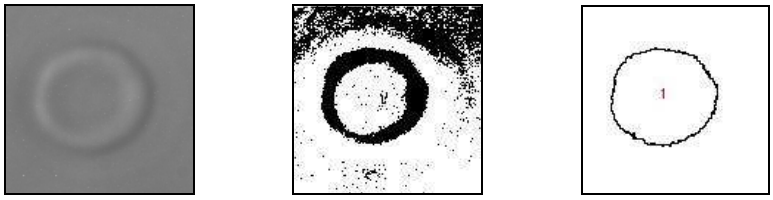

(a) *(b)* *(c)*

Fig. 1. The red cell image (a) and threshold (b) and the simple form of the cell (c)

From the image represented in Fig. 1c, the *Shape Descriptor* plugins (ImageJ) extracts the value of the diameter.

Results

For each experiment we have used 30 red blood cells. The correlation analysis reveals that both RBCs suspended in plasma and PBS presents two short range correlation exponents (Fig. 2). Every correlation segment is shorter than one order of magnitude and the correlation is weaker between closer terms than between distant terms.

The correlation is quite strong for erythrocytes suspended in plasma. Between closer terms, the Gaussian distribution has the median value at $\alpha_1 = 0.98 \pm 0.02$ and the Gaussian width is 0.28 ± 0.05 (Fig. 3). The median value is $\alpha_2 = 1.14 \pm 0.01$ while the Gaussian has the same width for the second correlation segment (Fig. 4). This value denotes that correlation still exists. In the PBS-suspended cells case, the median for the Gaussian function is 0.79+0.01 for the first correlation segment and 0.93+0.01 for the second correlation segment. The Gaussian width is smaller than for cells suspended in plasma, being 0.11 ± 0.02 for the first segment and 0.15 ± 0.02 for the second correlation segment. These results suggest that there are two short

range correlations both for plasma and PBS, but the correlations are stronger for plasma. The first correlation segment defines correlation between first and second terms, the second and the third, and so on. The second correlation segment report on the correlation between the first terms in series and the first term in the second segment (for RBCs series in this experiment we refer about the 500^{th} terms).

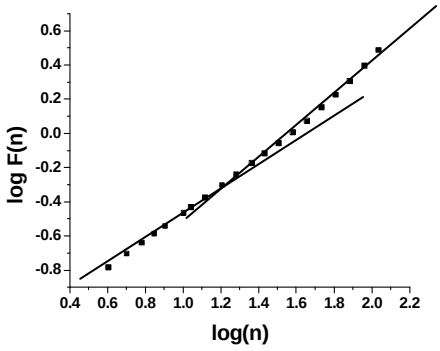

Fig. 2. The DFA plot of RBC diameter when suspended in plasma

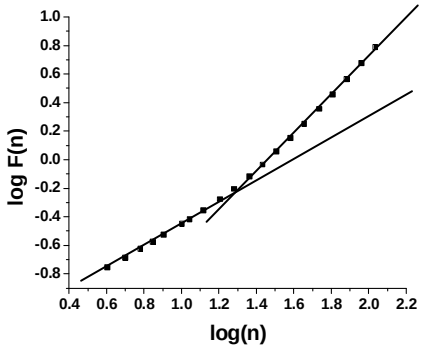

Fig. 3. The DFA plot of RBC diameter when suspended in PBS

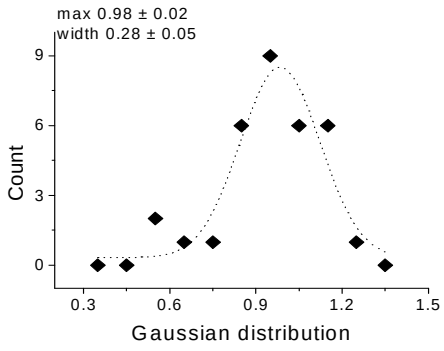

Fig. 4. The Gaussian distribution for the first correlation segment for RBCs suspended in plasma

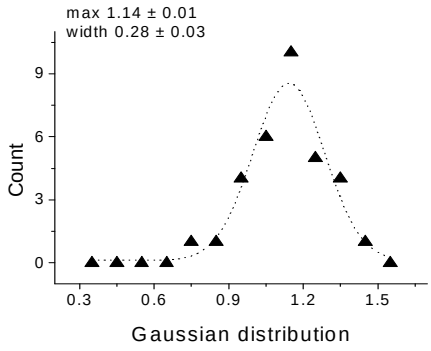

Fig. 5. The Gaussian distribution for the second correlation segment for RBCs suspended in plasma

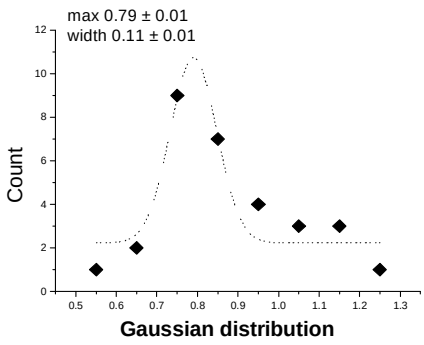

Fig. 6. The Gaussian distribution for the first correlation segment for RBCs suspended in PBS

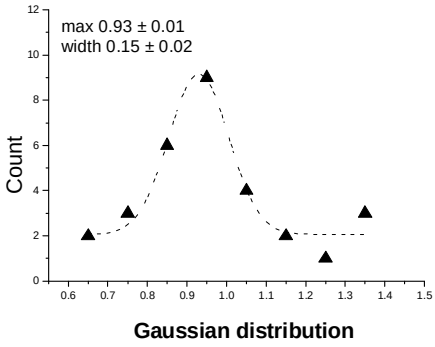

Fig. 7. The Gaussian distribution for the second correlation segment for RBCs suspended in PBS

Conclusions

For RBCs suspended in plasma, the correlation between closer terms seems to be has a value near 1, being stronger then for RBCs suspended in PBS. The correlation between distant terms remains still strong between distant terms for RBCs suspended in PBS. These differnces of fluctuations suggests that the cellular membrane for cells suspended in PBS has changed. Consequently the Phosphate Buffered Saline solution should be regarded as an abnormal suspending medium for red blood cells, at least from the point of view of the flickering phenomenon.

REFERENCES

1. Sambrook, Fritsch, and Maniatis (1989) *Molecular Cloning: A Laboratory Manual*, 2nd ed., Cold Spring Harbor Laboratory Press, Cold Spring Harbor, New York, volume 3, apendix B.12.
2. Peng C-K, Havlin S, Stanley HE, Goldberger AL. *Quantification of scaling exponents and crossover phenomena in nonstationary heartbeat time series.* Chaos 1995; 5:82-87.
3. Andrew JE Seely, Peter T Macklem, *Complex systems and the technology of variability analysis*, Critical Care 2004, 8:R367-R384.
4. Rasband, W.S., ImageJ, U. S. National Institutes of Health, Bethesda, Maryland, USA, http://rsb.info.nih.gov/ij/, 1997-2008.

STUDIA UNIVERSITATIS BABEŞ-BOLYAI, PHYSICA, LIII, 2, 2008

SPECTROSCOPIC INVESTIGATION OF SOME UO_2^{2+}–POLYOXOMETALATE COMPLEXES

N. L. MOGONEA, I. HAUER, D. COZMA, I. B. COZAR, A. MARCU, L. DAVID*

ABSTRACT. The $Na_{10}[(UO_2)_2(H_2O)_2X_2W_{20}O_{70}]\cdot nH_2O$ heteropolyoxometalates (**1**: X =Sb^{III}, n = 28; **2**: X =Bi^{III}, n = 34) were synthesized and investigated by thermal analysis, FT-IR and UV-Vis spectroscopy in order to determine the coordination, the ordering of cation electronic levels and his local symmetry. By comparing FT-IR spectra of the uranyl complexes with the corresponding ligand ($\mathbf{L_1}$= $Na_{12}[Sb_2W_{22}O_{74}(OH)_2]$ and $\mathbf{L_2}$= $Na_{12}[Bi_2W_{22}O_{74}(OH)_2]$) the coordination UO_2^{2+} ions to the POM lacunars unities have been estimated. The UV electronic spectra of the UO_2^{2+}-POM complexes are similar to the ones of the ligands $\mathbf{L_1}$ and $\mathbf{L_2}$. Each spectrum presents two bands assigned to the charge transfer from the ligand to the metal $p_\pi \rightarrow d_\pi$ transitions in W=O bonds and d_π–p_π–d_π electronic transitions between the W-O_b-W bonds energy levels.

The spectroscopic investigations of $Na_{10}[(UO_2)_2(H_2O)_2X_2W_{20}O_{70}]$, X = Sb^{III} (1), Bi^{III} (2) complexes indicate a sandwich-type structure formed by two B-β-XW_9O_{33} fragments binding by two uranyl ions and two WO_2 units.

Keywords: Thermal analysis, FT-IR and UV-vis spectroscopy, Chemical complexes

Introduction

The structure of polyoxometalic species can be described as a 1:2 sandwich type of structure: $Ln^{3+/4+}$ or An^{4+} ions with monovacant lacunars polyoxoanions "ligands", such as $[Ln^{III}(PW_{11}O_{39})_2]^{11-}$, where the metallic cations occupy an antiprismatic coordinative position. Sometimes, even though U^{IV} can be stabilized in these kinds of complexes, the chemistry of the watery solutions of the first actinides is dominated by trans-dioxo cations, from which the most familiar is UO_2^{2+}. Pope [2] reports the first example of heteropolyoxowolframats which incorporates the $U^{IV}O_2$, linear steric, as expected.

The $\{XW_{11}\}$ (with X=Sb^{III}, Bi^{III}) type of monolacunary polyoxocations and their complexes with a division of 1:1 with the di- and trivalent cations of transitional metals were published since 1970 [6,8]; recently these species were revealed as dimmers on the basis of the structure determined on the Krebs salts $[Sb_2W_{22}O_{74}(OH)_2]^{12-}$, $[Sb_2W_{20}Fe^{III}{}_2O_{70}(H_2O)_6]^{8-}$, $[Sb_2W_{20}Co^{II}{}_2O_{70}(H_2O)_6]^{10-}$ and $[Bi_2W_{20}Fe^{III}{}_2O_{70}(H_2O)_6]^{6}$.

* *Faculty of Physics, "Babes-Bolyai" University, 400084 Cluj-Napoca, Romania*

The polyoxotungstate anion structure consists of two groups {B-β-XW_9}, bonded by two additional tungsten centres weaker bonded which can be replaced with $M^{II/III}$ cations in the substituted polyoxoanions.

The Krebs $[X_2W_{22}O_{74}(OH))_2]^{12-}$ type of polyoxoanions belong to the clusters that incorporate different lacunary trivacant polyoxometalic fragments with the formula $[XW_9O_{33}]^{9-}$ where X= As^{III}, Sb^{III}, Bi^{III}.

The polyoxometalate $Na_{10}[(UO_2)_2(H_2O)_2X_2W_{20}O_{70}]$, X = Sb^{III} (1), Bi^{III} (2) was prepared and investigated by thermal analysis, FT–IR and UV–Vis spectroscopy.

Experimental

Reagent grade chemicals were used and all syntheses and studies were carried out in distilled water. The sodium salt of the polyoxometalate ligand $Na_2[Sb_2W_{22}O_{74}(OH)_2]\cdot 42H_2O$ (L_1) was prepared as previously reported [9] and the sodium salt of the polyoxometalate ligand $Na_2[Bi_2W_{22}O_{74}(OH)_2]\cdot 42H_2O$ (L_2) was prepared as previously reported [10].

Synthesis of $Na_2[Sb_2W_{22}O_{74}(OH)_2]\cdot 42H_2O$ (L_1) ligand

The **L_1** ligand was obtained according to the direct polycondensation method of sodium tungstate around the Sb(III) heteroatom after an original recipe which consists in the heat dissolvation of 33 g (100 mmol) of $Na_2WO_4\cdot 2H_2O$ in 100 ml of water, to which was added 40 ml solution acetic buffer with pH= 4.7 and it was boiled, after that some drops were added under stirring of a solution obtained from 0.9 g (4.5 mmls) of Sb_2O_3 dissolved in 13 ml of concentrated HNO_3. Diluted at 50 ml with distilled water, the clear yellow solution was refluxed at 80-90°C for two hours, then it was concentrated on a hot water bath until the halving of the initial volume, then the solution was allowed to slowly crystallize at room temperature. After three days, 24.5 g of small acicular pearl white crystals were obtained (with a yield of 86%) in 30 ml distilled water (pH = 4.5 obtained by adjustment with HCl 1M) it was strongly stirred at 70°C for 30 minutes. The clear yellow-orange solution was kept for 20 minutes on a water bath, than was hold at room temperature for 48 hours, while the compound begins to crystallize. The translucent/transparent crystals were recrystallized three times from distilled water at a pH of 4.5. 3.59g (58%) of compound was obtained.

Synthesis of $Na_{10}[(UO_2)_2(H_2O)_4Sb_2W_{20}O_{70}]\cdot 28H_2O$ (1) complex

A solution formed by 0.47 g (2 mmol) of $UO_2(NO_3)_2\cdot 4H_2O$ in 15 ml of distilled water was added to a solution formed by the dissolvation of 6.27g (1 mmol) of $Na_2[Sb_2W_{22}O_{74}(OH)_2]\cdot 42H_2O$ in 30 ml of distilled water (pH = 4.5 obtained by adjustment with HCl 1M) was strongly stirred at 70°C for 30 minutes. The clear yellow-orange solution was kept for 20 minutes on a water bath, after it was hold at room temperature for 48 hours, while the compound begins to crystallize. The translucent/transparent crystals were recrystallized three times from distilled water at a pH of 4.5. 4.15g (65%) of compound was obtained.

Synthesis of $Na_{10}[(UO_2)_2(H_2O)_4Bi_2W_{20}O_{70}]\cdot 34H_2O$ (2) complex

A solution formed by 0.47g (2 mmol) of $UO_2(NO_3)_2\cdot 4H_2O$ in 15 ml of distilled water was added to a solution formed by the dissolution of 6.75 g (1 mmol) of $Na_2[Bi_2W_{22}O_{74}(OH)_2]\cdot 42H_2O$ (**L_2**) in 30 ml of distilled water (pH=4.5 obtained by adjustment with HCl 1M) was strongly stirred at 70°C for 30 minutes. The clear yellow-orange solution is kept for 20 minutes on a water bath, after which it is hold at room temperature for 48 hours, when the compound begins to crystallize. The translucent crystals were recrystallized three times from distilled water with a pH of 4.5. 4.73g (71%) were obtained.

Physical measurements

The establishment of the optimum synthesis conditions was made by the molar ratios applied to spectrophotometry (λ=500 nm). The thermal analysis was performed using a METTLER-TGA/SDTA 851^e device, using a SOFT:STAR^e Software program. The working parameters are: the working massage, m_{sample}=15.1280 mg for $[Na_{10}[(UO_2)_2(H_2O)_4Sb_2W_{20}O_{70}]$ compound and m_{sample}=14.8256 mg for $[Na_{10}[(UO_2)_2(H_2O)_4Bi_2W_{20}O_{70}]$ compound (temperature range, T = 20-800 °C, heating speed, dT/dt=10 °C/min, balance sensibility, S=1 μg).

The FT-IR spectra were recorded with an Equinox 55 Bruker spectrophotometer on KBr pellets, in the 4000–400 cm^{-1} range. Electronic spectra were performed in aqueous solutions within a range of λ =200-800 nm using a JASCO 530 spectrophotometer.

Results and discussion

1. Elemental analysis

The reaction stereochemistry, once established, by stereophotometric titration, the $[(UO_2)_2(H_2O)_2X_2W_{20}O_{74}]^{12-}$ complexes synthesis was performed. Due to the fact that the $[X_2W_{22}O_{74}(OH)_2]^{12-}$ species where X= Sb^{III}, Bi^{III} were not stable in aqueous solutions, the reaction was lead by adding solid sodium salts of the ligand to the $UO_2(NO_3)_2$ aqueous solution. The complex polyoxoanions obtained was stable only in the presence of an excess of sodium ions and the obtained complexes were crystallized, with a good yield, after a few days from a solution kept at 5 °C. The results of the elementary chemical analysis are agreeably with the recommended formulary (Table 1).

Table 1.

The chemical analysis data of the synthesized compounds.

Complex	Yield (g / %)	Colour	Found (calc.) (%)				
			Na	X	W	U	H_2O
1	4.3 / 74	Yellow-Orange	3,72 (3,60)	3,86 (3,81)	57,70 (57,57)	7,48 (7,45)	8,98 (9,02)
2	3.4 / 57	Yellow-Orange	3,57 (3,45)	6,28 (6,27)	55,60 (55,15)	7,18 (7,14)	10,22 (10,26)

2. Thermogravimetric analysis

The thermogravimetric analysis show that between 35-325 ^{0}C the mass lost was 1.3491 mg (8.9185 %) and 1.5039 mg (10.1443 %) for **1** and respectively **2** complexes.

The water loss process took place in two successive phases: the first between 35-120 ^{0}C which corresponds to 28 (**1**) respectively 34 (**2**) water molecules lost (crystallization water), and the second between 120-325 ^{0}C which corresponds to 4 water molecules lost (coordinating water) for both complexes.

The DTA curves indicate two endothermic and two exothermic effects. The endothermic effects with a maximum temperature at ≈ 120 ^{0}C and ≈ 325 ^{0}C correspond to the water loss processes. The exothermic effect with a maximum at ≈ 430 ^{0}C corresponds to the crystallization process of the oxides from the mixture, and the exothermic effect with a maximum temperature at ≈ 500 ^{0}C corresponds to the phase transformation from oxides structures in the mixture [11].

3. FT – IR spectra

By comparing the FT-IR spectra of the uranyl complexes (**1**) and (**2**) with that of the corresponding ligand ($\mathbf{L_1}$=$Na_{12}[Sb_2W_{22}O_{74}(OH)_2]\cdot 42H_2O$ and $\mathbf{L_2}$= $Na_{12}[Bi_2W_{22}O_{74}(OH)_2]\cdot 42H_2O$) and their shifts, we obtained information regarding the UO_2^{2+} ions coordination to the lacunars POM unities, the local symmetry and the bonds strength (Fig. 1).

The bands shifting ν_{as}(As–$O_{b,c}$–W), ν_s(W–O_b–W), ν_{as}(W–O_c–W) in complex **1** comparing to the $\mathbf{L_1}$ ligand is due to the substitution of the side WO_6 octahedra by $UO_2^{2+}O_6$ octahedra and the UO_2^{2+} ions coordination to the $O_{b,c}$ type of oxygen. The FT-IR bands are larger in the complex, some of them being superposed. The ν_{as}(W=O_d) vibration band is shifted in the complex to higher frequencies than the ligand due to the substitution of the two ions of wolfram with two ions of uranyl (Fig.1).

For the second complex, the most shifted bands are ν_{as}(Sb–$O_{b,c}$–W) and ν_{as}(W–$O_{b,c}$–W). The ν_{as}(W=O_d) band is unchanged according to the structural establishment of β-B-SbW_9O_{33}. The ν_{as}(Sb–O_a) band is splitted being shifted in the complex spectrum only the low frequency component. This suggests a small influence of the UO_2^{2+} ions coordination to the Sb–O bonds and the presence of the s^2 electron pair steric-inerta to each Sb^{III} atom [10]. The most shifted bands are ν_{as}(W–O_c–W) that involve the oxygen atoms of tricentric W–O_c–W bond of the edge sharing WO_6 octahedra in the complexes spectra comparing to the ligands. The ν_{as}(W–O_e–W) band is splitted, in the both complexes being shifted in the complexes spectra toward higher or lower frequencies. This is consistent with an increase or decrease of the anions cohesion when coordination of the uranyl ions in the polyoxometalates frameworks takes place.

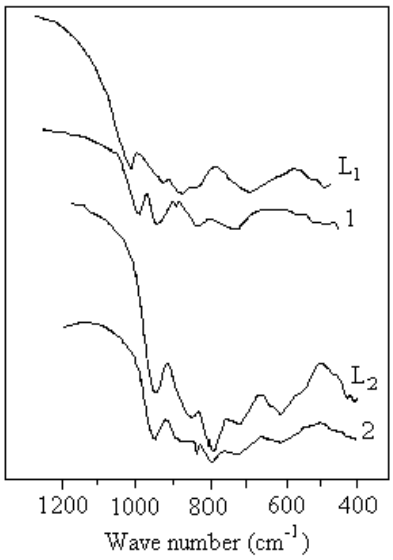

Fig. 1. FT - IR spectra of the ligands and of the UO_2^{2+} - POM complexes (1, 2)

The $\nu_{as}(UO_2^{2+})$ bands are shifted in polyoxometallic complexes to lower frequencies at ~835 cm^{-1}, comparing to the corresponding band from the $UO_2(NO_3)_2 \cdot 4H_2O$ (965 cm^{-1}) [11] and in complex polyoxometalates with uranyl, the IR spectra are compared similar to the ones of acetate complexes like $UO_2(CH_3COO)_2[(C_6H_5)_3AsO]_2$ [12] regarding the asymmetric stretching vibration frequency of the uranyl UO_2 unit. The presence of the different heteroatom in ligands polyoxometalates doesn't seem to affect the absorption frequency of uranyl because the band assigned to this vibrational mode is observed in the same position (~835 cm^{-1}) in complexes **1**, **2**.

Generally, in polyoxometalate complexes, the UO_2^{2+} group is linear and normal to the equatorial plane formed by the oxygen atoms from the complex. Therefore, the polyoxometalate ligands form strong bonds with uranium by lowering the order of the U=O band and consistently lowering the $\nu_{as}(O=U=O)$ frequency.

4. UV – VIS spectra

The UV electronic spectra of the UO_2^{2+}-POM complexes are similar to the ones of the $\mathbf{L_1}$ and $\mathbf{L_2}$ ligand (Fig. 2). Each spectrum presents two bands assigned to the charge transfer from the ligand to the metal $p_\pi \rightarrow d_\pi$ transitions in W=O bonds and d_π–p_π–d_π electronic transitions between the W-O-W bonds energy levels [13-14].

The shifting of the bands maximums for the complex, comparing to the to the ones of the ligand are due to the distortion introduced by the UO_2^{2+} ions coordinated to the neighbour WO_6 octahedra. The bicentric W=O band is more shifted for

complexes **2** comparing to the $\mathbf{L_2}$ ligand (~ 440 cm^{-1}) and for complex **1** comparing to the $\mathbf{L_1}$ ligand (~ 254 cm^{-1}). This band is only shifted by ~ 350 cm^{-1} for complex **1** comparing to the $\mathbf{L_1}$ ligand. The charge transfer band from the tricentric bond $d_\pi \rightarrow p_\pi \rightarrow d_\pi$ presents a shoulder for the UO_2^{2+}-POM complexes but not for the ligands because of the inequivalent character of the W-O-W bonds after the UO_2^{2+} complexion.

The W=O bond is more shifted for complexes than for ligands. The charge transfer band from the d_π–p_π–d_π bond presents a shoulder for the UO_2^{2+}-POM complexes, but not for the ligands because of the inequivalent feature of the W-O-W bonds after the UO_2^{2+} complexion.

The VIS electronic absorption spectra of the complexes in water solutions are very similar and present the bands due to O=U=O internal transitions (at ≈ 420 and ≈ 430 nm), charge transfer transitions (at ≈ 468 and ≈ 481 nm) and U (f→f) electronic transitions at ≈ 500 nm (Fig. 3) [2].

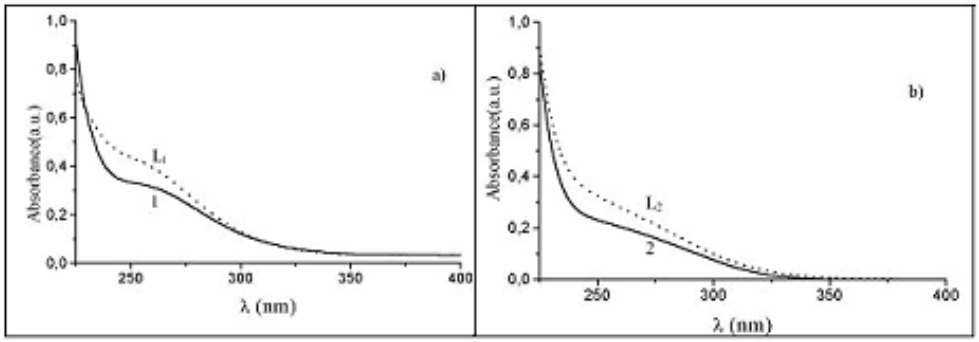

Fig. 2. The UV spectra of the ligands and UO_2^{2+} complexes

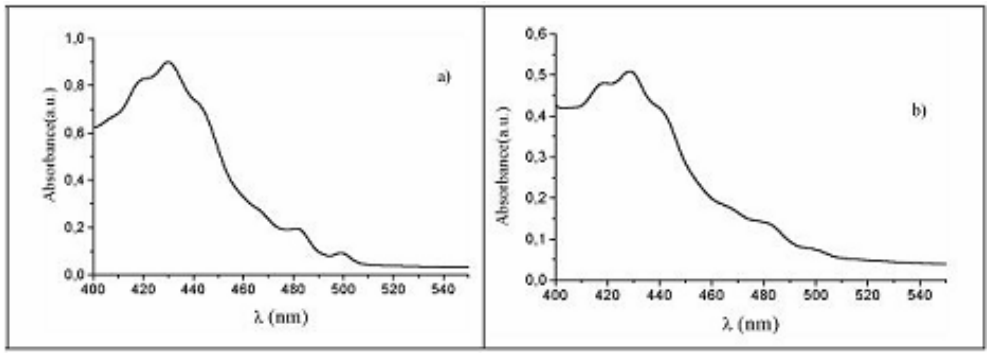

Fig. 3. The VIS electronic spectra of UO_2^{2+} complexes in aqueous solution (1 (a), 2 (b))

Conclusions

According to our studies, we propose for the uranyl complexes polyoxometalates a "sandwich" kind of structure, which consist of two B–β–XW_9O_{33} fragments united by two uranyl ions and two WO_2 fragments (Fig. 4). Each uranium atom adopts the bipyramidal pentagonal coordination, forming two equatorial bonds to the terminal oxygen of a pair of two WO_6 octahedra bonded by common edges which belong to one of the B–β–XW_9O_{33} fragments and a bond to the terminal oxygen of one of the WO_6 fragment, the other two equatorial coordinating points being satisfied by two molecules of water.

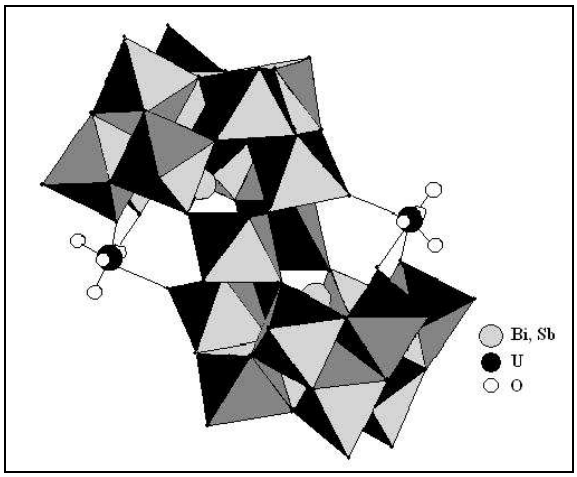

Fig. 4. The proposed structure of $Na_{10}[(UO_2)_2(H_2O)_2X_2W_{20}O_{70}]$, X = Sb^{III}, Bi^{III} complexes

The spectroscopic investigations of $Na_{10}[(UO_2)_2(H_2O)_2X_2W_{20}O_{70}]$, X = Sb^{III} (1), Bi^{III} (2) complexes indicate a sandwich-type structure formed by two B-β-XW_9O_{33} fragments binding by two uranyl ions and two WO_2 units.

REFERENCES

1. R. D. Peacock, T. J. R. Weakley, J. Chem. Soc. A (1971) 1836.
2. K.C. Kim, M. T. Pope; J. Am. Chem. Soc., 121 (1999) 8512.
3. K.C. Kim, M. T. Pope, J. Chem. Soc. Dalton Trans., (2001) 986.

4. C. Rosu, M. Rusu, C. Ciocan, Rev. Chim.(Bucuresti), 53 (2002) 157.
5. K.C. Kim, A.J. Gaunt, M T. Pope; Journal of Cluster Science, 13 (2002) 423.
6. A.J. Gaunt, I. May, R. Copping, I. Bhatt, D. Collison; O.D. Fox, K.T. Holman, M.T. Pope, J. Chem. Soc. Dalton Trans., (2003) 3009.
7. P. Souchay, M. Leray, G. Hervè, R. Acad. Sci., Ser. C 271 (1970) 1337.
8. M. Michelon, P. Souchay, R. Massart, G. Hervè, C. R. Acad. Sci., Ser. C 273 (1971) 1117.
9. Michelon, M.; Hervè, G.; C. R. Acad. Sci., Ser. C, 273 (1972) 209.
10. M. Bösing, I. Loose, H. Pohlmann, B. Krebs, Chem. Eur. J., 3 (1997) 1232.
11. I. Loose, E. Droste, M. Bosing, H. Pohlmann, M.H. Dickman, C. Rosu, M. Pope,B. Krebs; Inorg. Chem., 38 (1999) 2688.
12. M. Pospisil, J. Thermal Analysis, 44 (1995) 133.
13. W. M. Hosny, Synth. React. Inorg. Met.-Org. Chem., 28 (1998) 1029.
14. O.M. Varga, M.T. Pope, Inorg. Chem., 9 (1970) 667.
15. H. So, M.T. Pope, Inorg. Chem., 11 (1972) 1441.

STUDIA UNIVERSITATIS BABEŞ-BOLYAI, PHYSICA, LIII, 2, 2008

STRUCTURAL STUDIES ON MESOPOROUS ALUMINA

M. MAIER[1], V. PARVULESCU[2], M. TAMASAN[3], M. VASILESCU[1], R.F.V. TURCU[1], H. MOCUTA[3], S. SIMON[1,3]

ABSTRACT. Mesoporous alumina offer the possibility of improving the catalytic efficiency of many heterogeneous catalytic processes, such as automobile exhaust control, petroleum refining and petrochemical processing. KF/Al_2O_3 catalysts with different loadings from 1 till 20 wt.% were prepared using aqueous solutions of the alkaline fluoride compounds by wetness impregnation of basic mesoporous alumina. KF supported on mesoporous alumina was characterized by Differential Thermal Analysis (DTA), Magic-Angle-Spinning Nuclear Magnetic Resonance spectroscopy (^{27}Al MAS NMR) and by X-Ray Diffraction (XRD) measurements. XRD revealed two different phases for the samples with different KF contents, identified as AlO(OH) and K_3AlF_6. MAS NMR spectra show that three types of Al species are present: hexa- and tetra-coordinated with oxygens and a hexa-coordinated one with flour.

Keywords: mesoporous alumina, catalysts, XRD, NMR, Thermal analysis

Introduction

Aluminas are important industrial chemicals that have found wide application as adsorbents, ceramics, abrasives, catalysts and catalyst supports [1]. Alumina is widely used in catalysis as part of bifunctional catalysts, largely because it is inexpensive, reasonably stable, and can provide high surface area for many catalytic applications. As a general rule, the alumina used in catalytic reactions always requires a controlled pore size distribution. Because of this reason, the demand for mesoporous materials (pore radius higher than 1.0 nm and lower than 25 nm) has triggered major synthetic efforts in academic and industrial laboratories [2]. Mesoporous materials represent a class of molecular sieves having a high potential for commercial applications in adsorption and catalysis. Their regular pore arrangement is responsible for their extraordinary properties, such as high surface area and narrow pore size distributions [3]. Despite enormous importance mesoporous alumina, which exhibits narrow pore size distribution, higher surface areas and abundant of surface hydroxyl groups compared to conventional aluminas, for catalyst supports or adsorbents, the number of papers dealing with the characterization of mesoporous

[1] *Babes-Bolyai University, Faculty of Physics, 400084 Cluj-Napoca, Romania*
[2] *University of Bucharest, Department of Chemical Technology and Catalysis, 4 – 12 Regina Elisabeta Bvd., Bucharest 030016, Romania*
[3] *Institute for Interdisciplinary Experimental Research of Babes-Bolyai University, 400271 Cluj-Napoca, Romania*

alumina is still limited [4]. Mesoporous alumina represents a very interesting molecular sieve exhibiting a narrow pore size distribution with higher surface areas compared to conventional alumina, used as a support for catalytically active species a large scale of industrial processes such as petrochemical processing, petroleum refining, the steam reforming of hydrocarbon feedstock to produce hydrogen and automobile exhaust control.

The aim of this research is to characterize potassium fluoride supported on alumina (KF/Al_2O_3), a typical base catalyst [5, 6], at different KF concentrations. The effect of potassium fluoride addition over the mesoporous alumina is explored and discussed in terms of structure change.

The catalysts were investigated using X-Ray Diffraction, ^{27}Al Magic-Angle-Spinning Nuclear Magnetic Resonance and Differential Thermal Analysis.

Experimental

KF/Al_2O_3 catalysts with different loadings from 10 till 20 wt% were prepared using aqueous solutions of the alkaline fluoride compounds. KF was supported onto Al_2O_3 using wetness impregnation of basic mesoporous alumina synthesized according to literature data [7, 8]. There were obtained four samples with different potassium fluoride concentrations, varying from 0 to 20 wt. % KF.

For this purpose, in 1.65 mL, which represents the impregnation capacity of the 1.5 g support, 0.166 g (for 10 wt. % KF/Al_2O_3), 0.26 g (for 15 wt. % KF/Al_2O_3), 0.375 g (for 20 wt. % KF/Al_2O_3), respectively, were dissolved. After that the materials were dried over night at room temperature and then, for 12 h, at 393 K.

Thermogravimetric and differential thermal analysis measurements were carried out using a Shimadzu DTG-60H analyzer, with a rate of 10^0C/min, up to 1400^0C in static air atmosphere, at a flow rate of 70 ml/min, using alumina crucibles.

The activation of the catalysts has been checked by XRD measurements performed on a Shimadzu X-ray diffractometer XRD-6000 using Ni-filtered Cu-Kα radiation (λ = 1.5418 Å). The operation voltage and current were 40 kV and 30 mA. The measurements were performed at a scan speed of 1˚/min in a scan range from 5˚to 80˚, 2θ.

^{27}Al MAS NMR spectra were recorded at 15 kHz on a Bruker AVANCE 400 MHz NMR Spectrometer, operating at 9.4 Tesla.

Results and Discussion

1. Thermal analysis

TGA-DTA experiments were used to examine the thermal evolution and the weight loss in order to understand the structural changes that take place in the studied samples. The TGA–DTA trace of aluminium oxide (alumina) is reported in Fig. 1 and shows one weight loss in the range 200 – 400 ^{0}C corresponding to a broad exothermic peak. This weight loss above 255 ^{0}C is composed of hydroxyl group OH^- and also at this temperature begins the structural transformation of aluminum

oxyhydroxides AlO(OH) into γ-Al_2O_3 [9]. At higher temperatures in the range 800 – 950 ^{0}C the transition from γ-Al_2O_3 to the crystalline form of corundum α-Al_2O_3 take place.

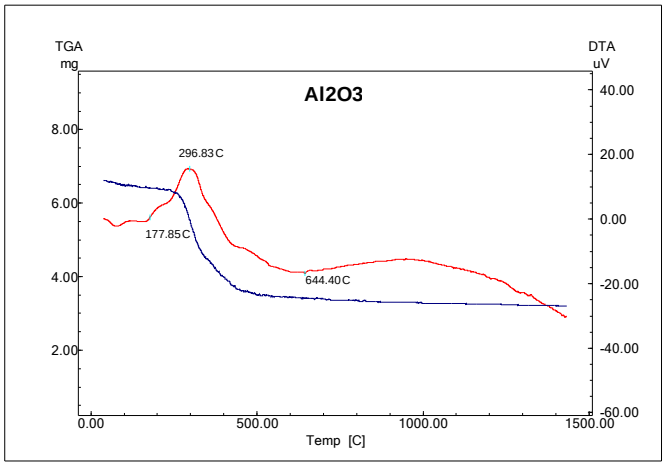

Fig. 1. TGA–DTA trace of alumina sample.

The TGA–DTA traces of KF-alumina are reported in Fig. 2 and Fig. 3. Beside the weight loss of hydroxyl group OH^- between 200 and 500 ^{0}C, there is another weight loss at about 950 ^{0}C, with a concomitant structural change, due to the transition from γ-alumina to α-alumina, the weight loss being assigned to the vaporization of the K_3AlF_6 phase, confirmed by XRD analysis.

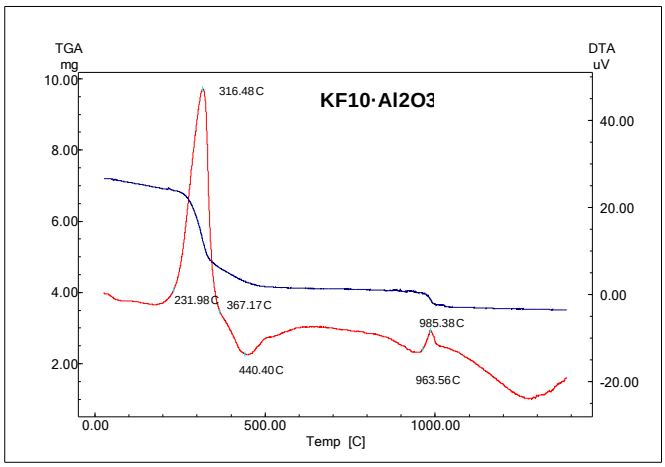

Fig. 2. TGA–DTA trace of xKF (100-x)Al_2O_3 system, x = 10 wt. %.

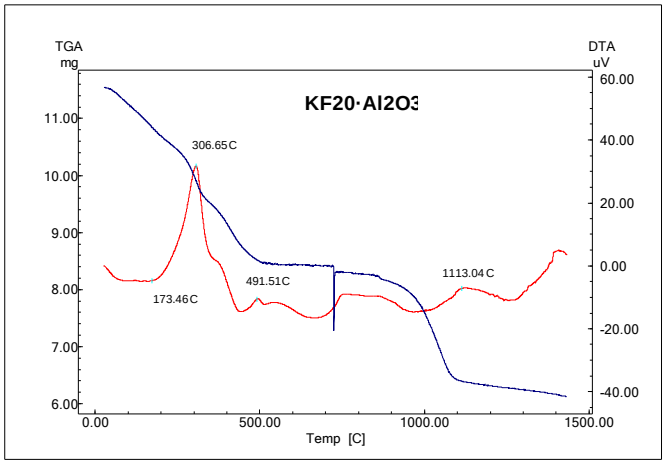

Fig. 3. TGA–DTA trace of xKF (100-x)Al_2O_3 system, x = 20 wt. %.

2. XRD analysis

Through X-Ray diffraction on xKF (100-x)Al_2O_3 system (Fig. 4), two phases could be identified: AlO(OH) phase and K_3AlF_6 phase. Therefore, the XRD pattern of the alumina sample without KF loading, shows only the first phase, while in case of the KF-alumina doped samples, beside AlO(OH) phase the second phase, K_3AlF_6, is present. It can be observed that for alumina sample the lines belonging to AlO(OH) are quite sharp, while in the KF doped alumina samples these lines become broad and the narrow lines corresponding to K_3AlF_6 phase are evidenced.

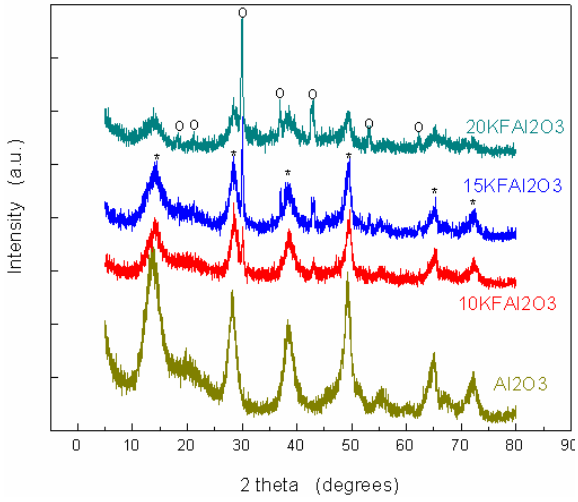

Fig. 4. X-ray patterns recorded on xKF (100-x)Al_2O_3 system, x = 0,10, 15, 20 wt.%, where: ***** - AlO(OH) phase and **o** -K_3AlF_6 phase.

3. ^{27}Al MAS NMR investigation

The nature of Al species was investigated by MAS NMR. The spectra obtained from alumina and KF-alumina samples are presented in Fig. 5a. Also one example of spectrum deconvolution is showed in Fig. 5b. The ^{27}Al MAS NMR spectra present a line at ~ 10 ppm [10-13], assigned to hexa-coordinated Al of the undoped and doped alumina samples. In the doped alumina sample with x = 20 wt.% KF a narrow at ~ 0 ppm can be observed and it is assigned to hexa-coordinated Al with 6 ions of fluoride. Also, in the same doped alumina sample with x = 20 wt.% KF, there is a broad resonance peak occurred at ~ 75 ppm that prove the existence of some tetra-coordinated positions probably due to the AlO(OH) phase network distortions. The spectra deconvolution was made using the DMFIT program [14] and the ^{27}Al MAS NMR spectra parameters of the studied samples are reported in Table 1.

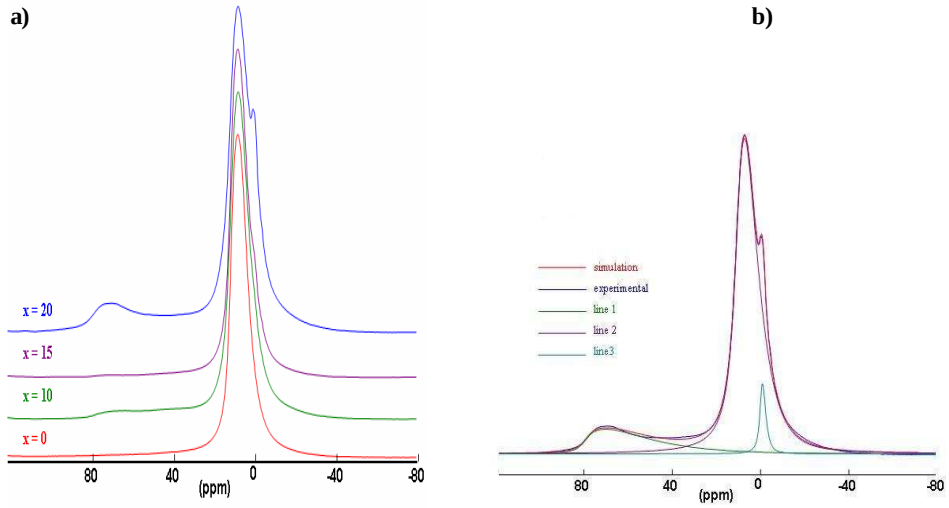

Fig. 5 a) ^{27}Al MAS NMR spectra for the samples of xKF (100-x)Al_2O_3 system; b) ^{27}Al MAS NMR deconvolution spectrum for the sample with x = 20.

Table 1

The ^{27}Al MAS NMR spectra parameters of the studied samples.

x(KF) (100-x)Al2O3

Sample 1 x=0	**Amplitude**	**Position (ppm)**	**Line width (Hz)**	**CQ (kHz)**	**etaQ**	**I (%)**
Line 1	20559.44	75.33	3226.38	527.36	0.99	7.52
Line 2	252961.57	10.19	502.52	2389.22	0.96	92.48

Sample 2 x=10	Amplitude	Position (ppm)	Line width (Hz)	CQ (kHz)	etaQ	I (%)
Line 1	7171.68	75.69	702.08	6279.52	0.99	1.01
Line 2	61079.56	39.08	2019.43	771.93	0.99	8.63
Line 3	635955.81	10.35	611.63	2511.75	0.9	89.78
Line 4	4127.75	-0.31	56.55	825.78	0.9	0.58

Sample 3 x=15	Amplitude	Position (ppm)	Line width (Hz)	CQ (kHz)	etaQ	I (%)
Line 1	4025.29	75.52	531.1	4251.72	0.99	0.19
Line 2	79499.77	42.29	2520.04	990.05	0.99	3.80
Line 3	1944392.5	10.44	493.92	2520.08	0.98	92.81
Line 4	67024.24	-0.26	250.61	1454.01	0.9	3.20

Sample 4 x=20	Amplitude	Position (ppm)	Line width (Hz)	CQ (kHz)	etaQ	I (%)
Line 1	20619.94	80.46	568.95	5956.2	0.9	3.20
Line 2	474408.62	10.78	706.3	2732.39	0.9	73.64
Line 3	149174.87	-0.52	230.74	1182.94	0.9	23.16

Conclusions

The analysis performed with complementary techniques, Differential Thermal Analysis, Magic-Angle-Spinning Nuclear Magnetic Resonance, and X-Ray Diffraction, revealed essential structural data in order to understand the effect of KF addition over the mesoporous alumina structure.

The thermal behaviour and XRD analysis were confirmed by the characterization of the aluminium coordination using the ^{27}Al MAS NMR spectroscopy. Differential Thermal Analysis revealed that the addition of KF led to hydroxyls at the surface of alumina and also, at higher temperatures, to a structural change due to the transition from γ-alumina to α-alumina.

By X-ray diffraction was identified the AlO(OH) phase and also a new phase in the case of doped samples, the K_3AlF_6 phase. This new phase was not detected by X-ray diffraction at low loadings, while at higher loadings it was present.

Comparing to the undoped sample's spectra, the ^{27}Al MAS NMR spectroscopy of doped samples show that for the sample with the higher KF loading, beside the presence of hexa-coordinated Al with six oxygens, there are some tetra-coordinated positions and also hexa-coordinated one with six ions of fluoride.

Therefore, the KF addition led to low coordinated aluminium species and also to a new phase consisting in K_3AlF_6.

Acknowledgments

This work is supported from project: PN2, no. 21-048/2007.

REFERENCES

[1] Ciesla Ulrike, Schüth Ferdi, *Microporous and Mesoporous Materials* 27,131, (1999)

[2] N. Yao, G. Xiong, Y. Zhang, M. He, W. Yang, *Catalysis Today* 68, 97, (2001)

[3] J. Cejka, N. Zilkova, J. Rathosk, A. Zukal, *Langmuir* 20, 7532, (2004)

[4] J. Cejka, *Applied Catalysis A: General* 254, 327, (2003)

[5] J. Yamawaki, T. Ando, *Chem. Lett.* 24, 45, (1979)

[6] J. Clark, H. Cork, D.G. Robertson, *M. S. Chem. Lett.* 13 , 1145, (1983)

[7] Z. Zhang, T.J. Pinnavaia, *J. Am. Chem. Soc.* 124, 12294, (2002)

[8] Z. Zhang, R.W. Hicks, T.R. Pauly, T.J. Pinnavaia, *J. Am. Chem. Soc.* 124, 1592, (2002)

[9] C.J. Brinker, G.W. Scherer, *Sol-Gel Science: The Physics and Chemistry of Sol-Gel Processing*, Academic Press, New York, (1990)

[10] S. Simon**,** A. van der Pol, E.J. Reijerse, APM Kentgens, G.J.M.P. van Morsel, E. de Boer, *J. Chem. Soc. Faraday Trans*. 91, (10), 1519, (1995)

[11] S. Simon, G.J.M.P. van Moorsel, A.P.M. Kentgens, E. de Boer, *Solid State NMR*, 5, (2), 163, (1995)

[12] S. Simon, *Mod. Phys. Lett. B*, 15, 375, (2001)

[13] V. Simon, R.V.F. Turcu, D. Eniu, S. Simon, *Physica B* 403, 139, (2008)

[14] D. Massiot, F. Fayon, M. Kapron, I. King, S. Le Calve, B. Alonso, J.-O. Durand, B. Bujoli, Z. Gan, G. Hoatson, Magn. Reson. Chem. 40, 70, (2002)

STUDIA UNIVERSITATIS BABEŞ-BOLYAI, PHYSICA, LIII, 2, 2008

PROPERTIES OF NOVEL Fe@Au CORE-SHELL NANOPARTICLES

C. LEOSTEAN*, O. PANA*, R. TURCU*, M.L. SORAN*

ABSTRACT. In this work we present the structural and magnetic properties of the core-shell iron-gold (Fe@Au) nanoparticles obtained by inverse micelles method. The properties of the composites were investigated by TEM, HRTEM, X-ray diffraction (XRD), X-ray Photoelectron spectroscopy (XPS) and magnetization measurements.

The experimental results show that the majority of nanoparticles are superparamagnetic with mean diameters of 5 nm.

Keywords: nanoparticles, core-shell, superparamagnetism

1. Introduction

Superparamagnetic core-shell nanoparticles with appropriate surface coating attracted much interest in the last few years owing to their fundamental interest and applications [1-4]. These new materials are increasingly used for various biomedical applications, such as magnetic resonance imaging, hyperthermia, drug delivery, tissue repair, cell and tissue targeting. All these biomedical and bioengineering applications require that these nanoparticles have high magnetization values and size smaller than 100nm with overall narrow particle size distribution, so that the particles have uniform physical and chemical properties. In addition, these applications need special surface coating of the magnetic particles, which has to be not only non-toxic and biocompatible but also allow a targetable delivery with particle localization in a specific area [5].

In this paper we present the structural magnetic properties of the core-shell iron-gold (Fe@Au) nanoparticles. Our goal is to study the effects of the core-shell structuralizing process onto the magnetic properties of these systems in order to obtain the required characteristics for specific applications.

2. Experimental

Samples preparation

Gold-coated iron nanoparticles generally were obtained by reverse micelle method [6]. We used $FeSO_4$ $7H_2O$ and $HAuCl_4$ as precursors and $NaBH_4$ as reducing agent; 4.8 ml $FeSO_4$ 0.5M (aq.), 6 g cetyltrimethylammonium bromide (CTAB),

* *National Institute for R&D of Isotopic and Molecular Technologies, 75-103 Donath, Str., 400293, Cluj-Napoca 5, P.O. Box 700, Cluj-Napoca, Romania*

12.48 ml 1-butanol, 42.8 ml octane were mixed up with 4.8 ml $NaBH_4$ 1M, 6 g CTAB, 12.48 ml 1-butanol and 42.8 ml octane. This mixture was stirred 1 hour, at the room temperature, under inert atmosphere. Another mixture containing: 3.6 ml $NaBH_4$ 1.6 M + 3 g CTAB + 6.2 ml 1-butanol + 28.6 ml octane and 3.6 ml $HAuCl_4$ 0.44 M + 3 g CTAB + 6.2 ml 1-butanol + 2.86 ml octane, was added at the solution, after 1 hour. The new solution was stirred 5 hours, at the room temperature, under inert atmosphere. In this synthesis the CTAB was the surfactant and the 1-butanol was the co-surfactant. After synthesis, the remaining surfactants were removed by thorough washing with a 1:1 chloroform/methanol mixture.

Characterization methods

The morphology of the Fe@Au core-shell nanostructures was determined by TEM and HRTEM using 1010 JEOL and Hitachi H9000NAR transmission electron microscopes.

Structural characterization of the samples was performed by X-ray diffraction (XRD) using Bruker D8 Advance diffractometer.

X-ray photoelectron spectroscopy (XPS) was carried out on a VG Scientific ESCA-3 Mk-II spectrometer having as X-ray source the Al Kα radiation (1486.6 eV, non-monochromatic) of an anode operating at 14 kV and 20 mA.

The magnetic measurements were performed by using a Cryogenic Limited Vibrating Sample Magnetometer (VSM).

3. Results and discussion

The analysis of TEM images shows the formation of nanoparticles (Fig. 1a) having two types of particle sizes distributions. A rough approximation of 2.5 -.3.5 nm for the thickness of the gold shell could be made by analyzing various HRTEM images.

The distribution upon diameters of the nanoparticles was determined for a number of 452 nanoparticles. In Fig. 1b one can observe the existence of two groups of nanoparticles with different sizes, one with a log-normal type distribution below 10 nm (centered at 5 nm) and another one centered at 25 nm.

Fig. 2 shows the XRD pattern of the core-shell Fe@Au nanoparticles. One can see the characteristic peaks for iron core and gold shell. From the X-Ray line profile analysis the effective nanocrystallites resulted are $<D_{Au}>$ = 24.5 nm for gold and $<D_{Fe}>$ = 14.6 nm for iron.

The distribution shown in Fig. 3 results from the distribution upon grain sizes in Fig. 1b by multiplying the diameter *d* at power *3* with the corresponding number of particles and normalizing to the total volume of the particles. From Fig. 3 one can see that most of the Au atoms (and by consequence the inner Fe atoms) are in large diameter grains, having a peak around 25 nm, in accordance with the mean diameter resulted from XRD line profile analysis. It should be noticed that as it concerns the number of nanoparticles having diameters below 8-10 nm are by far the dominant ones in number.

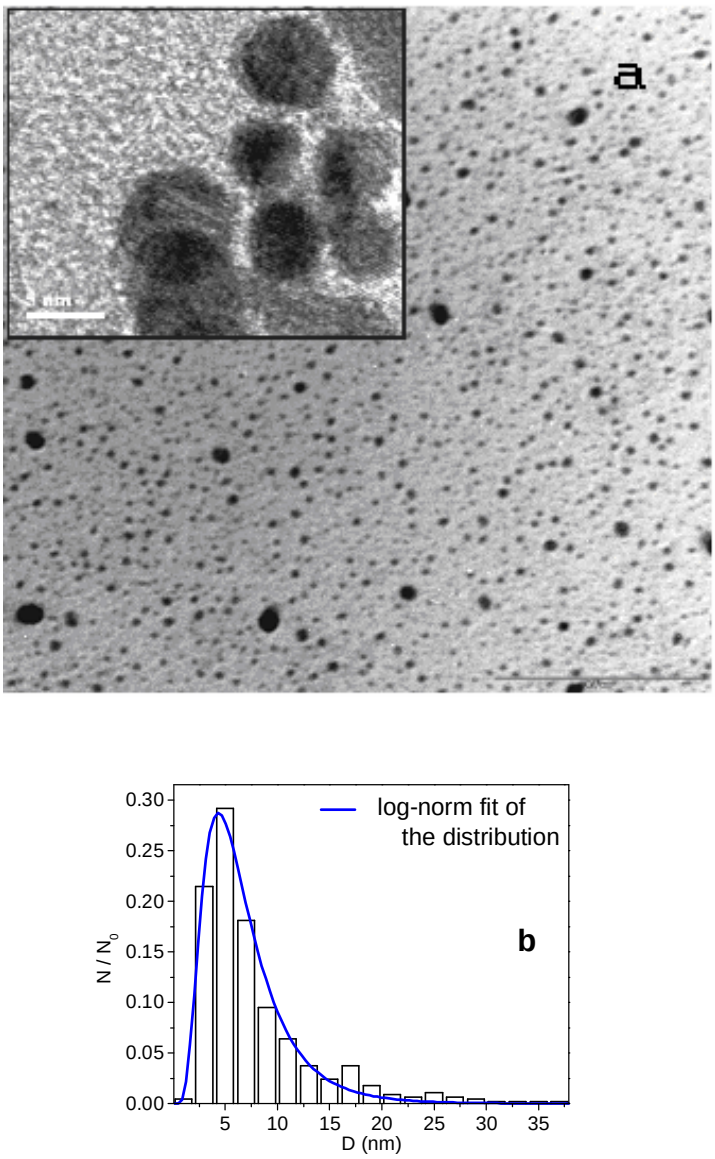

Fig. 1. (a) TEM image of the core-shell Fe@Au nanoparticles. Insert: HRTEM image of the core-shell Fe@Au nanoparticles (b) The size distribution of the Fe@Au nanoparticles

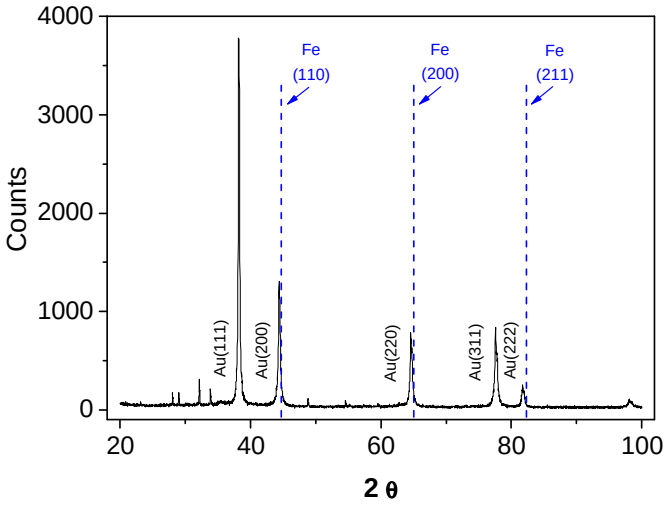

Fig. 2. XRD pattern of the core-shell Fe@Au nanoparticles

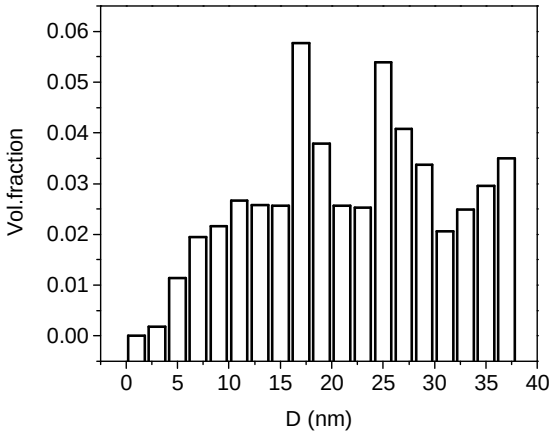

Fig. 3. Volume fraction distribution upon size of the nanoparticles

Fig. 4 shows the Fe 2p XPS spectra for the as-introduced sample (spectrum I) and after 1, 2 and 3 sputtering cycles (spectra II, III and IV respectively). Each of the spectra II, III and IV corresponds to around 2 nm of corrosion starting from the surface.

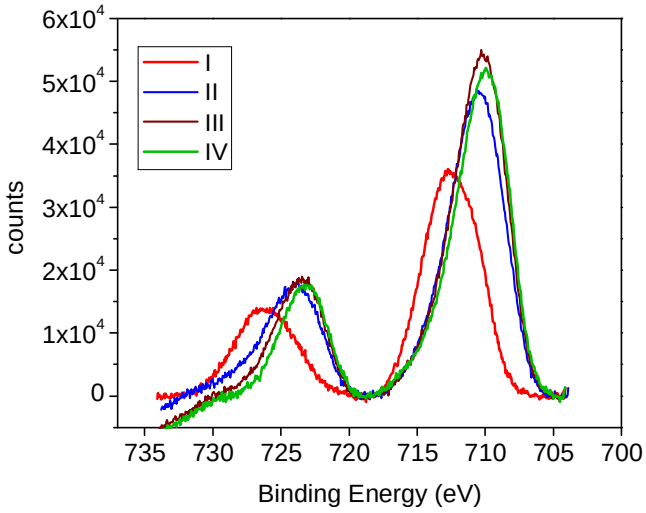

Fig. 4. The Fe 2p XPS spectra for the as prepared sample (spectrum I) and after 1, 2 or 3 sputtering cycles (spectra II, III and IV respectively). Each of the spectra II - IV corresponds to around 2 nm corrosion starting from the surface.

The parameters of the XPS spectra of the iron are summarized in Table 1. Analyzing the lines positions as shown in Table 1, one observe that the lines of XPS spectrum I have a chemical shift towards higher binding energies compared to the other spectra. This shift can be an indication for the presence of iron in the $Fe^{II,III}$ oxidation state. Thus, at the very surface of the sample, we infer the presence of Fe oxides, whose contribution disappears immediately after sputtering. As soon as the surface layer is eliminated by sputtering, even for the lowest amounts of corroded layers, the position of the Fe 2*p* levels approach very quickly the values of the corresponding lines in bulk clean Fe^0.

Table 1.

Characteristics of XPS spectra for iron in the core-shell Fe@Au nanoparticles

Recorded spectrum	Corrosion depth (nm)	Position of Fe $2p_{3/2}$ line (eV)
I	0	712.6
II	2	710.5
III	4	710.3
IV	6	710.0
bulk Fe^0	-	710.0

Since, after corrosion, the oxidized Fe quickly disappears from the spectra it seems to be located on the surface or into the cracks of the surface of the gold shell [7]. This is a proof that the chemical synthesis procedure leads to no oxidized core Fe atoms inside the Au nanoparticles.

From the variation of the Fe^0 2p line intensities before and after various corrosions one can estimate the thickness of the Au shell, δ_{Au}, as being 2 nm < δ_{Au} < 4 nm in accordance with the estimation made from HRTEM images.

The magnetization curve *vs.* the applied magnetic field at room temperature for the Fe@Au system is shown in Fig. 5. It does not show hysteresis loop, being typical for fine particles with superparamagnetic behavior. For such a system, above the blocking temperature the magnetic moment of the particle is free to rotate in response to the applied magnetic field.

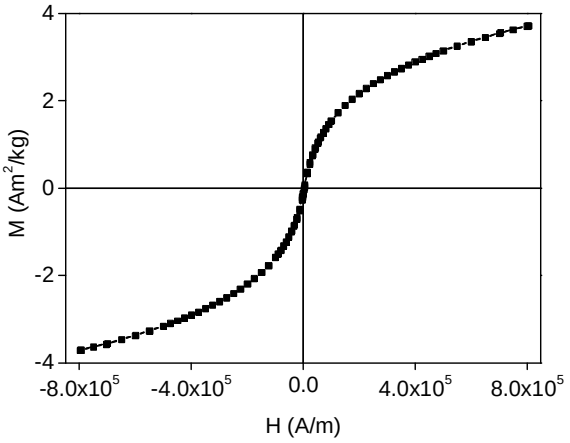

Fig. 5. The hysteresis curve measured at the room temperature for the Fe@Au system.

The field-cooled (FC) and zero-field cooled (ZFC) curves given in the Fig. 6 for the Fe@Au systems show that the blocking process for the majority of the superparamagnetic particles takes place at the temperature of 70K.

Generally, the blocking temperature is related to the particles mean volume, V by the relation [9]

$$T_b = \frac{KV}{25k_B}.$$

Here K is the anisotropy coefficient (K=4.2x10^4 J/m^3 for Fe [10]) and k_B is the Boltzmann constant. Accordingly, at the room temperature, the nanoparticles with the diameter of the magnetic iron cores D>15 nm should be blocked. Therefore only the fraction of nanoparticles having diameters smaller than 15 nm (10 nm diameter of iron cores) will contribute to the superparamagnetic behavior of the magnetization.

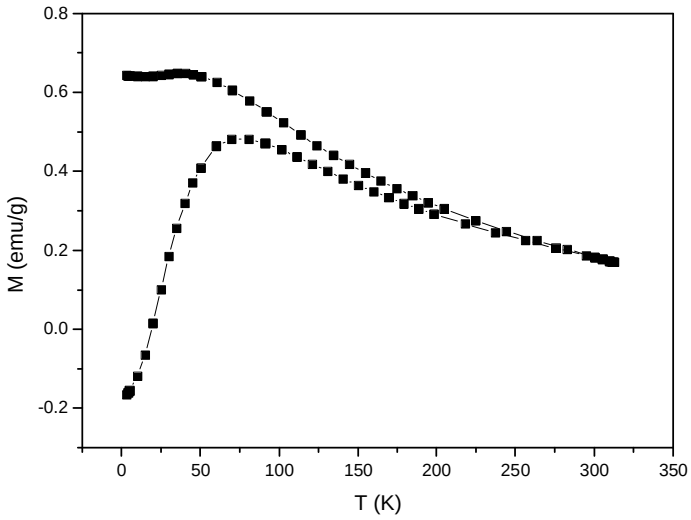

Fig. 6. Magnetization vs. temperature under field cooled (FC) and zero field cooled (ZFC) at 0.01T magnetic field for Fe@Au nanoparticles.

4. Conclusions

Core-shell Fe@Au nanoparticles were obtained by the inverse micelles method. We established that two distributions exist concerning the diameters of nanoparticles: one centered around 5 nm and another one centered at 25 nm, respectively. The majority of the nanoparticles are in the low diameters size distribution. As a consequence only large particles with diameters above 15 nm could be evidenced from the analysis of the XRD line profiles, because the majority of Au atoms (and probably of the Fe atoms) are within these large diameter particles. On the other hand, the magnetic properties of the system are determined only by low dimension particles which are dominant as a number.

XPS studies show that the inner cores of the nanoparticles are formed by Fe^0. Besides Fe^0 into the core the core-shell Fe@Au nanoparticles contain small amounts of FeO, and Fe_2O_3 which could appear on the gold nanoparticles surface inside the cracks and by contamination.

The missing hysteresis loop in the magnetization vs. applied magnetic filed represents a clear evidence for the superparamagnetic behavior for the core-shell Fe@Au nanoparticles. The superparamagnetic behavior is also evidenced from FC and ZFC dependences of the magnetization *vs.* temperature.

REFERENCES

[1] A. K. Gupta, M Gupta, Biomaterials **26**, 3995-4021(2005)

[2] M. Li, H. Schnablegger, S. Mann, Nature **402**, 393(1999)

[3] J. Chatterjee, Y. Haik, C. J. Chen, J. Magn. Magn. Mater. **246**, 382(2002)

[4] J. M. Vargas, L. M. Socolovsky, M. Knobel, D. Zanchet, Nanotechnology **16**, S285 (2005)

[5] A. K. Gupta, R. Naregalkar, V. D. Vaidya,M. Gupta, Nanomedicine **2**, 23-39(2007)

[6] O. Pana, C.M. Teodorescu, O. Chauvet, C. Payen, D. Macovei, R. Turcu, M.L. Soran, N. Aldea, L. Barbu, Surface Science **601**, 4352-4357(2007)

[7] S.J. Cho, A.M. Shahin, G.J. Long, J.E. Davies, K. Liu, F. Grandjean, S.M. Kauzlarich, Chem. Mater. **18**, 960(2006)

[8] C. Estournes, T. Lutz, J. Happich, T. Quaranta, P. Wissler and J. L. Guille, J. Mag. Mag. Mat. **173,** 83(1997)

[9] I.S. Jacobs and C.P. Bean , in G.T. Rado and H. Suhl (Eds.), Magnetism, Vol.3, Academic Press, New York 1963, p.271

[10] *See for example* C. Kittel, Introduction to Solid State Physics, J. Wiley & Sons, 1971, NY, London, Sydney, Toronto

STUDIA UNIVERSITATIS BABEŞ-BOLYAI, PHYSICA, LIII, 2, 2008

GC/MS ANALYSIS OF WINES

ANDREEA IORDACHE, MONICA CULEA, CAMELIA LEHENE, ONUC COZAR*

ABSTRACT. The analysis of organic compounds and some pesticides in different Romanian wines by gas chromatography-mass spectrometry (GC-MS) was performed in scan and selected ion monitoring (SIM) modes. Liquid-liquid extraction (LLE) and solid phase micro extraction (SPME) methods were used. The incorporated Rtx-5MS capillary column, 30mx 0.32mm, 0.25µm film thickness, was used in a temperature program from: 50 ^{o}C for 2 min, then increased to 310 ^{o}C with a rate of 10 ^{o}C /min. The required level for pesticides in drinking water and food, specified in EEC Directive explains the need for straightforward, selective and sensitive methods for trace level determination of these compounds in drinking water or beverages and the recent development of techniques in this area.

Keywords: Gas chromatography-mass spectrometry, Liquid-liquid and solid phase micro extraction method, wines, pesticides

Introduction

The fingerprint chromatograms could be used for comparison of wines and require simple extraction methods. Trace pollutants in the environment involve pretreatment: the extraction and concentration procedure for analysis at these concentrations, to increase the analyte concentration to within instrument sensitivity. Residual determination of pesticides at the levels required a preconcentration step before chromatography analysis. The preconcentration step could be: (1) solvent extraction, (2) headspace analysis, (3) purge and trap, (4) solid phase extraction (column and discs) (5) solid phase microextraction (SPME).

A typical pre-treatment would be as follows: (1) Extraction of the organic components into a suitable solvent; (2) Drying the solvent using a column containing 5g of sodium sulphate; (3) further concentration of the extract to 1 ml by partially evaporation by bubbling dry nitrogen or argon through the sample; (4) clean-up of the extract by column chromatography.

80/778/EEC Directive [1, 2] sets a maximum admissible concentration (MAC) of 0.1 $\mu g/l^{-1}$ for individual pesticides and of 0.5 $\mu g/l^{-1}$ for total pesticides in drinking water [1] and of 1-3 $\mu g/l^{-1}$ in surface water [3-6]. The majority of pesticides discharged in aquatic environment of the Community listed in the 76/464/EEC Council Directive (so-called black list) are organophosphorus pesticides [3,6]. A continue

revision of the methods for the determination of organic components in water or food is necessary. GC-MS is the most widely confirmation technique. EPA and UK Standing Committee of Analysis (SCA) methods have already implemented GC-MS in some of their protocols (EPA Method 525) [7-14].

Materials and method

The wine (Jidvei white wine) samples were from the market. Pesticides were obtaine from Merck (Germany).

Extraction procedures

Liquid-liquid extraction. Liquid-liquid extraction (LLE) followed some steps: the sample was shaken with an immiscible organic solvent in which the components are soluble as light petroleum/ dichloromethane(3:1) [9]. The organic layer was separated and after concentration was injected in the chromatograph. By altering the pH of the aqueous layer the extraction can be made selective towards acidic and basic components. The aliquot of sample was shaken with an equal volume of the light petroleum in a capped vial, three times, by using three portions of solvent. LLE was laborious, time consuming, subjected to emulsification and contamination. For polar pesticides polar solvents like acetonitrile, methanol, nitromethane, dimethyl-acetamide, dimethylformamide, dichloromethane/ethyl acetate(1:0) were used.

Solid-phase extraction Solid-phase extraction (SPE) is an alternative to LLE.

(1) Adsorption: The most commonly used contains octadecylsilane (C18), a column in the form of a packed cartridge containing suitable sorbent (200 mg) to trap the analyte, a plastic syringe and a filter of 0,4 µm to avoid impurities to stop the flux of sample by cartridge. The sample and solvent flowed through the sorbent by gravity or by positive (syringe) pressure.

The SPE sequence involved the following steps: (1) activation (conditioning) of the sorbent (wetting with the appropriate solvent), (2) sample introduction, (3) washing of the bonded phases, (4) elution of the retained pesticides, (5) regeneration of the column. Ethyl acetate was used as solvent for desorption. The sorbent ethylvinylbenzene-divinylbenzene copolymer LiChrolute EN, a copolymer with a specific surface area of cca 1200 m^2/g, due to its microporous structure was also used. Recovery values obtained for pesticides were of 85-100% .

Solid phase microextraction. Pawliszyn and co-workers [14] have introduced the solid phase microextraction (SPME). The SPME consists of a Hamilton syringe. A fused silica fiber coated with stationary phase (1 cm) is glued into a stainless steel tubing which enters in the syringe needle. The fiber was kept for 10 minutes into the headspace volume of the sample heated 1 hour at 70°C. Stationary phases investigated: polydimethylsiloxane (PDMS), thickness 100 µm. Desorption was made by direct injection into the injector port for 2 minutes.

Apparatus

Gas chromatograph-mass spectrometry (GC-MS) is a high sensitive and specific technique for use in the environmental organic analysis to identify compounds. GC is used for separation of the mixture. Into the MS the compound is ionized under high vacuum, often using electron impact, inducing fragmentation of molecules. The ions produced are focused into a beam, accelerated and then separated according to their mass to charge ratio, m/z. The method of identification is to compare the mass spectrum of the sample with that from a reference NIST or Willey library. In the selective ion monitoring (SIM) mode, using a few selected ions, the sensitivity is increased by one or two orders of magnitude.

Results and Discussion

A Trace DSQ ThermoFinnigan quadrupole mass spectrometer in the EI mode coupled with a Trace GC was used. The capillary column Rtx-5MS had 30 m in length, 0.25 mm as diameter and a film thickness of 0.25µm. The experiments were performed by using a temperature program from 50°C (2 min) to 310°C with 10°C/min, kept 15 minutes at final temperature. Helium (5.5) carrier gas had a flow rate of 1 ml/min. The qualitative analysis was carried out in the 50-500 a.m.u. mass range. The following conditions were ensured: transfer line temperature 250°C, injector temperature 200 °C, ion source temperature 250 °C, splitter 10:1, electron energy 70eV and emission current 100µA.

In the SIM mode, the typical fragment ions obtained in EI mode for pesticides have been used. (Table 1).

Table 1

Fragment ions and relative abundances(%) in mass spectra of pesticides by GC/MS analysis

Compounds	MW	m/z relative intensity (%) of the main ions	
		EI	NCI
Azinphos-ethyl	345	104(19),132(100),160(82)	185(100)
Chlorpyryfos	349	97(59),125(22),197(100),258(37),314(33)	169(23),212(40), 313(100)
Coumaphos	362	89(310,97(94),109(100),210(56),226(49) 362(79)	169(6),362(100)
Demeton	258	109(47),125(39),169(100)	169(15),187(100)
Diazinon	304	93(29),137(100),152(74),179(98),199(59) 304(22)	169(100)
Dichlorvos	220	79(18),109(100),185(30)	125(100),134(58), 170(80)
Disulfoton	274	88(100),97(31),125(26),147(27),153(27), 185(25)	185(100)
Ethoprophos	242	97(57),126(48),139(46),158(100),200(31)	199(100)

Compounds	MW	m/z relative intensity (%) of the main ions	
		EI	NCI
Fenamiphos	303	122(29),154(100),217(54),260(30),288(31), 303(97)	153(100)
Fenchlorphos	340	79(17),109(28),125(65),285(100)	141(20),211(100), 270(54)
Fenitrooxon	261	109(97),127(20),244(100),261(12)	261(100)
Fenitrothion	308	95(58),109(48),125(81),139(39),140(82), 141(64),153(34),156(100),293(84)	169(100),293(8)
Fensulfothion	308	97(58),109(48),125(81),139(39),140(82), 141(64),156(100),293(84)	169(100),293(8)
Fenthion	278	125(78),278(100)	
Fonofos	246	109(100),137(57),246(36)	109(39),169(100)
Isofenphos	345	232(88)	
Malaoxon	314	99(23),109(19),125(25),127(100),142(16), 173(12),195(17)	141(100)
Malathion	330	93(40),125(85),127(93),158(43),173(100)	157(100)
Mevinphos	224	192(23),224(4)	
Monocrotophos	223	127(100),223(3)	
Paraoxon-ethyl	275	81(38),109(100),127(27),139(51),149(66), 220(26), 247(25),275(27)	275(100)
Paraoxon-methyl	247	79(15),96(41),109(100),230(36),247(25)	247(100)
Parathion-ethyl	291	97(83),109(100),125(49),139(67),155(54), 186(29)	154(100)
Phorate	260	75(100),97(27),121(58),260(20)	185(100)
Phosmet	317	77(4),93(4),160(100),317(2)	157(100)
Pyridafenthion	340	77(30),97(68),125(47),188(89),199(100), 204(58),349(79)	169(40),340(100)
RPA-400629	368	97(25),109(24),121(31),153(14),171(100), 215(30),233(11)	169(49),185(100)
Stirofos	366	79(11),109(100),331(66),	125(100)
Vamidothion	287	58(13),60(15),87(100),109(39),125(20), 142(39),145(74),169(26)	141(100)
Penconazole	283	159(100), 248(70), 161(65), 250(24)	
chlorothalonil	264	266 (100), 264 (73), 268 (49)	
folpet	295	260 (100),262 (71),104(57),76(55),295 (20)	
propargite	350	135(100), 81(18), 173(15), 350 (2)	
iprodione	329	56(100), 43(92), 314(41), 187(26)	

A comparison of the compounds identified in the LLE extracts of the studied white wines of Jidvei vineyard: Sauvignon Blanc, Feteasca Regala and Riesling is presented in Table 2 and Fig. 3.

The pollutants preliminary study was applied for SIM detection from wine for some pesticides as penconazole (1), chlorothalonil (2), folpet (3), propargite (4) and iprodione (5), dimethoate (6), having the information thet they are used in Jidvey vineyard. The molecular mases and the important ions from the mass spectra are

presented in Table 1. The SIM mode was used by selecting ions from the mass spectra for residual determination of different pesticides. The baze peak ions were especially used for SIM mode measurements, as shown for the base peak of dimethoate, m/z 87, in Fig.1 and for some others in Fig. 2.

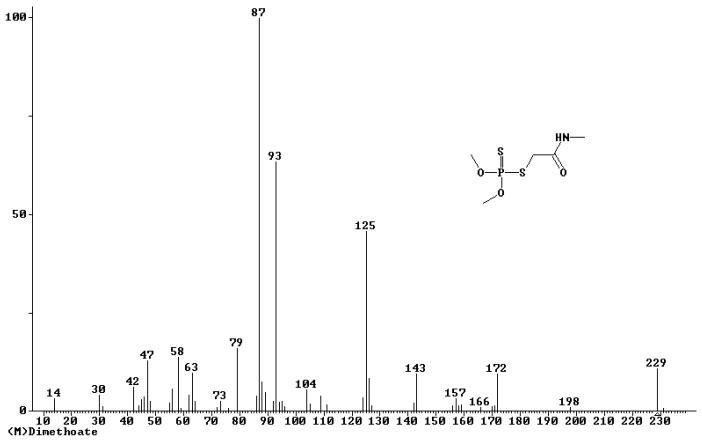

Fig. 1. The mass spectrum of dimethoate

Table 2.

Comparison of LLE extraction of white wines: (SB)Sauvignon Blanc, Feteasca Regala (FR) si Riesling de Jidvei

RT	Name	M	Area % (SB)	Area % (R)	Area % (FR)
3.15	Benzene	78		9.47	9.63
3.23	Propanamide, 2-hydroxy-	89	1.06	0.03	0.0
3.32	2-butanone, 4-hydroxy-	88		0.09	0.08
3.44	2-butanone, 4-hydroxy-	88		0.38	0.47
3.63	Acetic acid	60	2.18	0.06	2.68
3.82	Ciclohexane, methyl	98		2.60	
4.02	1-Butanol, 3-methyl-	88	3.74	30.85	34.09
4.49	1,2-Propanediol, 3-methoxy-	106	0.07	0.23	0.02
4.74	toluene	92		1.47	1.57
5.18	Propylene Glycol	76	0.53	1.37	2.34
5.57	Ethyl butyrate	116		0.12	0.23
5.90	Propanoic acid, 2-hydroxy-, ethyl ester, (S)-	118	4.48	2.60	3.36
6.10	2,3-Butanediol, [R-(R*,R*)]-	90	2.60		
6.47	Furfural	96	2.07		
7.51	1-hexanol	102		0.93	0.97
7.66	2-Furanmethanol	98	0.41		
7.77	Amyl acetate	130		0.18	0.20
8.18	Pentyl acetate	130		0.05	1.06
8.92	Methyltartronic acid	134	4.63	0.29	0.3

RT	Name	M	Area % (SB)	Area % (R)	Area % (FR)
9.47	Butanoic acid, 4-hydroxy-	104	0.16		
9.47	Butyrolactone	86	0.16		
9.82	Butanoic acid, 3-hydroxy-,ethyl ester	132	0.02		
10.14	2,3-Dehydro-4-oxo-á-ionol	206	0.05		
10.35	4-ethylbenzoic acid,2-pentyl ester?	220	0.92		0.09
10.35	1,3-Dioxolane, 2-cyclohexyl-4,5-dimethyl-	184	0.92		
10.35	2-Oxopentanedioic acid	146	0.92		
10.66	2-Furancarboxaldehyde, 5-methyl-	110	0.74		
10.83	Disiloxane, 1,3-diethoxy-1,1,3,3-tetramethyl-	222	0.29		
10.95	Guanosine	283	0.03		
11.21	Hexanoic acid	116	2.16	0.85	0.90
11.50	Hexanoic acid, ethyl ester	144	0.26	0.76	0.91
11.64	2H-Pyran-2,6(3H)-dione	112	0.16		
11.77	á-D-Glucopyranose, 4-O-á-D-galactopyranosyl-	342	0.02		
12.16	Benzyl alcohol	108	0.04	0.03	
12.67	benzenacetaldehyde	122	0.97	0.05	0.05
12.95	Ethyl 2-hydroxycaproate	160		0.17	0.4
13.23	2-furancarboxylic acid	112		0.18	0.16
13.60	Furyl hydroxymethyl ketone	126	1.32		
14.15	Phenetyl alcohol	122		20.43	14.85
14.47	Glycerin	92	39.65	0.15	
14.61	methylbutylacetamide	129		0.35	0.24
14.82	4H-Pyran-4-one, 2,3-dihydro-3,5-dihydroxy-6-methyl-	144	10.17		
15.29	Butanedioic acid, diethyl ester	184		11.5	7.26
15.69	Octanoic acid ethyl ester	172	0.08	0.86	0.54
15.76	Amino-pentanedioic acid	175		0.53	
15.95	Butanedioic acid (succinic acid)	118	4.03	01.07	1.59
16.19	2-Furancarboxaldehyde, 5-(hydroxymethyl)-	126	1.49		
16.44	2,3-Dihydroxy-2-methylpentanoic acid	148	0.62	0.03	
16.58	Phenylethyl hexanote	220		0.12	0.1
16.72	Butanedioic acid, hydroxy-, diethyl ester	190	2.51	2.00	3.37
16.99	malic acid mono ethyl ester?	134	4.25	2.56	4.21
17.29	5-Hydroxymethyldihydrofuran-2-one	116	0.31	0.59	
17.63	Malic Acid	134	4.25		
18.09	n-decanoic acid	172	2.07	0.97	1.17
18.30	Succinoic acid, 2-hydroxy, 3-methyl-, diethyl ester	204	0.04	0.34	0.31
18.48	Ethyl decanoate	200	0.05	0.10	0.11
18.49	5-Oxotetrahydrofuran-2-carboxylic acid, ethyl ester	158	2.38		
19.19	alpha-D-Glucopyranose, 4-O-alpha-D-galactopyranosyl-	342	1.33		
19.32	Benzeneethanol, 4-hydroxy-	138	1.12	3.54	3.98
19.55	Benzenepropanoic acid, hydroxy ethyl	194	0.59	0.35	
19.81	Phenol, 3-methoxy-2,4,6-trimethyl-	166	0.07	0.02	.37

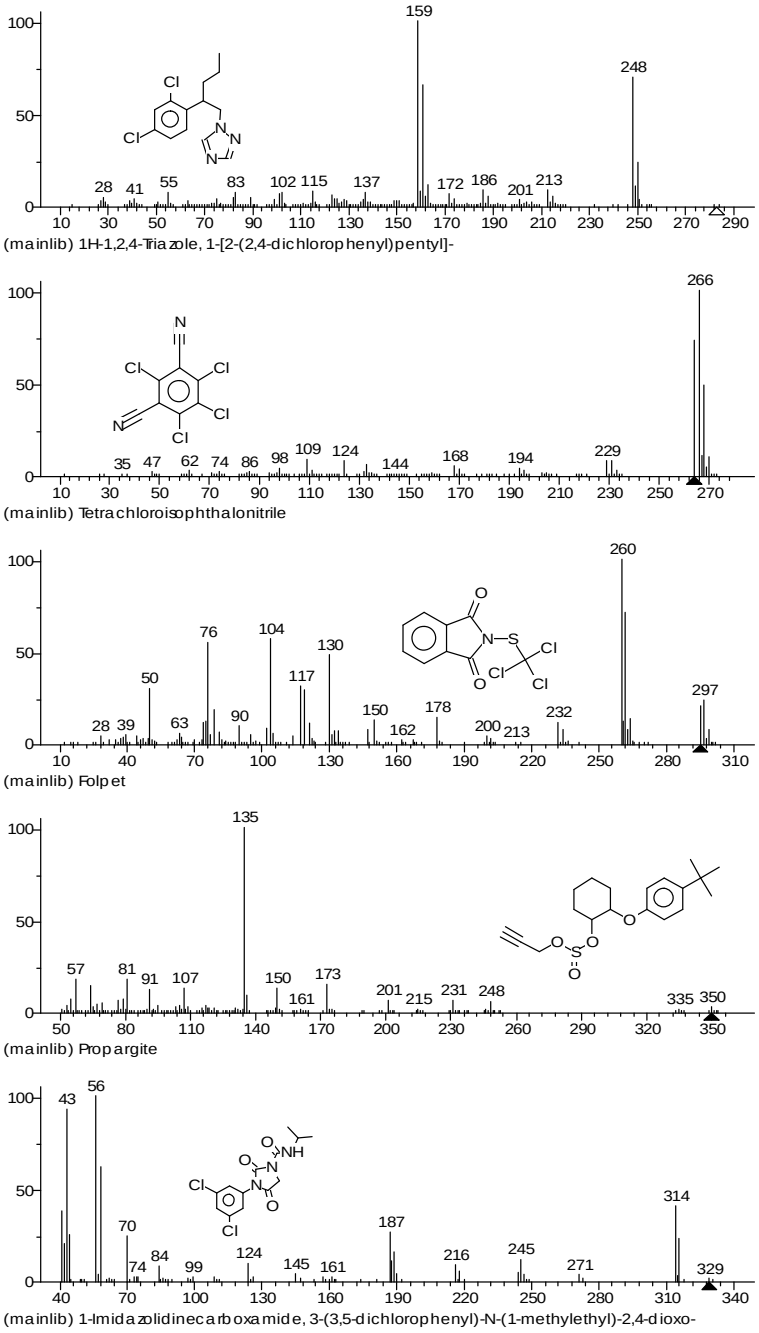

Fig. 2. The mass spectra and formula for some the fungicides studied

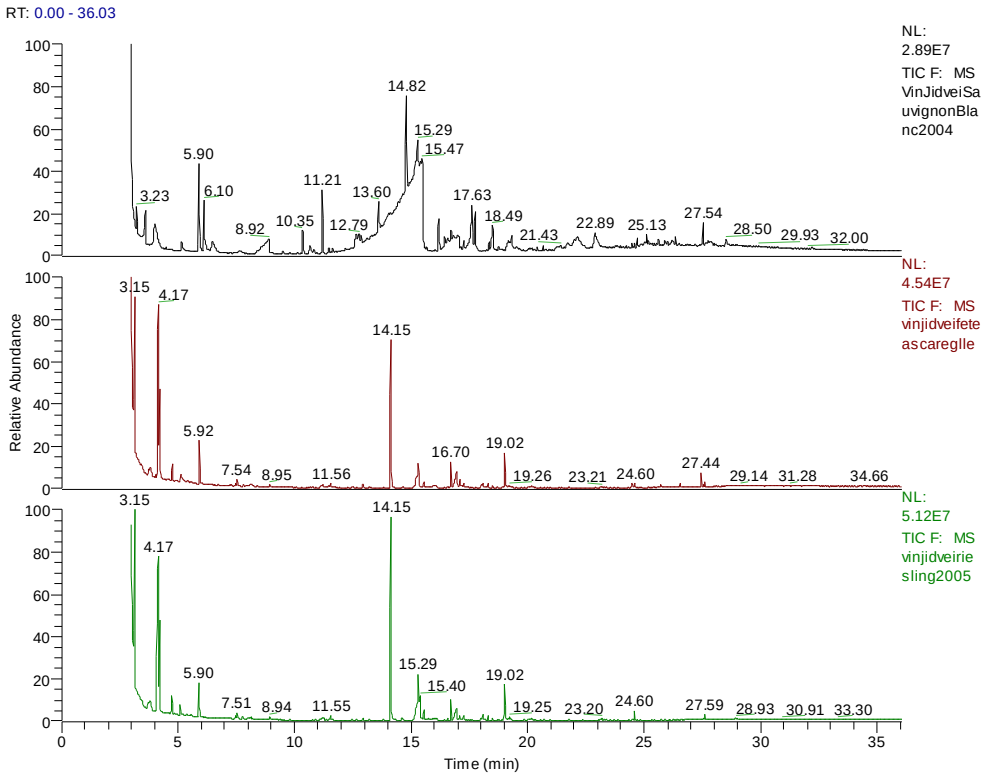

Fig. 3. The chromatograms of liquid-liquid extracts (LLE): Sauvignon Blanc is different, Feteasca Regala and Riesling, are similar. (Rtx-5MS, 30m x 0.25 mm, film thiekness 0.25µm. Temperature program from 50°C (1 min) to 310°C, with 15°C/min).

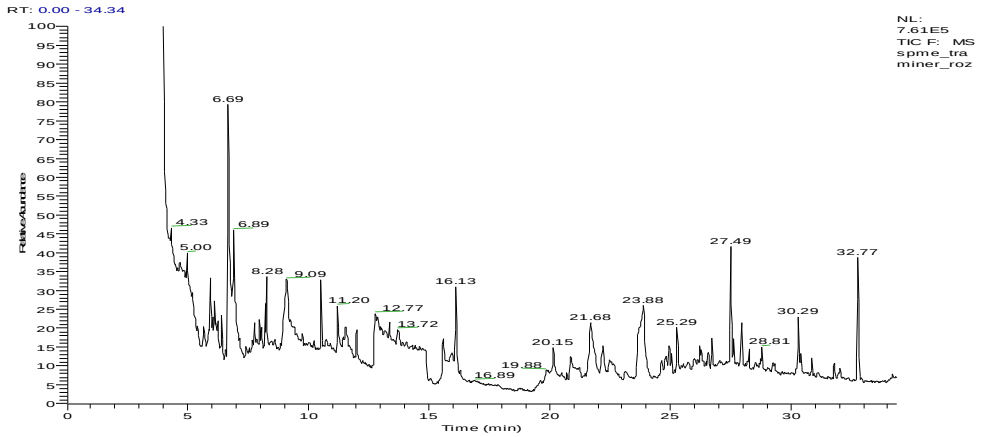

Fig. 4. SPME-GC-MS chromatogram of the Traminer Roz wine (Jidvei).

The solid phase micoextraction (SPME) of a Jidvei wine, Traminer Roz, in the SIM mode, is presented in Fig. 4. The base peaks of the fungicides of interest were selected in the analytical method and analysed. Elution order was dimethoate (13.9 min), chlorothalonil (15.1 min), cyprodinyl (17.2 min), penconazole (17.35 min), folpet (17.65 min), propargite (20.31 min) and iprodione (20.75 min).

Our preliminary results showed lower values than 100µg/l for the tested pesticides in some wight wines of Jidvei vignard selected from the market, the limit of detection being 10 µg/l.

Conclusions

The extraction methods described are useful for rapid characterization of wines (GC fingerprint) but also for their detailed characterization. GC-MS method is the best for volatile organic compounds characterization and active principles of wines. The samples of wines have different compounds but especially are quantitatively different.

The compounds of high toxicity are needed to be analyzed at very low concentrations by using SIM mode. Ultra-trace analysis includes concentration ranges of pollutants of ng/kg or pg/kg. The analysis not only requires highly sensitive and selective instrumentation but also a large degree of analytical skill and expertise. Such low concentration is important to be measured because the concentration can be easily increased in an organism compared with the environment in which it is living.

REFERENCES

1. *EEC Drinking water Guidelines*,80/779/EEC NoL229/11-29,EEC, Brussels, 1980, pp 1-20.
2. M Fielding, D Barcelo, A Helweg, S Calassi, L Torstensson, P Van Zoonen, R Wolter, G Angeletti. *Water pollution research. Report 27. Commission of the European Communities*, Brussels,1992.
3. S Hatrik, J Tekel.. J ChromatogrA 733, 217 (1996).
4. C Molina, P Grasso, E Benfenati, D Barcelo. J ChromatogrA 737, 47 (1996).
5. D. Barcelo. Trends Anal Chem 10, 323 (1991).
6. D. Barcelo. J Chromatogr 643,117 (1993).
7. US Environmental Protection Agency. *Methods for the determination of Organic compounds in drinking water, supplement* 1, PB91-140627, National Technique Information Service, Springfield, VA, 1990.
8. US Environmental Protection Agency. *Methods for the determination of Organic compounds in drinking water, PB91-231480*, National Technique Information Service, Springfield, VA, revised, 1991.

9. I Tolosa, JW Readman, LD Mee. J ChromatogrA 725, 93 (1996).
10. M. Culea, S. Gocan, *Handbook of water analysis, Organophosphates*, Ed. Leo Nollet, Marcel Decker, p.571-608, 2000
11. J Slobodnik, AC Hogenboom, AJH Louter, UAT Brinkman. J Chromatogr A 730, 353 (1996).
12. M Culea, I Fenesan, S Cobzac, S Gocan, M Chiriac, N Palibroda. Fresenius'J Anal Chem 335, 748 (1996).
13. C.van Doorn, M. Vink and J. M. van der Poll, Chromatographia, 40, 458 (2005).
14. S Magdic, A Boyd-Boland, K Jinno, JB Pawliszyn. J ChromatogrA 736, 219 (1996).
15. Andreea Iordache, Monica Culea, Onuc Cozar, "Chemické listy" Journal, 102, s667 (2008).

STUDIA UNIVERSITATIS BABEŞ-BOLYAI, PHYSICA, LIII, 2, 2008

STATISTICS FOR CIRRHOSIS DIAGNOSIS BY GC/MS

ANDREEA IORDACHE, CORNELIA MESAROS, MONICA CULEA, ONUC COZAR*

ABSTRACT. Gas chromatographic-mass spectrometry (GC/MS) is one of the best methods used for measuring drugs in biological fluids. The selected ion monitoring (SIM) mode was used in caffeine test measurements by adding known amounts of ^{15}N-theophylline as internal standard. A single dose of 4 mg.kg^{-1} p.o. of caffeine was followed by blood concentrations measurements at two points, 1h and 9 h. Caffeine clearance, measured in patients with cirrhosis and chronic hepatitis, was reduced and half live time was increased in children with liver disease as compared with control. Different statistical methods have been used to study the pharmacokinetic data for cirrhosis diagnosis.

Keywords: Gas chromatographic-mass spectrometry, statistical methods, diagnosis

Introduction

Caffeine is used for measuring the metabolic capacity of the liver. Because caffeine is metabolized by the hepatic P-450 cytochrome oxidase system, clearance of caffeine is an excellent quantitative test of hepatic function in human beings. Caffeine test consists in caffeine oral intake followed by measurements of blood caffeine concentration. Gas chromatographic-mass spectrometric (GC/MS) applications for measuring drugs are very important for pharmacokinetic studies, metabolic studies, clinical applications for treatment and diagnosis [1-3, 5-8].

The aim of this work was the statistical study of data obtained by GC-MS measurements of caffeine concentration and some pharmacokinetic parameters. The pharmacokinetic parameters as plasma clearance and half-life time of caffeine in children with hepatic dysfunctions and control have been compared.

Materials and methods

Equipment:

A Hewlett Packard mass spectrometer (Palo Alto, CA, USA) HP 5989B couplet with a gas chromatograph HP 5890 was used in the conditions: electron energy of 70 eV, electron emission of 300μA and ion source temperature of 250^{o}C, selected

* *Babes-Bolyai University, Biomedical Physics Dept., 1 Kogalniceanu str, 3400 Cluj-Napoca, Romania, e-mail: mculea@phys.ubbcluj.ro*

ion monitoring (SIM) mode. The gas chromatograph-mass spectrometer (GC/MS) assay used a HP-5MS fused silica capillary column, 30m x 0.25 mm, 0.25µm film-thickness, programmed from 200 ^{o}C to 250 ^{o}C at a rate of 10 ^{o}C/min, the flow rate 1ml.min^{-1}, with helium 5.5 as carrier gas. Injector temperature was 200 ^{o}C. Retention time for caffeine and ^{15}N-theophylline, the internal standard, were 3.5 min and 2.8 min. 3 µl of sample were injected. The molecular ion m/z 194 for caffeine and the molecular ion m/z 181 for the internal standard were monitored for quantitative analyses in the selected ion monitoring (SIM) mode.

Extraction procedure:

0.5 ml of plasma containing caffeine was placed into a 5 ml screw-cap vial and 5µl of internal standard ^{15}N-theophylline, 1 ml of the extraction solvent, chloroform: isopropanol 20:1 v/v and 0.2 g NaCl were added. After mechanical mixing for 1 min, the sample was centrifuged for 3 min. 3 µl were injected into the GC from the lower layer.

The method was validated in the range 0-20µg.ml^{-1} of caffeine. The regression curve, plotted as peak-area ratio of m/z 194 to m/z181 versus caffeine concentration, gave the following linearity parameters: slope 0.5207, intercept 0.1058, and regression coefficient r = 0.97.

Precision gave R.S.D. values lower than 5% for 5µg.ml^{-1} (n=7) and lower than 3% for 3µg.ml^{-1} (n=5). Accuracy showed values lower than 10%. The limit of detection was 0.1µg.ml^{-1} caffeine in blood sample, signal to noise ratio 4:1.

Caffeine concentration measurements were performed in 29 hospitalized children suffering of hepatic dysfunctions and controls. Three different groups were studied: one formed by 16 children with hepatitis aged 3-19 years old, the other consisting from 5 children with cirrhosis, aged between 5-12 years old, and 8 children as control aged between 5-15 years old. The main dose was 4 mg.kg^{-1} p.o. for all groups. Blood samples were taken at 0, 30 min, 1, 3, 6, 9 and 12 h. Blood samples were drawn into heparinzed plastic tubes and immediately centrifuged. Plasma was stored at - 20 ^{o}C. Written informed consents were obtained from each subject parent prior to this study.

Calculation:

Regression curves obtain by the GC/MS method in the SIM mode was used for pharmacokinetic parameters study. Caffeine elimination constant was calculated as follows:

$$k_{el} = (\ln C_1 - \ln C_2)/\Delta t$$

Where

C_1=higher caffeine blood concentration

C_2=lower caffeine blood concentration

Δt= the time elapsed between venous blood samples

Two points caffeine clearance was calculated as $Cl = k_{el} \times V_d$ and caffeine half-life as $t_{1/2} = \ln 2/k_{el}$, using a constant volume of distribution (V_d) of 0.6 liters per kg body weight. Clearance values calculated as dose/area under curve (AUC) were compared with the two-points calculation values.

Statistical Assessment:

A limit may have to be set for the confidence level for the experimental mean within which there is a known confidence of determining the true mean. For a large number of samples determined, the experimental mean will follow a normal distribution. For small number of samples (n<30), the experimental mean will follow a t-distribution; hence the t-distribution can be used for calculating a confidence interval for an experimental mean using the relationship:

$$\bar{x} \pm \frac{ts}{\sqrt{n}} \tag{1}$$

where $\bar{x}$ is the experimental mean, t is the statistical factor derived from the normal error at various confidence levels, s is the calculated standard deviation, and n is the number of results. The t-distribution also offers a means of comparing the experimental mean with a specified standard mean or standard value.

When it has been established that the standard deviation of the two sets of data agree to a reasonable level of confidence, the appropriate t-test can then be used for comparison of the experimental means with other means using any of the appropriate equations relating t to the standard deviation s.

The t-test will indicate whether the numerical difference between the experimental mean and the set standard value is significant or not. This could be done using the following equation, in which the value of t is calculated and compared with those of t-critical tabulated in Tables at various confidence levels:

$$t = \frac{(\bar{x} - \mu)\sqrt{n}}{s} \tag{2}$$

In this case μ is the true mean or the accepted standard**.** For a given number of degrees of freedom, if the calculated value of *t* exceeds *t*-critical derived from the tabulated values in the distribution table, the difference between the experimental mean and the accepted standard is considered significant. Comparison of two sets of data obtained for the same type of parameter for two different groups of patients can be carried out to see if there is any significant difference between the two experimental means. This is important if one of the group samples was used as the control while a set of data was also obtained for the other. The following equation can be used for the purpose of comparison:

$$t = \frac{\overline{x_1} - \overline{x_2}}{\sqrt{\frac{s_1^2}{n_1} + \frac{s_2^2}{n_2}}} \tag{3}$$

$$\text{Degree of freedom} = \left\{ \frac{(s_1^2/n_1 + s_2^2/n_2)^2}{\frac{(s_1^2/n_1)^2}{n_1+1} + \frac{(s_2^2/n_2)^2}{n_2+1}} \right\} - 2 \tag{4}$$

$$t = (\overline{x_1} - \overline{x_2}) / s\sqrt{(1/n_1 + 1/n_2)} \tag{5}$$

Results and discussion

Caffeine clearance (Fig. 1) measured in patients with cirrhosis and chronic hepatitis was reduced and half live time was increased in children with liver disease compared with control.

The clearance was calculated in two ways, by using only two blood collection at overnight distance or by using seven collections of blood.

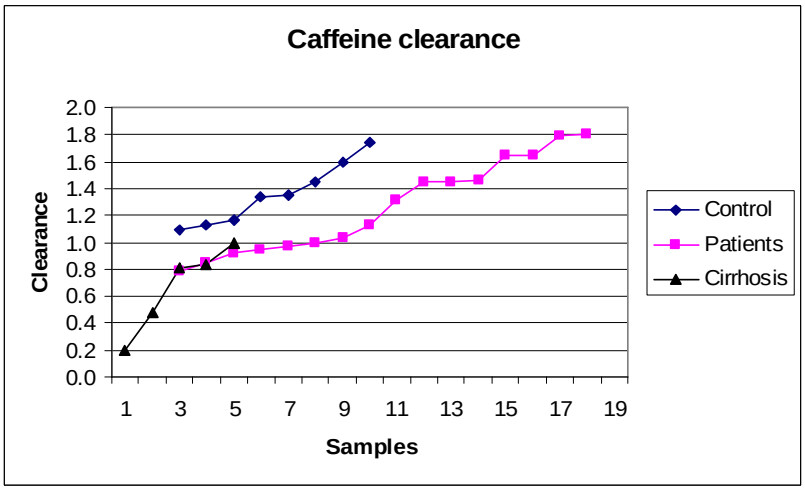

Fig. 1. Caffeine clearance values in control and patients

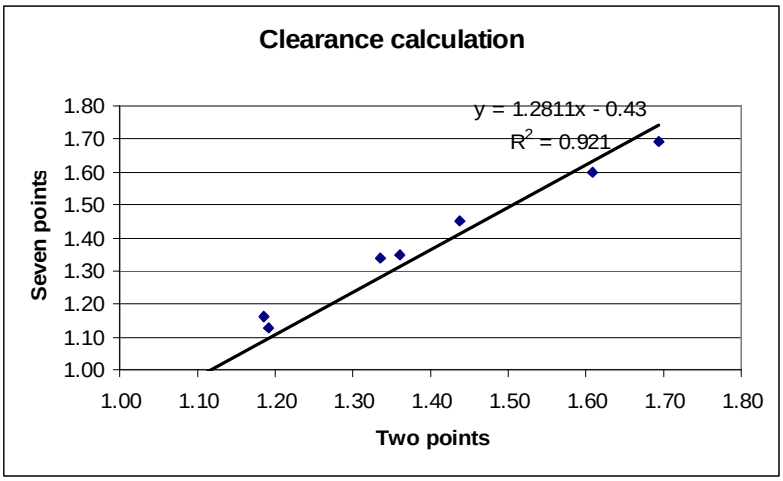

Fig. 2. Correlation between two and seven points clearance calculation (r=0.96)

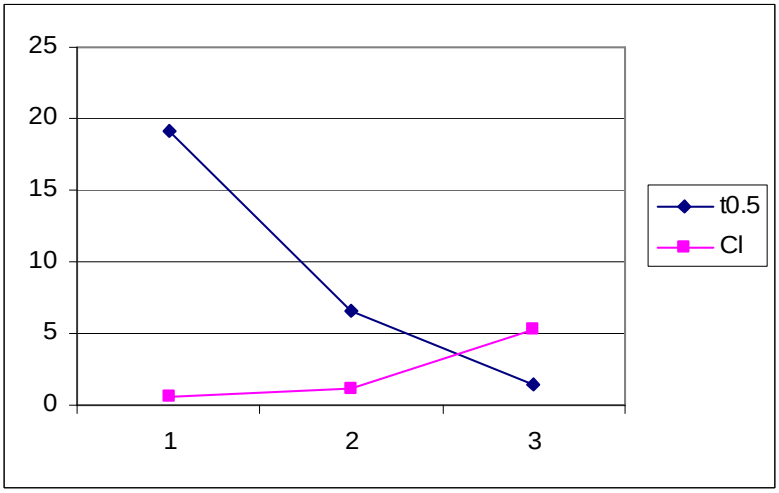

Fig. 3. The mean values of clearance and half time $t_{1/2}$ in the three groups of cases studied. Caffeine clearance measured in patients with cirrhosis (1) and chronic hepatitis (2), was reduced and half live time was increased in children with liver disease compared with control (3)

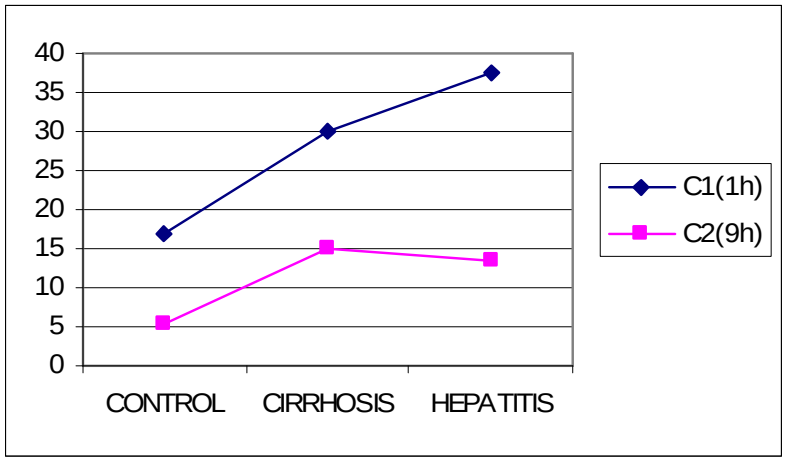

Fig. 4. Comparative mean value of caffeine concentration after dose, two point case, at the first hour and overnight

The data for caffeine clearance obtained by using two and seven points were compared. The data showed good correlation, a regression coefficient of 0.96. Fig. 2 presents the regression curve obtained by using the two way of clearance calculation.

Fig. 3 presents the mean value for the two pharmacokinetic parameters in disease compared with control. Interesting value shows the mean value for caffeine concentration in blood at the first hour after caffeine administration which is very high in hepatitis in comparison with control and cirrhosis (Fig.4).

By using Pearson test for the comparison of the results of caffeine clearance obtained by calculation of data for two points and seven points for plasma samples we have obtained no difference between the two sets of values. GraphPad showed also the same results demonstrating that two point collection of blood are sufficient.

The statistical calculation of Student t-test value and probability value p were compared with the theoretical values. Similar results for all the statistical method used were obtained.

The comparison of means of two samples [4] was tested, the patient groups and control. Clearance, half-life values for caffeine and t-test values calculated in the three groups of children are presented in Table 1.

The t-test values were calculated by using the formula (5) and gave the values in the last two columns of Table 1. Comparable results were obtained by using formula (2): 5.11 and 0.57 for clearance for cirrhosis and hepatitis and 2.58 and 1.19 for half life in the two diseases. The significance of the calculated t values was obtained by comparison with the theoretical values from Table 2 and 3.

Table 1.

Student t-test values calculated in the case of caffeine test (n_1=control, n_2=cirrhosis, n_3=hepatitis)

			Clearance	$t_{1/2}$	s	s	/t/	/t/
n_1	8	x1,s1	1.36	5.23	0.23	0.85	Cl	t1/2
n_2	5	x2,s2	0.60	15.58	0.30	11.63	5.11	2.58
n_3	16	x2,s2	1.26	6.16	0.45	2.12	0.57	1.19

Table 2.

The p values for clearance and half time

			p=0.1	p=0.05	p=0.02	p=0.01
n_1+n_2-2	11	cirrhosis	1.81	2.23	2.76	3.17
n_1+n_2-2	22	hepatitis	1.73	2.09	2.53	2.85
		Cl	$t_{1/2}$			
11	cirrhosis	p<0.01	p<0.05	Significant difference		
22	hepatitis	p>0.1	p>0.1	Not significant difference		

Table 3.

t-critical at various confidence levels

The number of degree of freedom k=n-1	Confidence level 90%	Confidence level 95%	Confidence level 99%	Confidence level 99.5%
1	6.317	12.706	63.657	127.32
2	2.920	4.303	9.925	14.089
3	2.353	3.182	5.841	7.453
4	2.132	2.776	4.604	5.598
5	2.015	2.571	4.032	4.773
6	1.943	2.447	3.707	4.317
7	1.895	2.365	3.500	1.029
8	1.86	2.306	3.355	3.832
9	1.833	2.262	3.250	3.690
10	1.812	2.228	3.169	3.581
15	1.753	2.131	2.947	3.252
20	1.725	2.086	2.845	3.153
25	1.707	2.060	2.787	3.078
	1.645	1.960	2.576	2.807

The results obtained by using the GraphPad soft were quite similar.

The GraphPad soft was applied for the same comparison of data. We have obtained t=5.088 for 11 degrees of freedom and p=0.0004 for clearance in cirrhosis, an extremely significant difference and t=2.577 for 11 degrees of freedom and p=0.0257

for $t_{1/2,}$ a significant result. For hepatitis, t=0.5677 for 22 degrees of freedom and p=0.576, is considered not significant for clearance and for $t_{1/2,}$ t=1.187 and p=0.248, also not significant differences.

Conclusions

The study showed significant difference of pharmacokinetics for two points sample collection for cirrhosis diagnosis. The elimination half-life ($t_{1/2}$) of caffeine was significantly longer in cirrhotic patients than in the other two groups and clearance was substantially reduced in these patients. These findings suggest that caffeine pharmacokinetic parameters can be estimated using two-point blood sampling procedure and GC/MS determination, following a single load. Further studies are intended for adults where the number of cases of cirrhosis is greater.

REFERENCES

1. M. Culea, D.L. Hachey, Rapid Commun. Mass Spectrom., 9, 655 (1995).
2. M. Culea, P. Panta, M. Nanulescu, N. Palibroda, O. Cozar, I. Vintilă, Balcanic Physics Letters, 5, 1861 (1997).
3. M. Culea, N. Palibroda, P. Panta Chereches, M. Nanulescu, Chromatographia, 53, S387 (2001).
4. J.C. Miller, J. N. Miller, *Statistics for analytical chemistry*, John Wiley&Sons, Chichester, England, 1986.
5. Cornelia Mesaros, Monica Culea, Eugen Culea, "Chemické listy" Journal**,** 102, s961 (2008).
6. G.J. Park, P.H. Katelaris, D.B. Jones, F. Seow, D.G. Le Couteur, M.C. Ngu, Hepatology 38, 1227 (2003).
7. H. Lelouet, Y.C. Bechtel, G. Paintaud, M.P. Brientini, J.P. Miguet, P.R. Bechtel, Int J Clin Pharmacol Ther. 39, 25 (2001).
8. Y.C. Bechtel, E. Haffen, H. Lelouet, M.P. Brientini, G. Paintaud, J.P. Miguet, P.R. Bechtel, Int J Clin Pharmacol Ther. 38, 467 (2000).

STUDIA UNIVERSITATIS BABEŞ-BOLYAI, PHYSICA, LIII, 2, 2008

X-RAY PHOTOELECTRON SPECTROSCOPY OF $MnSb_{1-x}Bi_x$

L. REDNIC[1*], M. COLDEA[1], V. REDNIC[1], M. NEUMANN[2], D. BENEA[1]

ABSTRACT. X-ray Diffraction (XRD) and X-ray Photoelectron Spectroscopy (XPS) of $MnSb_{1-x}Bi_x$ (x= 0, 0.2, 0.5 and 0.95) system are reported. Both MnBi and MnSb crystallize into two different phases: a hexagonal ferromagnetic nickel-arsenide (NiAs) structure type and an orthorhombic paramagnetic zinc-blende (ZB) phase. The zinc-blende structure of MnSb and MnBi is mechanically unstable and would transform spontaneously into a metastable denser tetragonal phase. The substitution of Sb by Bi in MnSb generates new compound which preserve the same hexagonal nickel-arsenide (NiAs) crystallographic structure type. The formation of $MnSb_{1-x}Bi_x$ phase is confirmed by X-ray diffraction measurements, valence band and core level XPS spectra.

Keywords: XPS spectra, nickel-arsenide structure type, X-ray diffraction

Introduction

The intermetallic compound MnBi received considerable attention since its favorable magneto-optical properties were recognized [1]. The high uniaxial magnetic anisotropy [2] at room temperature and the magneto-optical properties have attracted the interest of scientific community because of its possible applications in permanent magnets [3] and erasable magneto-optical memory devices [4]. The binary compound MnBi crystallizes into two phases: the lower-temperature hexagonal ferromagnetic phase (LTP) and the high temperature orthorhombic paramagnetic phase (HTP) with a structural phase transition at 628 K [5]. The electronic structure of MnBi indicates that the Mn atom possesses a magnetic moment of 3.6 μ_B, and that the Bi atom has a magnetic moment of −0.15 μ_B which is due to the s–d and p–d hybridization between Bi and Mn atoms [5]. Numerous attempts have been made for the purpose of obtaining single-phase MnBi, such as arc melting and rapid solidification methods [6,7], but formation of Mn precipitations and Bi matrix could not be avoided [8]. At present, no single-phase MnBi has been prepared. In order to oversee this impediment many efforts have been made to stabilize MnBi by varying its stoichiometry or by alloying it with a third element like Cu, Al, Nb, Si, etc., without any success [9, 10, 11].

[1] *Babes-Bolyai University, Faculty of Physics, 400084 Cluj-Napoca, Romania*
* E-mail: lrednic@phys.ubbcluj.ro
[2] *University of Osnabrück, Fachbereich Physik, 49069 Osnabrück, Germany*

On the other hand, the ferromagnetic compound MnSb has an electronic structure similar to MnBi and also crystallizes in two different structures: nickel-arsenide (NiAs) and zinc-blende (ZB). MnSb presents a $3d^{5.5}$ configuration on the Mn atom, with a magnetic moment of 3.5 μ_B on the Mn sites, and –0.06 μ_B on the Sb sites and a Curie temperature well above room temperature (T_c=587 K) [12]. Since both MnBi and MnSb have a hexagonal structure of NiAs type, it is possible that new ternary Mn-Bi-Sb system with an appropriate constitution is able to form a hexagonal structure too. The purpose of the present work is to obtain a new material with improved qualities by studying the structural and electronic changes induced by the substitution of Sb with Bi in $MnSb_{1-x}Bi_x$ (x=0, 0.2, 0.5, and x=0.95) system.

Experimental

Four samples belonging to $MnSb_{1-x}Bi_x$ (x= 0, 0.2, 0.5 and 0.95) system were prepared by argon arc melting method. In order to ensure homogeneity the samples were melted several times in the same atmosphere. The purity of the starting materials was 99.99% for Mn and Sb and 99.9% for Bi. The weight loss of the final samples was found out to be less than 1%. The quality of the samples was checked by conventional X-ray powder diffraction with Cu K_α radiation using a Bruker D8 Advance diffractometer.

The XPS spectra were recorded using a PHI 5600ci ESCA spectrometer with monochromatized Al K_α radiation at room temperature. The pressure in the ultra-high vacuum chamber was in the 10^{-10} mbar range during the measurements. In order to prevent surface contamination the samples were scratched in situ and the surface cleanness was checked by monitoring the O 1s and C 1s core levels in the survey spectra.

Results and discussions

The XRD patterns for the investigated samples are presented in Fig. 1, together with the corresponding theoretical spectra and theoretical pure Bi pattern. The PowderCell 2.3 [13] program was used for the evaluation of XRD patterns.

The alloys obtained by the substitution of Sb with Bi in MnSb have the same hexagonal crystallographic NiAs structure type phase ($MnSb_{1-x}Bi_x$) corresponding to the parent compound MnSb and also observed for MnBi. One can see the presence of some pure Bi peaks in all patterns corresponding to the investigated samples. The presence of these peaks is due to the segregation of Bi during the preparation process. The pure Bi phase is small comparing to $MnSb_{1-x}Bi_x$ phase, except for x=0.95 where it succeeds the nickel-arsenide structure type phase.

XPS core level and valence band spectra can provide important information regarding the electronic structure. To illustrate the quality of the samples in Fig. 2 is shown the survey spectrum of $MnSb_{0.5}Bi_{0.5}$ with the identification of the core levels and Auger lines.

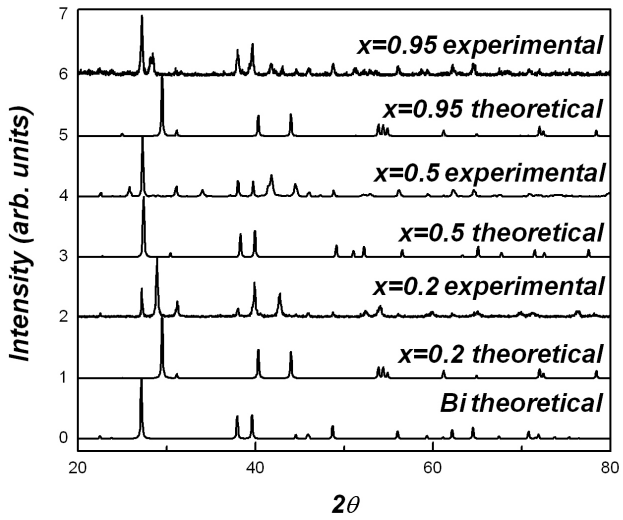

Fig. 1. Experimental and generated X-ray diffraction patterns of $MnSb_{1-x}Bi_x$ (x= 0, 0.2, 0.5 and 0.95) alloys and theoretical pure Bi spectra

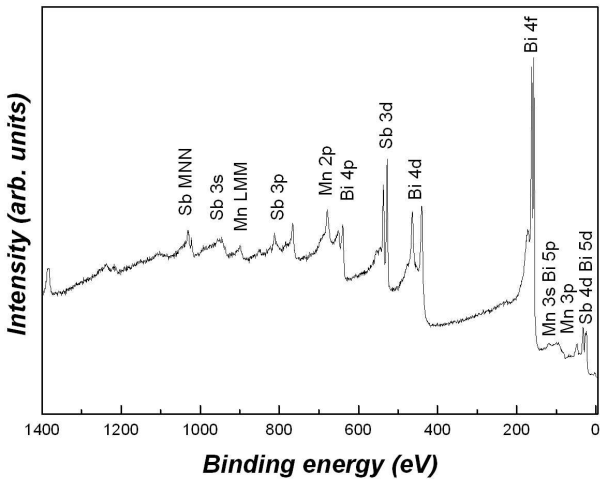

Fig. 2. XPS survey spectrum of $MnSb_{0.5}Bi_{0.5}$ alloy

One can observe that contamination is absent (the lack of C 1s and O 1s levels), thus the XPS spectra are representative of the bulk.

The valence band spectra of $MnSb_{1-x}Bi_x$ (x= 0, 0.2, 0.5 and 0.95) alloys are shown in Fig. 3.

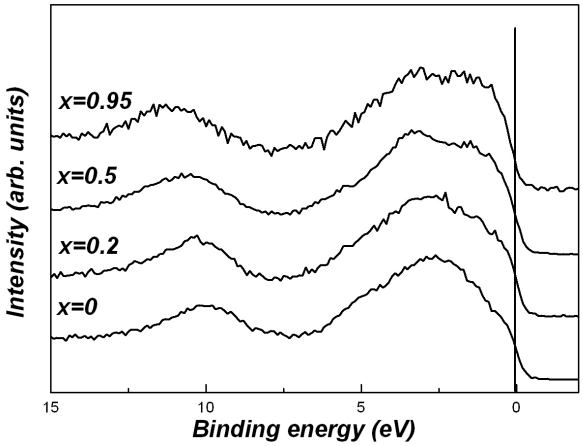

Fig. 3. XPS valence band spectra of $MnSb_{1-x}Bi_x$ (x= 0, 0.2, 0.5 and 0.95) alloys

Since the photoionization cross section of Mn, Bi and Sb are comparable; the valence band spectra of $MnSb_{1-x}Bi_x$ alloys are dominated by three main contributions: one given by Sb 5p, another one from Mn 3d and finally the Bi 6p. One can observe that the substitution of Sb with Bi in MnSb leads to the appearance of a new feature at higher binding energy, which is characteristic for the MnBi phase. The intensity of this feature increases with the increasement of Bi concentration. The spectral feature situated at about 10–11 eV is assigned to the Sb 5s and Bi 6s states [14]. The displacement of this feature is generated by the contribution brought by Bi 6s levels (10.5 eV).

A better understanding of the main characteristics in the valence band requires a comparison with the XPS valence band spectra of MnSb calculated with the Munich SPR-KKR package (Fig. 4).

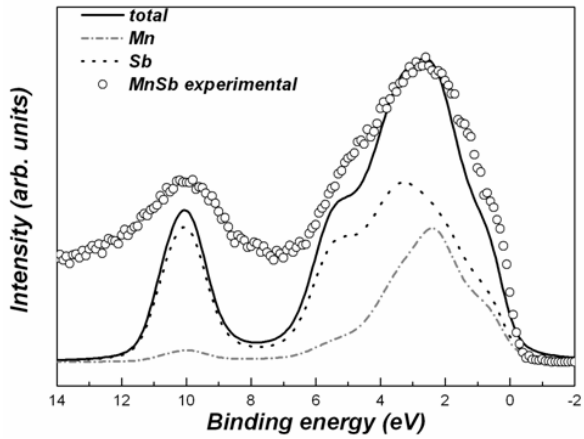

Fig. 4. Calculated (lines) and experimental (circles) XPS valence band spectra of MnSb

The computed XPS valence band spectrum of MnSb is in good agreement with the experimental results, indicating that the measured spectrum is representative of the bulk. Taking into account the similarities of the MnSb and MnBi electronic structures, one may suppose that the calculated XPS valence band spectrum of MnSb is also representative for the $MnSb_{1-x}Bi_x$ solid solutions.

Mn 2p XPS spectra of $MnSb_{1-x}Bi_x$ (x= 0, 0.2, 0.5 and 0.95) system (Fig. 5**)** present a spin–orbit splitting of ~11 eV, which can be identified in the distance between the centers of energy of the $2p_{3/2}$ and $2p_{1/2}$ states. The substitution of Sb by Bi in MnSb brings no significant changes in the Mn 2p band.

In case of atomic Mn, experimental and theoretical results revealed a fine structure of the 2p photoelectron spectrum caused by the Coulomb interactions of the 2p hole and 3d valence electrons [15]. Fig. 6 shows the fitting of Mn $2p_{3/2}$ XPS spectra for the investigated alloys. The fitting results were obtained considering four components and a satellite line. The full width at half maximum (HWHM) of each multiplet peak was considered between 1 eV and 1.5 eV, with a 0.4eV Lorentian contribution (accounting the Mn 2p hole states lifetime [16]) and a 0.6-0.8 eV Gaussian contribution (accounting for the instrumental broadering). The relative intensities of these states vary depending on the Mn atomic environment, reflecting the changes induced to the properties of Mn 3d states.

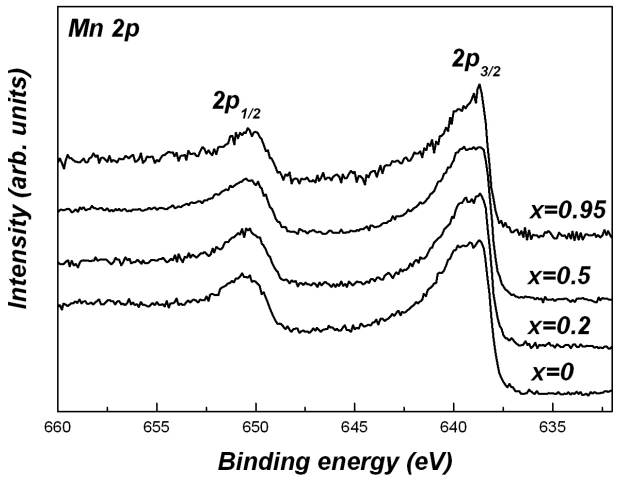

Fig. 5. XPS Mn 2p core level spectra of $MnSb_{1-x}Bi_x$ (x= 0, 0.2, 0.5 and 0.95) alloys

The binding energies of the fitted multiplet splitting components and the mean energy separation between the four components, which corresponds to the exchange splitting of the Mn 2p core-hole states, are listed in Table 1.

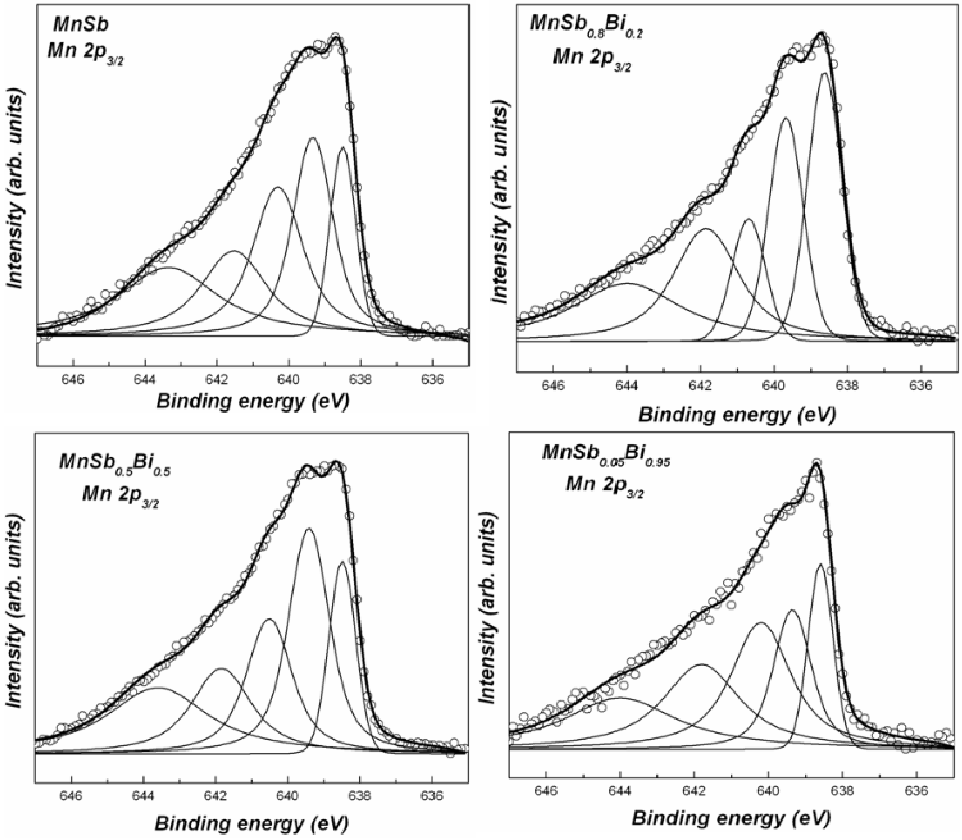

Fig. 6. Curve fitting results (solid lines) of Mn $2p_{3/2}$ core level spectra of $MnSb_{1-x}Bi_x$ (x= 0, 0.2, 0.5 and 0.95) alloys superposed on the measured spectra (circles)

Table 1.

Fitting parameters for Mn $2p_{3/2}$ XPS spectra of $MnSb_{1-x}Bi_x$ (x= 0, 0.2, 0.5 and 0.95) alloys. Δ_{ex} denotes the mean exchange splitting between the sublevels

x	Binding energy (eV)				
	Component 1	Component 2	Component 3	Component 4	Δ_{ex} (eV)
0	638.5	639.3	640.3	641.5	1.01
0.2	638.6	639.6	640.7	641.8	1.07
0.5	638.4	639.4	640.5	641.8	1.12
0.95	638.6	639.3	640.1	641.7	1.06

The mean energy separation between the four components has a value between 1.01 eV and 1.12 eV in the investigated samples. These values confirm the formation of $MnSb_{1-x}Bi_x$ solid solution by the substitution of Sb with Bi in MnSb compound. Since the exchange splitting Δ_{ex} is approximately the same in all alloys one may suppose that the Mn 3d states in $MnSb_{1-x}Bi_x$ are not affected by alloying.

The Sb 3d XPS core level spectra of $MnSb_{1-x}Bi_x$ (x= 0, 0.2, and 0.5) system are shown in Fig. 7.

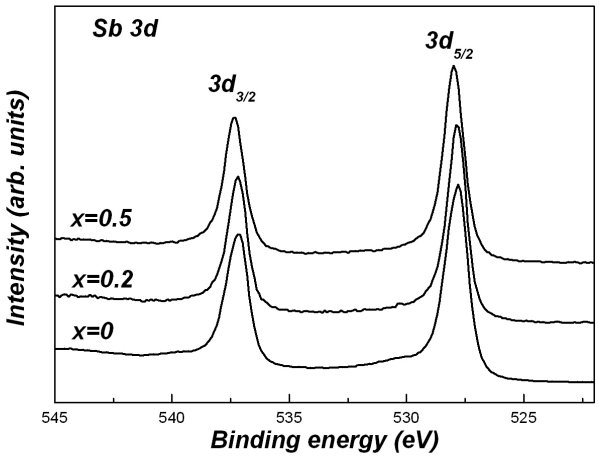

Fig. 6. XPS Sb 3d core level spectra of $MnSb_{1-x}Bi_x$ (x= 0, 0.2 and 0.5) alloys

The lack of O 1s at 531eV binding energy in the Sb 3d core level spectra indicates that contamination is absent and proves the good quality of the investigated sample. The small chemical shifts observed in the Sb 3d core level spectra of $MnSb_{1-x}Bi_x$ may be explained by the changed induced in the Sb atoms vicinity.

Conclusions

Until now no single-phase MnBi has been prepared. In order to oversee this impediment we have tried to stabilize MnBi phase by alloying it with Sb. The substitution of Sb by Bi in MnSb leads to the formation of new and improved compounds which preserve the same crystallographic structure as the parent compound. The X-ray diffraction measurements indicate the formation of $MnSb_{1-x}Bi_x$ solid solution. For higher Bi concentration (x=0.95) one can observe that a mixture of pure metallic Bi and $MnSb_{1-x}Bi_x$ phase appears. The presence of unreacted Bi is due to the segregation during the preparation process. XPS valence band, Mn 2p and Sb 3d core level spectra have confirmed the formation of $MnSb_{1-x}Bi_x$ solid solution. The

computed XPS valence band spectrum of MnSb is in good agreement with the experimental results, indicating that the measured spectrum is representative of the bulk. The Mn $2p_{3/2}$ core levels exhibit a multiplet structure arising from the exchange interactions between the core hole and the open 3d shell. The Mn 3d states in $MnSb_{1-x}Bi_x$ do not change appreciable by alloying.

REFERENCES

[1] H. J. Williams, R. C. Sherwood, F. G. Foster, and E. M. Kelley, *J. Appl. Phys.* **28**, 1181(**1957**)

[2] C. Guillard, *J. Phys Radium* **12**, 143 (**1951**)

[3] J. B. Yang, K. Kamaraju, W.B. Yelon, W. J. James, *Appl. Phys. Lett.* **79**, 1846 (**2001**)

[4] P.M. Oppeneer, V.N. Antonov, T. Kraft, H. Eschrig, A.N. Yaresko, A.Ya. Perlov, *J. Appl. Phys.* **80**, 1099. (**1996**)

[5] R. Coehoorn and R. A. De Groot, *J. Phys. F: Met. Phys.* **15**, 2135 (**1985**)

[6] H. Yoshida, T. Shima, T. Takahashi, H. Fujimori, *Mater. Trans. JIM* **40**, 455 (**1999**)

[7] X. Guo, Z. Altounian, J.O. Stom-Olsen, *J. Appl. Phys.* **69**, 6067 (**1991**).

[8] S. Saha, M.Q. Huang, C.J. Thong, B.J. Zande, V.K. Chandhok, S. Simizu, R.T. Obermyer, S.G. Sankar, *J. Appl. Phys.* **87**, 6040 (**2000**)

[9] Y. J. Wang, *J. Magn. Magn. Mater*. **84**, 39 (**1990**)

[10] P. Bandaru, T. D. Sands, Y. Kubota, and E. E. Marinero, *Appl. Phys. Lett.* **72**, 1 (**1998**)

[11] R. F. Sabiryanov and S. S. Jaswal, *J. Appl. Phys.* **85**, 8 (**1999**)

[12] R. Coehoorn, C. Haas and R.A. de Groot, *Phys. Rev. B* **31,** 1980 (**1990**).

[13] G. Nolze and W. Kraus, *PowderCell 2.3 Program*, BAM Berlin (**2000**)

[14] A. Kimura, S. Suga, T. Matsushita, H. Daimon, T. Kaneko, T. Kanomata, *J. Phys. Soc. Jpn.* **62**, 1624 (**1993**).

[15] Ph. Wernet, B. Sonntag, M. Martins, P. Glatzel, B. Obst and P. Zimmermann, *Phys. Rev. A* **63**, 050702(R) (**2001**)

[16] M.O. Krause and J. H. Oliver, *J. Phys. Chem.* Ref. Data **8**, 329(**1979**)

STUDIA UNIVERSITATIS BABEŞ-BOLYAI, PHYSICA, LIII, 2, 2008

^{13}C CPMAS NMR STUDY OF CHLORTHALIDONE AND FUROSEMIDE INCLUSION IN B-CYCLODEXTRINS

BOGDAN FRENȚIU[1], CODRUȚA ȘOICA[2], CRISTINA DEHELEAN[2], ÁRPÁD GYÉRSESI[3], MIHAELA ALUAȘ[1], SIMION SIMON[1]

ABSTRACT. The nuclear magnetic resonance (NMR) spectroscopy on solids using cross-polarization magic angle spinning experiment have been used to study insertion of drugs chlorthalidone in hydroxypropyl-β-cyclodextrin (HPBCD) and furosemide in randomly methylated β-cyclodextrin (RAMEB) to see if exist any interaction between substances in each case, and if they will shape inclusion complexes. Both drugs are practically in water insoluble diuretic, used for the treatment of edema and hypertension. The preparations have been done in 1:1 and 1:2 molar ratios using specifically methods like kneading product and ultrasonication.

The study demonstrate that HPBCD and RAMEB are able to include in their cavities chlorthalidone and furosemide respectively, follow by formation of inclusion complexes with a high bioavailability, offering possibility to produce new improved pharmaceutical products.

Key-words: NMR spectroscopy, furosemide, chlorthalidone, RAMEB, HPBCD

Introduction

The nuclear magnetic resonance (NMR) spectroscopy is one of most used methods to investigate and characterize different solid samples, and using cross-polarization magic angle spinning experiment can be obtained improved signals for nuclei which have low gyromagnetic ratio or poorly natural abundance like ^{13}C nuclei. The method was used by us to investigate insertion of chlorthalidone in hydroxypropyl-β-cyclodextrin (HPBCD) and furosemide in randomly methylated β-cyclodextrin (RAMEB) respectively, to see if exist any interaction between substances in each case, and if they will shape inclusion complexes.

Chlorthalidone (2-chloro-5[(1RS)-1-hydroxy-oxo-2, 3-dihydro-1H-isoinodol-1-yl]) and furosemide (4-chloro-2[(furan-2-ylmethyl) amino]-5-sulphamoylbenzoic acid) are practically in water insoluble diuretic, used for the treatment of edema and hypertension [1]; they are yellowish-white powders, soluble in ethanol, methanol and acetone and photosensitive. The drugs present a poor bioavailability because they have a low solubility in water. This aspect can be improved if we will obtain inclusion

[1] *Faculty of Physics, „Babeş-Bolyai" University, Cluj-Napoca, Romania*
[2] *Faculty of Pharmacy, University of Medicine and Pharmacy „Victor Babeş" Timişoara, Romania*
[3] *Faculty of Pharmacy, University of Medicine and Pharmacy Târgu-Mureş, Romania*

complexes between chlorthalidone and HPBCD, and furosemide and RAMEB respectively, that means we optimized the solubility and chemical-physical stability, which leads to higher bioavailability [2].

Cyclodextrins are torus-shaped oligosaccharides, which contain a number of glucose monomers ranging from 6 to 13 units in a ring, built up from α-1,4-D-glucopyranose units, creating a cone shape. The principals and most synthesized and analyzed cyclodextrins are that which contains 6 sugar ring units (α-cyclodextrin), 7 sugar ring units (β-cyclodextrin), 8 sugar ring units (γ-cyclodextrin) (fig.1) [3].

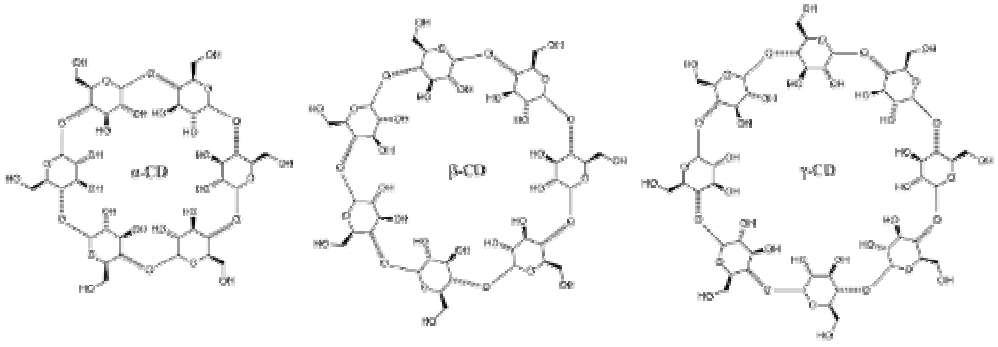

Fig. 1. The principal cyclodextrins

The theoretical calculations of conformational energy demonstrate that can not create rings with less than six units, because of existing stearic barrier [3, 4]. The cyclodextrins can be obtained using an approachable technology like fermentation of starch reaction. They have truncated cone shape and posed a hydrophobic cavity with size of 6-10 Å, which is able to host hydrophobic organics molecules. Most suitable cyclodextrin for insertion is β-cyclodextrin; this is actually most facile and used among cyclodextrins can be able to form inclusion complexes with 1:1 molar ratio.

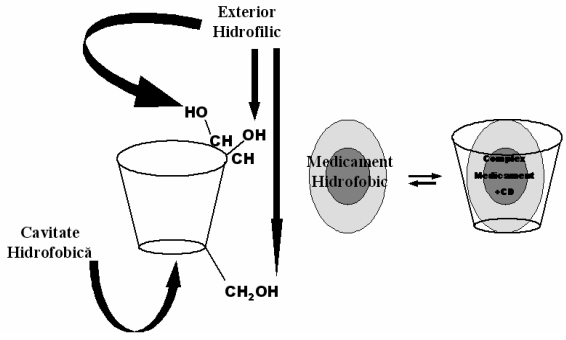

Fig. 2. Schematically process of drug insertion in β-cyclodextrin.

When a substance less soluble in water interacts with a cyclodextrin, the hydrophobic part of that substance is totally or partial include in cyclodextrin cavity and in same time it will form inclusion complex. At genesis of inclusion complexes, the forces which permit the isolation of complex in solid state and in the same time, the discharge of active substance in special condition, are Van der Waals forces, hydrogen links and dipole-dipole interactions [2, 6].

The aim of this study is to investigate insertion of chlorthalidone and furosemide in cyclodextrins using solid state nuclear magnetic resonance spectroscopy, and to confirm the results which have been obtained on insertion of chlorthalidone in HPBCD and insertion of furosemide in RAMEB, using the others investigation methods like differential scanning calorimetry (DSC), X-ray diffraction (XRD), in vitro dissolution tests. The results obtained with these methods have been demonstrated that there is an interaction between used drugs and cyclodextrins, and leads to form inclusion complexes.

During the afore-mentioned measurements, was observe for each case which is the most applicable preparation method and which is the better molar ratio to prepare inclusion complexes of both drugs. Such as for furosemide, the better method to prepare inclusion complex is ultrasonication in 1:1 and 1:2 molar ratio; and for chlorthalidone is kneading product method in 1:2 molar ratio [2].

Methods and materials

Chlorthalidone and furosemide was received as a gift sample from SC Terapia SA (Cluj-Napoca); Cyclodextrins RAMEB and HPBCD (fig.3 a&b) were purchased from Cyclolab R&D Ltd. (Budapest, Hungary).

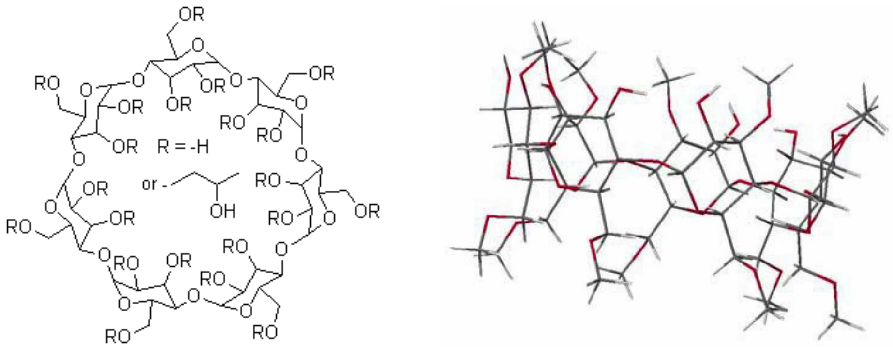

a b

Fig. 3. Chemical structure of HPBCD (a) and RAMEB (b)

Chlorthalidone and HPBCD was prepared using kneading product method obtained an inclusion complex between this substances in 1:2 molar ratio: the physical mixtures were kneaded with 50% ethanol solution until the bulk of solvent

evaporated and then dried at room temperature for 24 hours and then was put in the oven at 105ºC by the constant mass. The sample was pulverized in mortar and after that passed through sieve no V [5].

The inclusion complex of furosemide and RAMEB was prepared using ultrasonication method: the physical mixtures were dissolved in 50% ethanol, placed in the ultrasonic apparatus Dataphysics OCA 20 (Dataphysics, Germany) for 1 hour, dried in oven at 105ºC and after that pulverized in mortar and passed through sieve no V [5].

The solid state ^{13}C NMR spectra were recorded at 100 MHz ^{13}C Larmor frequency with a Bruker Avance-400 spectrometer. All NMR experiments were performed at room temperature and the sample was centred-packed in zirconium rotors to minimize the effect of rf field inhomogeneity. Standard cross-polarization magic angle spinning (CP/MAS) (fig.4) [7, 8] experiments were performed at a spinning frequency ν_R=8 kHz, using a ^1H 90° pulse length of 3.6 μs.

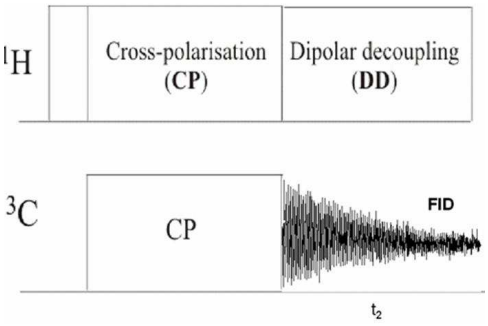

Fig. 4. Pulse sequence of CPMAS NMR experiment

The ^{13}C NMR spectra were acquired under two-pulse phase-modulated (TTPM) ^1H decoupling at 70 kHz by averaging 512 scans with a recycle delay of 3 s. The CP transfer was optimized for the first Hartmann-Hahn matching condition ($\nu_{1C}= \nu_{1H}=\nu_R$), were the rf fields on the 1H and 13C channels have been calibrated to 42 and 50 kHz, respectively and the CP contact time was set to 1 ms for all the experiments. Chemical shift of ^{13}C nuclei are expressed in parts per million (ppm) and calibrated with respect to tetramethylsilane (TMS) as described in literature [9].

Results and discussion

The ^{13}C NMR spectra were recorded for two sets of sample and for each sample in case:

1) Chlorthalidone (CLT), hydroxypropyl-β-cyclodextrin (HPBCD) and inclusion complex of CLT with HPBCD (fig.5);
2) Furosemide (FS), randomly methylated β-cyclodextrin (RAMEB) and inclusion complex of FS with RAMEB (fig.7).

In the table I we can see the chemical shifts (δ) peaks of ^{13}C CP/MAS NMR spectra of chlorthalidone, hydroxypropyl-β-cyclodextrin and inclusion complex of CLT with HPBCD.

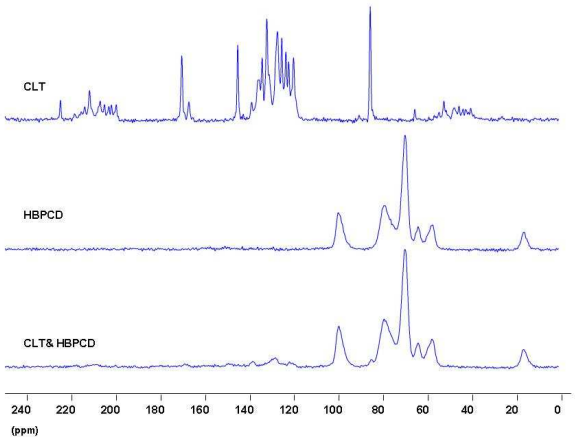

Fig. 5. The CPMAS ^{13}C NMR spectrum of CLT, HPBCD, HPBCD&CLT

Table I.

No. peak	CLT (ppm)	HPBCD (ppm)	CLT+HPBCD (ppm)
1		17.2	18.1
2	53.4		
3		58.1	58.9
4		64.6	65.1
5		70.3	70.9
6		79.3	80.3
7	86.4		85.5
8		99.7	100.5
9	120.9		
10	123.1		122.7
11	124.3		
12	126.2		
13	128.2		129
14	132.9		
15	135		
16	136.7		
17			139.1
18	145.9		
19	171.1		
20	212.5		

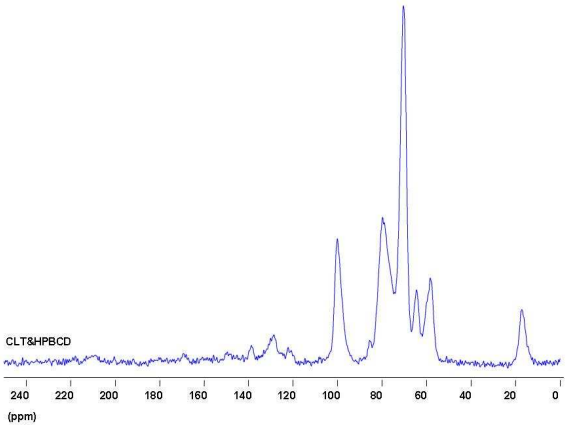

Fig. 6. The CPMAS ^{13}C NMR spectrum of CLT&HPBCD

After the insertion of chlorthalidone into the cavity of HPBCD, we can observe the appearance of four new peaks of low intensity at 85.5 ppm, 122.7 ppm, 129 ppm and 139.1 ppm (fig.6) and the others characteristic peaks of HPBCD have a short shift (0.6-1 ppm). The shifting down-filed of the cyclodextrin peaks in the spectrum of the complex and the appearance of the new peaks which are not characteristic to the host molecule prove there has been an interaction between the two substances probably with the formation of an inclusion complex.

In the table II we can see peaks of ^{13}C CP/MAS NMR spectra of furosemide, randomly methylated β-cyclodextrin (RAMEB) and inclusion complex of FS with RAMEB.

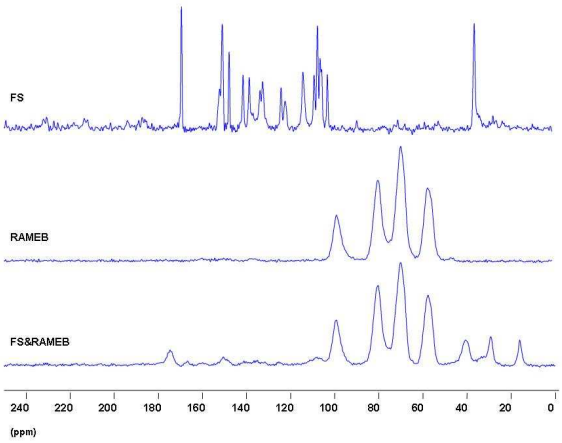

Fig. 7. The CPMAS ^{13}C NMR spectrum of FS, RAMEB, FS&RAMEB

Table II.

No. peak	FS (ppm)	RAMEB (ppm)	FS+RAMEB (ppm)
1			16.4
2			29.6
3	36.8		
4			41
5		57.3	58
6		69.5	70.3
7		79.7	80.5
8		98.6	99.4
9	103.5		
10	106.7		
11	108		108.3
12	109.5		
13	114.5		
14	122.6		
15	124.5		
16	132.8		
17	138.9		
18	141.7		
19	148.1		
20	151.2		150.6
21	169.7		166.8
22			174.2

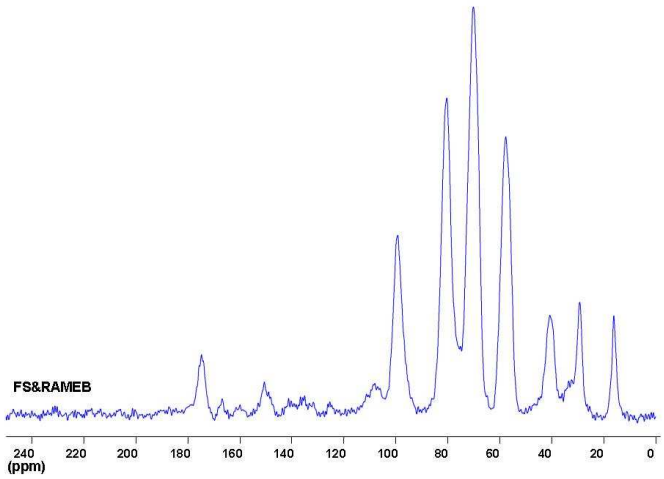

Fig. 8. The CPMAS ^{13}C NMR spectrum of FS&RAMEB (FS-US)

After the insertion of furosemide into cavity of RAMEB we can observe the appearance of five new peaks at 16.4 ppm; 29.6 ppm; 41 ppm; 150.6 ppm and 174.2 ppm (fig.8); and the others peaks which are characteristic for RAMEB are shifted ~ 0.8 ppm.

The appearance of the new five peaks which are not characteristic for the guest molecule as well as the shift down field of the cyclodextrin peaks proves there has been a quite strong interaction between the drug and cyclodextrin suggesting the formation of an inclusion complex. These results are in good correlation with information obtained by methods like differential scanning calorimetry (DSC), X-ray diffraction (XRD), in vitro dissolution tests [2].

Conclusions

The results by ^{13}C CP/MAS NMR spectroscopy confirm the results of complex analyzes which have been obtained using X-ray diffraction (XRD), differential scanning calorimetry (DSC) and in vitro dissolution tests, attesting that experimental method by itself it is adequate for suchlike of studies and it exist an interaction between chlorthalidone and HPBCD and furosemide and RAMEB respectively, both with really chance to form inclusion complexes.

The information obtained by NMR spectroscopy correlated with results of complementary experiments (XRD, DSC) demonstrate in case of chlorthalidone and HPBCD the most adequate method is kneading product in 1:2 molar ratio, while for furosemide and RAMEB the most efficient method is ultrasonication in 1:1 and 1:2 molar ratio to obtain inclusion complexes.

The presence of HPBCD and RAMEB for each drug strongly influences different parameters of chlorthalidone and furosemide: solubility, dissolution, leading to the possibility of obtaining new pharmaceutical preparation, with a greater bioavailability.

Acknowledgments

The authors would like to thank for the financial support from the Romanian Ministry of Educational and Research (CNCSIS nr.63 AT_ALUAS şi CNCSIS nr.173 AT_DEHELEAN).

REFERENCES

1. C.T. Dollery, Therapeutic Drugs, Churchill Livingstone, New York, 221, 1999
2. C. Şoica, Á. Gyérsesi, M. Kata, C. Dehlean, Revista de Chimie, 57, 4, (2006)
3. J. Szejtli: Chem. Rev., 98, 1743 (1998).

4. C. Morari, D. Bogdan, M. Bogdan, Rom. Journ. Phys., Vol. 50, (9–10), 995 (2005)
5. ******* Farmacopeea Română, ed. a X-a, Ed. Medicală, Bucureşti, 1993
6. M.E. Davis, M.E. Brewster, Drug discovery, 3, 1023, (2004)
7. A Pines, M. G. Gibby, J. S.Waugh, *Chem. Phys.*, 59, 569, (1973**)**
8. Andrew, E. R.; Bradbury, A.; Eades, R.G., *Nature,*182, 1659, **(**1958**)**
9. R.K. Harris, in *Encyclopedia of Nuclear Magnetic Resonance*, D.M. Granty and R.K. Harris (eds.), vol.5, John Wiley & Sons, Chichester,1996.

STUDIA UNIVERSITATIS BABEŞ-BOLYAI, PHYSICA, LIII, 2, 2008

INFRARED SPECTROSCOPY OF SMALL WATER CLUSTERS

TITUS A. BEU[*] AND GABRIEL CĂBĂU

ABSTRACT. We report calculated infrared spectra for water clusters composed of up to twenty molecules, using a formalism based on second order perturbation theory. We have investigated the frequency domain between 3000 and 4000 cm^{-1}, which includes the two stretching modes and the first overtone of the angle bending mode. The stretching modes are found to be red shifted, while the bending mode is blue shifted. For both modes the line shifts increase with the cluster size and appear to be strongly correlated with the average number of hydrogen bonds per cluster. The spectral lines corresponding to the stretching of free OH bonds (not participating in hydrogen bonds) have been found to be almost independent on the cluster sizes. For larger clusters the spectra tend to form broad bands which can be identified in the experimental spectra of bulk water.

Keywords: molecular clusters, vibrational spectra, water.

1. Introduction

Water is one of the most intensively studied substances, due to its special properties, the presence of hydrogen bonds being responsible for many of them. A water molecule can form four hydrogen bonds: two of them involving the oxygen atom and the other two, the hydrogen atoms, acting as donors.

One of the most sensitive methods of probing the hydrogen bond network is vibrational spectroscopy. The presence of the hydrogen bonds causes the spectral lines of the monomer to be either red shifted (the stretching modes) or blue shifted (the bending mode). We have investigated the frequency domain between 3000 and 4000 cm^{-1}, containing beside the symmetric and asymmetric stretch modes also the first overtone of the angle bending mode (all three modes being non-degenerate). There are only few experimental studies of water cluster spectra in this frequency range, among which the most accurate are those published by Buck et al. [1]-[4] and Huisken et al. [5]. Other experiments were carried out using less effective size-selection techniques. For example, Huang and Miller [6] have measured spectra only for the dimer, while Cocker et al. [7] have reported spectra for larger clusters, however without any size selection.

2. Theoretical methods

Our investigations comprise two main areas: calculations of the geometrical equilibrium structures of the clusters (using a compound deterministic-stochastic strategy) and quantum mechanical calculations of the infrared spectra employing a well tested formalism based on second order perturbation theory [8],[9].

One of the goals of the present study was also to distinguish the relevance of molecular polarization in simulations of water clusters, and consequently we have comparatively studied a potential model implying a fully rigid monomer, TIP4P [10], and a model featuring along with the fixed sites also one movable polarization site, COS/B2 [11].

The TIP4P model consists of four fixed sites: three corresponding to real atoms and one supplementary site that is positioned on the bond angle bisector. The supplementary site carries the electric charge corresponding to the lone-pair electrons, while the sites corresponding to the actual O atoms interact with each other only through a Lennard-Jones potential.

In the COS/B2 model, electrostatic interactions operate between all sites of different molecules and, again, the O atoms feature supplementary Lennard-Jones interactions. The molecular polarization is accounted for by an additional pair of opposite charges, placed on the O atom and on an additional movable site, respectively. The equilibrium separation between the two charges results in response to the instantaneous electric field acting on the O atom.

The formalism for the frequency shifts of molecular clusters [8] is based on the idea of treating the anharmonic contributions to the intramolecular force field and the intermolecular potential as a perturbation of the uncoupled harmonic vibrations of the monomers, described in the normal mode approach. This formalism was successfully applied to several systems, including ammonia clusters up to N=100 [13].

Since the method used in this study is well tested and we have used it successfully in several other studies [9], in order to get more realistic results, we have adjusted a few of the cubic force constants $\Phi_{m'm''r}$. These originally stem from the anharmonic normal mode analysis of the monomer vibrations performed according to the L-tensor method of Hoy et al. [16], but they are known to be rather susceptible to the transformation process from valence to normal coordinates. From the total of ten most significant cubic force constants, three have been adjusted. For example, the Φ_{111} constant was increased by a factor of 1.5.

Another aspect worth mentioning is that the line spectra obtained for the isomers of a given size was averaged over the whole ensemble of the lowest 500 configurations, assuming a Boltzmann-type distribution of the isomers with respect to the binding energy and an equilibrium temperature of 150 K, which is consistent with typical experimental conditions [3].

3. Results and discussion

The equilibrium structures of the water clusters (N=2-20) have been determined by stochastic minimization of the total interaction energy. Specifically, the energy minima have been determined by optimizing the center of mass positions and orientations of the molecules, starting from random initial configurations. Several hundreds of thousands (up to millions) of minimizations have been necessary to obtain the global minimum for each cluster size and, with a view to calculating average IR-spectra, we have considered the lowest 500 configurations.

The energies obtained for the equilibrium structures with both potential models agree with those published by Wales et al. [17]. Even though for small clusters, the energies obtained with the TIP4P model are slightly lower than those obtained with the COS/B2 model, the structures optimized with the latter showing generally higher symmetry. As an example, Figure 1 shows comparatively the structures of the lowest energy hexamer isomers obtained with the two potentials. As can be easily noticed, the COS/B2 equilibrium structure shows higher symmetry, even though the corresponding binding energy (-197.22 kJ/mol) is a bit higher than the TIP4P value (-197.78 kJ/mol).

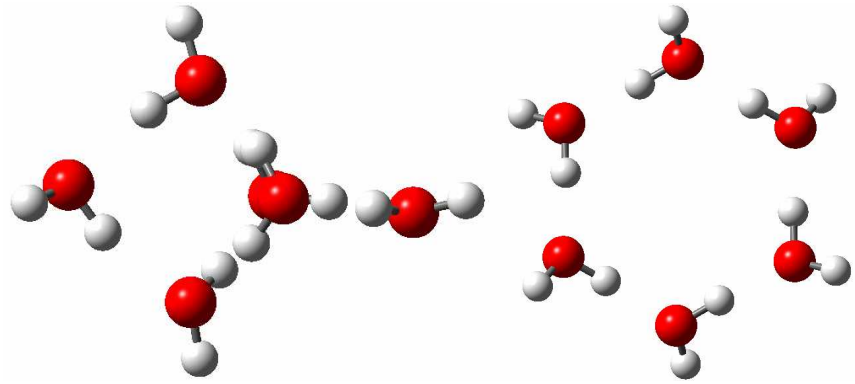

Figure 1. Geometric structures of the lowest energy hexamer isomer obtained with the non-polarizable potential TIP5P (left panel) and the polarizable COS/B2 potential (right panel).

For clusters composed of up to five molecules, the spectra obtained with the two potentials are comparable. However, when going to larger cluster sizes, the difference between them becomes more significant. Even with adjusted cubic force constants, for clusters larger than the pentamer the TIP4P model produces unrealistic spectra, while the spectra computed with the COS/B2 model follow fairly the experimental ones. It appears that the lack of polarizability renders the TIP4P model ineffective for IR spectroscopy studies. Therefore we will discuss further on only results obtained with the COS/B2 potential model.

The frequency shifts obtained for the asymmetric stretch mode ν_3 are the smallest ones and this can be explained by the fact that the vibrations of the free OH bonds, which are not involved in hydrogen bonds but which are mainly involved in this mode, are almost independent of the number of hydrogen bonds and of the cluster size. The symmetric stretch lines (ν_1) are less intense than the asymmetric stretch lines because of the hydrogen bonds being hindered by the intermolecular force field, but the ν_1 lines show a larger shift, proving a strong dependence of the number of hydrogen bonds. As expected, the intensity of the overtone of the bending mode ($2\nu_2$) lines is about for times smaller than that of the stretch lines. This result, too, comes to confirm the appropriateness of our perturbative approach.

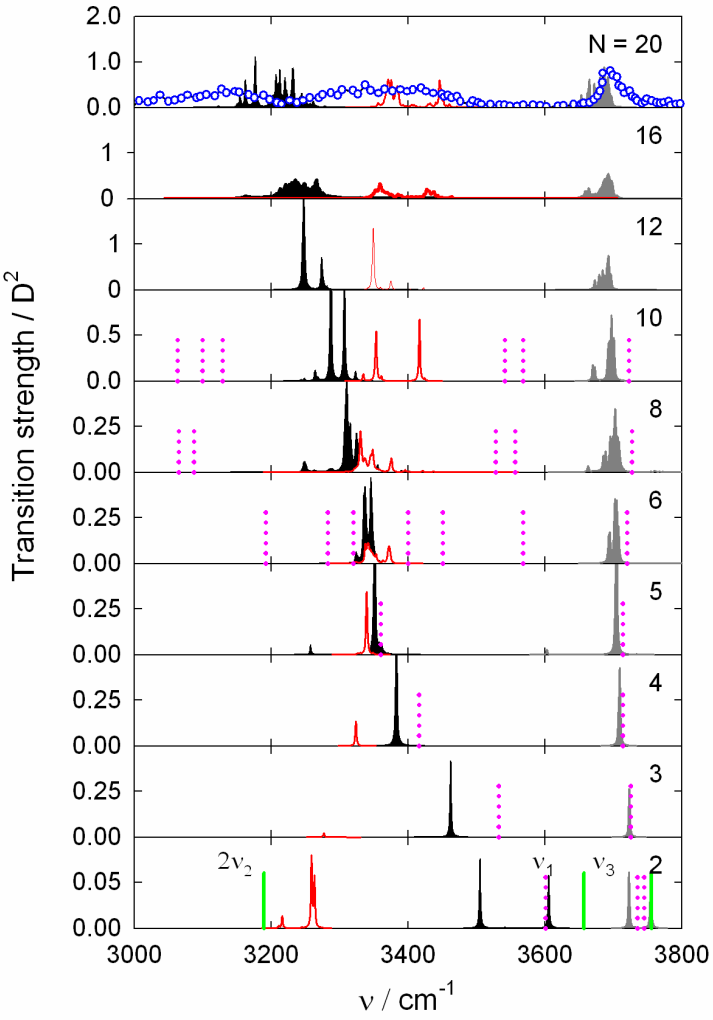

Figure 2. IR spectra for $(H_2O)_N$ clusters. The solid drop-lines in the lowest panel (N=2) represent the monomer frequencies, while the dotted drop lines are the experimental frequencies of Huisken et al. [5]. The intensity of lines corresponding to the bending mode, $2\nu_2$, was increased by a factor of 4. The data for liquid water reported by Buck et al. [3] was depicted in the upper most panel (N=20).

Our infrared spectra are compared with the experimental results for size-selected water clusters obtained by Huisken et al. (N=2-5) [5] and Buck et al. (N = 6-10) [1]-[4]. For clusters larger than the decamer there is no accurate size-selective study in literature. For dimer and trimer our results are in good agreement with the experiments. From trimer to pentamer the experimental lines assigned to

the asymmetric stretch mode are less redshifted than the values predicted by our calculations while from the octamer the tendency is inverse, arriving to the comparable shift for clusters around N = 20.

There is an obvious tendency of the clusters lines to reach the central positions of the three main bands present in the experimental liquid phase spectrum [3].

4. Conclusions

We have computed structures and infrared line shifts for water clusters formed of up to 20 molecules, investigating two model potentials (TIP4P and COS/B2) and several prescriptions for the motions of the supplementary interaction sites as part of the molecular vibrations. The best results were obtained with the polarizable COS/B2 model, the TIP4P model rendering unrealistic spectra due to its rigidity and the lack of polarizability. The line shifts appear to be strongly dependent on the number of hydrogen bonds in the clusters. The most significant shifts appear for the symmetric stretch mode ν_1, while the asymmetric stretch mode ν_3 remains almost unshifted with increasing cluster size, being less affected by the intermolecular force field. The lines corresponding to the overtone of the bending mode are much less intense. The line shifts increase with cluster size, but for larger clusters they tend to saturate, reproducing in the investigated frequency range the three distinct bands found in the experimental liquid-state spectra.

Acknowledgments

The authors acknowledge the CNCSIS grant 1310/2006 from the Romanian Ministry of Education and Research.

REFERENCES

[1] U. Buck, I. Ettischer, M.Melzer, V. Buch and J. Sadlej, Phys. Rev. Lett. **80**, 2578 (1998).
[2] J. Brudermann, M. Melzer, U. Buck, J. Kazimirski, U. Buck, J. Chem. Phys, **110**, 10649 (1999).
[3] U. Buck, F. Husiken, Chem. Rev. **100**, 3863 (2004).
[4] C. Steinbach, P. Andresson, M. Melzer, J.K. Kazimirski, U. Buck, V. Buch, Phys. Chem. Chem. Phys. **6**, 3320 (2004).
[5] F. Huisken, M. Kaloudis, A. Kulcke, J. Chem. Phys. **104**, 1 (1996).
[6] Z.S. Huang, R. E. Miller, J. Chem. Phys. **91**, 6613 (1989).
[7] D. F. Cocker, R. E. Miller, R.O. Watts, J. Chem. Phys. **82**, 3554 (1985).
[8] T.Beu , Z.Phys: At., Mol. Clusters **31**, 95 (1995).
[9] T. A. Beu and K. Takeuchi, J. Chem. Phys. **103**,6394(1995).
[10] M.W. Mahoney and W.L. Jorgensen, J. Chem. Phys. **112**, 20 (2000).

[11] Habio Yu, T. Hansson and W. F. Gunsteren J. Chem. Phys. **118**, 221 (2003).
[12] U. Buck and B. Schmidt, J. Chem. Phys. **98**, 9410 (1993).
[13] T. A. Beu and U. Buck, J. Chem. Phys. **114**, 7853 (2001).
[14] T. A. Beu and U. Buck, J. Chem. Phys. **114**, 7848 (2001).
[15] E. B. Wilson, J. C. Decius, and P.C. Cross, Molecular Vibrations (McGraw-Hill, New York, 1955).
[16] A.R. Hoy, I. M. Mills, and G. Strey, Mol. Phys. **24**, 1965, (1972).
[17] D. J. Wales and M. P. Hodges, Chem. Phys. Lett. **286**, 65 (1998).
[18] T. James, D.V. Wales, J. Hernandez-Rojas, Chem. Phys. Lett. **415**, 302 (2005).
[19] Xantheas, T.H. Dunning, J. Chem. Phys. **99**, 8774 (1993).

STUDIA UNIVERSITATIS BABEŞ-BOLYAI, PHYSICA, LIII, 2, 2008

SUPPORTED NICKEL CATALYSTS INVESTIGATED BY TEMPERATURE PROGRAMMED REDUCTION METHOD

STELIAN PINTEA[a,b]*, PETRU MĂRGINEAN[a], ŞTEFAN GERGELY[a], VASILE REDNIC[a,b], NICOLAE ALDEA[a]

ABSTRACT. A method for obtaining supported nickel catalysts is a chemical one that involves four steps described in the following pages. Reduction is one of these steps and it can be analyzed by temperature programmed reduction technique. In this paper we investigate the reduction behavior of the NiO in different cases. For data acquisition we used a home-made setup also described in the paper. The temperature for reduction of NiO depends on the presence and the chemical nature of the support. The first case discussed is that of the pure NiO reduction as a function of temperature. The present paper also describes the reduction of NiO in the presence of Al_2O_3, Cr_2O_3 and MgO as supports. Different values for the temperatures corresponding to the maximum hydrogen consumption during the reduction of NiO are discussed.

Keywords: supported nickel catalysts, TPR, NiO reduction, active metal – oxide support interaction

Introduction

Temperature programmed reduction (TPR) is a technique that describes the reduction behavior of different oxides as a function of temperature [1, 2].

The applications of the catalysts make them very useful in industrial activities like: production of ammonia, sulfuric acid and petroleum reforming. If we are speaking about nickel catalysts, we have to mention its applications in the field of isotopic exchange reactions and hydrogenation of the CO [3]. The catalysts act by decreasing the activation energy of the reaction, selecting one from many ways that reaction can occur, making possible some reactions that cannot take place without catalysts. So, we can see that these materials are very important and they are very helpful in environmental protection and for saving energy in the industrial processes.

[a] *National Institute for R&D of Isotopic and Molecular Technologies, 400293 Cluj – Napoca, Romania*
[b] *Faculty of Physics, Babeş-Bolyai University, 400084 Cluj – Napoca, Romania*
* Corresponding author. Tel.: +40 264 584037; fax: +40 264 420042
E-mail address: Stelian.Pintea@itim-cj.ro (S.Pintea)

Preparation method of the supported nickel catalysts

Supported nickel catalysts were obtained using the coprecipitation method that involves four important steps: coprecipitation, calcination, reduction and passivation.

Coprecipitation is used for the mixing of the components, the metal with the supports. For preparing Ni/Al_2O_3, the solution of the mixture of nickel nitrate and aluminium nitrate, in the expected Ni/Al ratio for the catalyst, was precipitated with a sodium carbonate solution. The coprecipitation is leaded to a neutral pH. In these conditions the components are totally precipitating, thus, the Ni/Al ratio does not change. The precipitate is filtered many times with double distilled water until the disappearance of the Na^+ and $(NO_3)^-$ ions. Sodium ions in the catalyst are acting like a poison for many catalytic reactions. After this operation, the product is dried in stove at 105ºC.

By calcination at 340ºC, the mixture obtained by coprecipitation and drying is decomposed, leading to the formation of a mixture of nickel oxide with aluminum oxide. During calcination, a huge amount of gases (water vapors and carbon dioxide) are emitted, producing a very porous material with high specific surface area.

The reduction of the nickel oxide from the oxides mixture obtained by calcination was done by thermal treatment in strong hydrogen flow. The reduction of NiO is an autocatalytic process. It needs an induction period. It was shown that the energy used for removing oxygen from the free surface of nickel oxide is bigger than the energy needed for removing oxygen from those surfaces of nickel oxide that are in contact with metallic nickel [4,5]. The behavior of the reduction was studied by TPR and the results of this study are discussed in the following sections.

In the same way, the Ni/Cr_2O_3 and Ni/MgO catalysts were prepared. In these cases we used chromium nitrate and, respectively, magnesium nitrate instead of aluminum nitrate. The procedure for obtaining them is the same like that described for Ni/Al_2O_3 catalysts.

Experimental

1. TPR measurements

The TPR measurements were carried out on a home-made apparatus. This device is built up from more pieces. One of them is the gas source that gives a mixture of Ar and H_2 with 94.5 % volume of Ar and 5.5 % volume of H_2. The gas flow is divided in two parts. A part of the gas flow is conducted through the reaction chamber, is dried (using a molecular sieve) after leaving the reactor and is leaded to the thermal conductivity detector (catarometer). The second part of the gas flow is connected directly with the catarometer. For data acquisition, the catarometer is connected with a computer. The reaction chamber is connected to a temperature programmer. The limit temperature for measurements was 650°C. The measurements were carried out starting at room temperature.

2. Data acquisition system

The hardware part of the acquisition system, consist of a signal preconditioning module and a National Instruments NI-DAQ 6220 module. The NI module is an M series, PCI type of board. This board is simply inserted in a desktop PC without any other necessary adaptation. The unit as a whole uses only two channels, which are set as analog inputs. One measuring channel is dedicated to the acquisition of the differential voltage supplied by the catarometer. The other one does the acquisition of the oven's temperature, having the readings been corrected by a software linear regression. The block diagram of the preconditioning module is shown in fig.1.

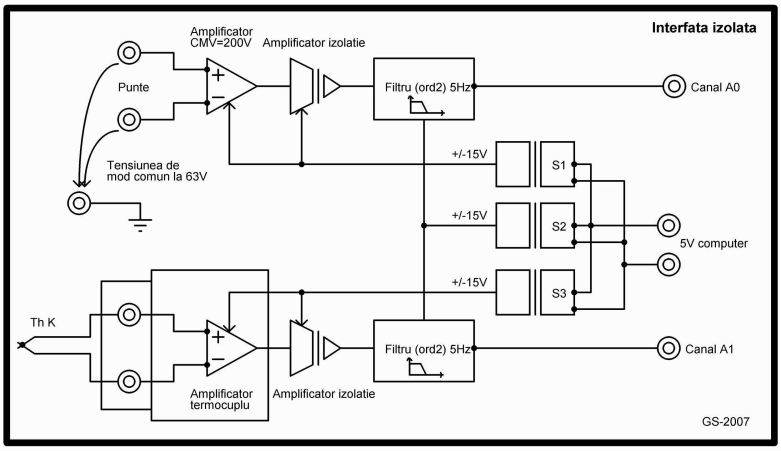

Fig. 1. Block diagram of the preconditioning module

Now, the main issue in using an acquisition board for any industrial or in laboratory application, is that the usually electrical grounding points are situated sometimes at a different voltage level. A much higher risk of damaging the acquisition board can be avoided, if the presence of the common mode level at the input is limited to a max. 10V; unfortunately the catarometer bridge generates a differential voltage which has a very high common mode voltage situated between 60 and 100V. All these issues are resolved by using a specially designed signal preconditioning module. This module guarantees that the acquisition board will record all signals at the same grounding potential and also adapts the high common mode signal to an appropriate input level.

The input of the preconditioning module which measures the catarometer bridge, acts as an impedance buffer and because of his special design, the INA117 unity-gain operational amplifier does withstand the high common mode voltage which might be up to 200V. A second operational amplifier is wired as an inverting amplifier which is set to a (V_{in})*5V voltage gain at the output. The temperature of

the oven is measured using a K type thermocouple for the entire 25°C to 800°C range. Using a proprietary AD595 thermocouple amplifier, it proved to be the best way of adapting the small signal provided by the thermocouple to the input of the acquisition board.

After the signal conditioning, both channels are using the ISO124 insulation amplifiers by means of separating the different measuring electrical groundings from the common ground of the acquisition NI-DAQ board.

Two second order unity-gain Sallen-Key type low pass filters, one for each channel are filtering out the switching noise generated by the insulation amplifiers. Another benefit of using these filters can be obtained if the cutting frequency is set to 5Hz. In that case the rejection of the mains frequency is about 40db at 50Hz. This is achievable mainly because the measured signals are having a very slow variation rate.

The preconditioning module is powered by the computer 5V power supply which is present on the NI-DAQ connector. Furthermore the galvanic separation is completed by using three separate +/-15V miniature 1W switching mode power supplies for powering all the above mentioned circuits.

We used the LabView8 platform mostly because is best fitted to our National Instruments acquisition board. Also the necessary developing time for a given application is greatly reduced because of the use of the “in software implemented modules”.

Results and discussion

For data analysis we used dedicated software developed and implemented by our research team. We were looking for the modifications in the temperatures specific for the maximum hydrogen consumption in different cases [6]. So, we collect data representing the reduction behavior of nickel oxide in the presence of some oxide supports. In fig.2a is represented the reduction behavior of pure nickel oxide without any other oxide used as support. From the first derivative of this spectrum, the value of the temperature where the hydrogen consumption has a maximum, at about 255ºC, was obtained. For the other samples, the values for the maximum hydrogen consumption are increased, as a sign of the influence of the support oxide on the reduction behavior of the nickel oxide.

The reduction behavior of nickel oxide in the presence of Cr_2O_3, Al_2O_3 and MgO are represented in fig.2b-d. The values for the maximum hydrogen consumption for the investigated samples are given in the Table 1. We can see that for reducing the NiO using MgO support we need higher temperature, about 373.3ºC, than in the case of pure NiO. This effect is caused by the presence of the MgO that interacts with the nickel oxide making NiO more stable and difficult to reduce. If we are looking at the temperature corresponding to the NiO reduction in the presence of chromium oxide, a higher value, of 385.5ºC, will be found. This means that the reduction of NiO

in this case occurs with higher energy consumption and the chromium oxide makes the NiO more stable than the MgO. In this case some chromites are formed during the calcination process and make the complete reduction of the NiO more difficult. A really significant difference in the temperature corresponding to the highest hydrogen consumption can be observed in the NiO deposed on alumina as support. The value for this case was 487.3ºC. In this case some aluminates can be produced. The reduction of the NiO involved in aluminates is difficult due to the high stability of these aluminates.

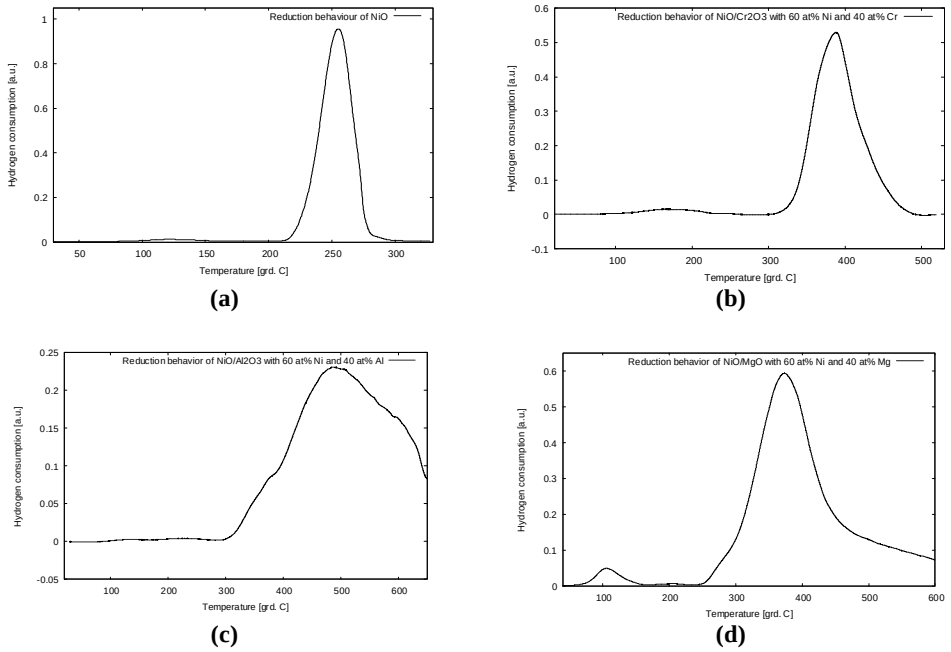

Fig. 2. The reduction behavior of NiO (a), NiO/Cr_2O_3 (b), NiO/Al_2O_3 (c) and NiO/MgO (d)

Table 1

The temperatures corresponding to the maximum hydrogen consumption (T_{max})

Sample	T_{max} (ºC)
NiO	**255**
NiO/Cr_2O_3	**387.5**
NiO/Al_2O_3	**487.3**
NiO/MgO	**373.3**

All the samples, excepting the pure NiO, have a concentration of 60 at% of nickel and 40 at% of the metal present in the support, respectively Cr, Al and Mg. We can see that it will be easier, from energetic point of view, to obtain nickel

catalysts supported on magnesium oxide and chromium oxide than to obtain nickel catalysts supported on alumina due to the fact that the temperatures needed for the reduction of the NiO in the presence of alumina is much higher than in the first two cases. This is a proof of oxide support influence on the reduction behavior. This influence is explained by interaction between nickel oxide and support oxide. This phenomenon was also evidenced in literature [7, 8].

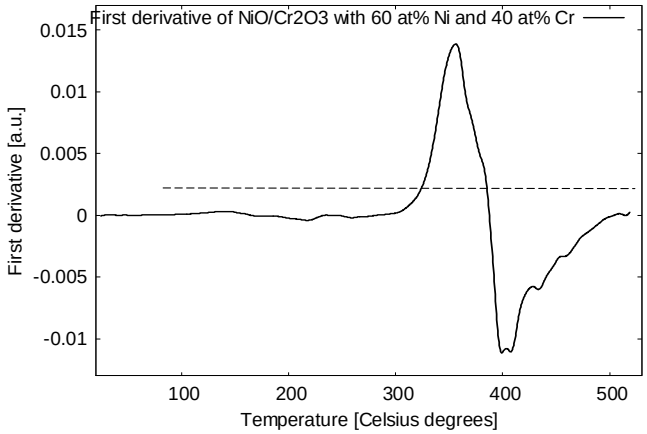

Fig. 3. The first derivative for the TPR spectra of NiO/Cr_2O_3

In fig.3 the first derivatives of the TPR spectra, corresponding to the NiO reduction using Cr_2O_3 as support, is represented. The zero value of the derivative corresponds to the maximum hydrogen consumption for this support.

Conclusions

The TPR spectra give important information regarding the reduction behavior of the NiO with different oxides used as support for the catalysts.

The difference in the temperatures corresponding to the maximum hydrogen consumption is a proof of the support influence in the reduction behavior and also in the catalytic activity of the samples. This influence is proved by the increasing of the temperature for maximum hydrogen consumption in the case of MgO, Cr_2O_3 and Al_2O_3 used as support. The increased temperatures are also an evidence of the nickel oxide –support oxide interaction.

REFERENCES

[1]. J. W. Niemantsverdriet, Spectroscopy in Catalysis, Wiley – VCH Verlag, 2007.

[2]. G. Munteanu, L.Ilieva, R.Nedyalkova, D.Andreeva, Applied Catalysis A: General 277, 31–40, 2004.

[3]. C.N. Satterfield, *Heterogeneous Catalysis in Industrial Practice*, McGraw-Hill, New York, 1991.

[4]. N.N. Bulgakov, V.V. Boldirev, Kin. Kataliz., 14, 1402, 1973.

[5]. B. Delmon, Bull. Soc. Chim. France., 590, 1961.

[6]. N. Aldea, F. Aldea, *Tehnici de analiza semnalelor fizico-chimice*, Ed. Risoprint Cluj-Napoca, 2001.

[7]. S. J. Tauster, S.A. Stevenson, J.A. Dumesic, G.B. Raupp, R.T.K. Baker, in S.A. Stevenson, J.A. Dumesic, R.T.K. Baker, E. Ruckenstein (eds), *Metal-Support Interactions in Catalysis, Sintering and Redispersion*, Van Nostrand, New York, 1987.

[8]. N. Aldea, B. Barz, A.C. Gluhoi, P. Marginean, X. Yaning, H. Tiandou, L. Tao, Zhonghua Wu, Z. Wu, Journal of Optoelectronics and Advanced Materials, 6 (4), 1287-1296, 2004.

STUDIA UNIVERSITATIS BABEŞ-BOLYAI, PHYSICA, LIII, 2, 2008

THE EFFECT OF ZrO_2 AND ZrO_2-SiO_2 NANOSTRUCTURED FILLER PARTICLES ON POLYMERIC COMPOSITES FOR THIN DENTAL COATINGS

CAMELIA ALB[1], MARIOARA MOLDOVAN[2], CRISTINA PREJMEREAN[2], DOINA PRODAN[2], MARCELA TRIF[2], CODRUTA SAROSI[2], LAURA SILAGHI-DUMITRESCU[2], VIOLETA PASCALAU[2]

ABSTRACT. Polymeric composite films for dental applications are synthesized and characterized with respect to their structural properties. The composite samples consist of polymers including as reinforcement phase inorganic nanostructured particles. The key to realize dental composites having adequate properties is the homogenous dispersion in the polymer matrix of a low content of inorganic nanoparticles. Dental fillers based on resin composites reinforced with ZrO_2 and SiO_2 were obtained by hydrothermal methods. The crystal sizes identified in the ZrO_2 and SiO_2 – ZrO_2 inorganic phases are ranging from 4 nm to 50 nm. By introducing different ratios of the synthesized nanostructured fillers into a dimethacrylic organic matrix we have realized films using UV and visible initiatory system. The adherence of these films on dental device substrate depend on their structural properties.

Keywords: Polymeric composite films, nanostructured fillers, dental coatings

Introduction

Many of the actual researches are centered upon three main directions: modification of the nature of the filling materials; development of the polymerization systems; improvement of mechanical properties of the composite materials by increasing the quantity of filler involved in composite following the advantages of an adequate distribution of the particles' sizes and of some proper form of the filling particles [1-4]. Two of these research directions aim the filling systems, which enter in the composite material. The choice of some proper inorganic materials aims, by their chemical nature (composition, structure and properties) to suit to the requirements of the composite and, in the same time it is enforced the knowledge of the form and the size of the particles, of their granulometric distribution, of the physical-chemical state of the inorganic particles' size, their variations influencing in an obvious way the composites' properties [5-9]. The results of the literature studies traced the new tendencies in the domain, namely, the decreasing of the particles'

[1] *Hatieganu University of Medicine and Pharmacy, Cluj-Napoca, Romania*
[2] *BabesBolyai University, Raluca Ripan Institute for Research in Chemistry, Cluj-Napoca, Romania*

size in the same time with the increasing of the including degree in the composite mixture, in the view of reaching the best performances. The obtaining key of some superior properties at the inorganic low includes is homogenous dispersion of nanometric sizes of inorganic phase in polymer, and creation of some favorable interactions at the organic/inorganic interface. The favorable interfacial chemistry leads to dispersion of organic and inorganic phases at a nanometric stage. The use of a low inorganic content leads to significant advantages. In case of a much lower inorganic content, as compared with that of ionomer polymers with glass, there are obtained high degrees of hardness, properties of force and barrier. Thus there are obtained significant reductions of the weight.

Materials and methods

The inorganic phase of the investigated samples consists of ZrO_2 based nanostructured particles. The most utilized method for obtaining this type of particles is the sol-gel method. ZrO_2 filler particles with a granulation up to 1 μm and with specific weight ρ = 2,45 g/cm^3 have been obtained from $ZrOCl_2 \cdot 8H_2O$ (Aldrich) and bidistilled water, using for neutralization 25% NH_3 solution. The thermal treatment was performed up to 900°C. Nanostructured particles of $SiO_2 - ZrO_2$ type, with ρ=2,87g/cm^3, were obtained from a combination of an organic or aqueous dispersion (sol of colloidal silica) with an aqueous or organic dispersion (sol of microparticles of zirconium oxide) with thermal treatment up to 1000°C.

The organic matrix comprises Bis-GMA; HEMA (2-hydroxi-methacrylate), TEGDMA (triethyleneglycol dimethacrylate) and 1,3 Glycidopropyl-thetramethyl-disiloxan Different percents from these monomers were used, and two initiation systems: photoinitiatory in visible domain and initiatory in UV domain. In case of photopolymerization in visible domain, it was used the system CQ (camphorquinone)/ DMAEM (dimethylamine methylmethacrylate). In the case of photopolymerization in UV domain it was used p-methoxybenzoil diphenylphosphynoxide as initiator with DMAEM. The representation of the monomers used in the organic matrix of the investigated composites is given bellow.

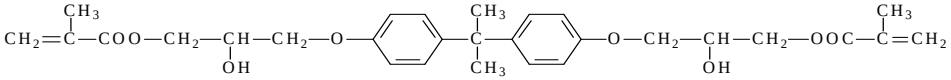

Bis-GMA

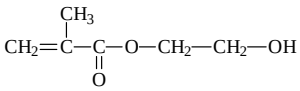

HEMA

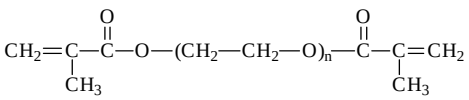

TEGDMA

The films were prepared with the synthesized nanostructured fillers added in different proportions to an organic dimethacrylic matrix with UV and visible initiatory system. In Table 1 is given the composition of these films.

Table 1.

Composition of the obtained films.

COD	ORGANIC MATRIX					FILLERS
	HEMA	**Bis-GMA**	**TEGDMA**	**1,3-Glicidopropyl-thetrametyldisiloxan**	**Initiation system**	
F1	35	65	-	-	Visible	ZrO_2–1%
F2	-	45	35	20	UV	ZrO_2–5%
F3	25	65	-	10	UV	ZrO_2 – 10%
F4	-	50	50	-	Visible	ZrO_2-SiO_2–15%
C5		65	35	-	Visible	ZrO_2-SiO_2–50%
C6	45	55	-	10	UV	ZrO_2-SiO_2–25%
F7	35	65	-	5	UV	ZrO_2 – 5%
C8	-	65	35	-	Visible	ZrO_2-SiO_2–55%

The Brunauer, Emmett and Teller (BET) method was used to determine the specific surface area of the inorganic oxide fillers. For identification of the oxide materials structure we used the technique of X ray diffraction on crystalline fillers. Diffractograms of the oxide compounds synthesized were registered on standard X ray equipment, BURUKER *Advance* type. Gathering of diffraction information was accomplished by "step by step" method, in angular steps of 0.02 degrees. We used Cu K_α (λ_{Cu}=*1.5406* Å) radiation with a Ni filter for eliminating the component Cu K_β. The experimental registrations were carried out in the angular diffraction domain 2θ = 15 - 60 degrees. The morphological examination of the microparticles, as well as the of the composite films was made by scanning electron microscopy (SEM) on a TESCAN equipment.

Results and discussion

The experimental diffractograms for ZrO_2 sample thermal treated at 110^0C and at 900^0C are shown in Figure 1. After the thermal treatment applied at 110^0C are evidenced diffraction lines occurring from $ZrOCl_2$ and $ZrOCl_2 \cdot 8H_2O$ crystals [10, 11] which are still present from the precursor used in the sol-gel synthesis of the fillers. By applying the thermal treatment at 900^0C, the structure of the filler is modified and in this case lines typical for ZrO_2 dominate the diffraction pattern, but also diffraction peaks typical for ZrO crystals [12] are recorded close to 34^0, 40^0 and 56^0.

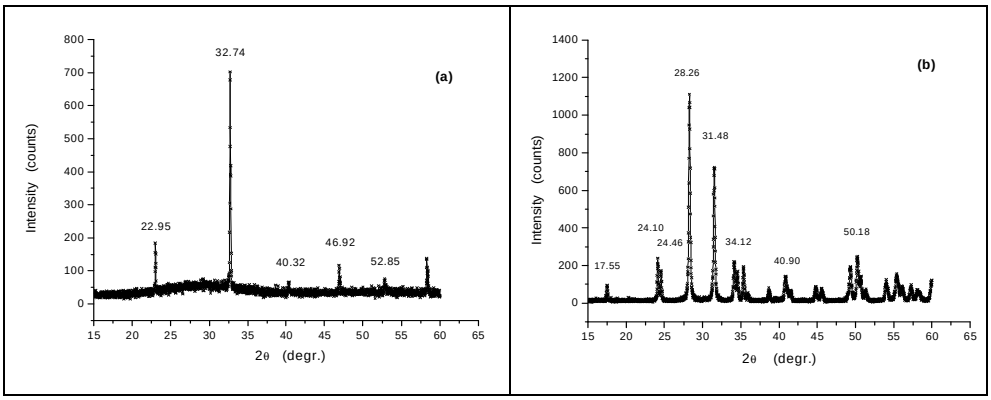

Fig. 1. Diffractograms of ZrO_2 filler thermal treated at 110^0C (a) and at 900^0C (b).

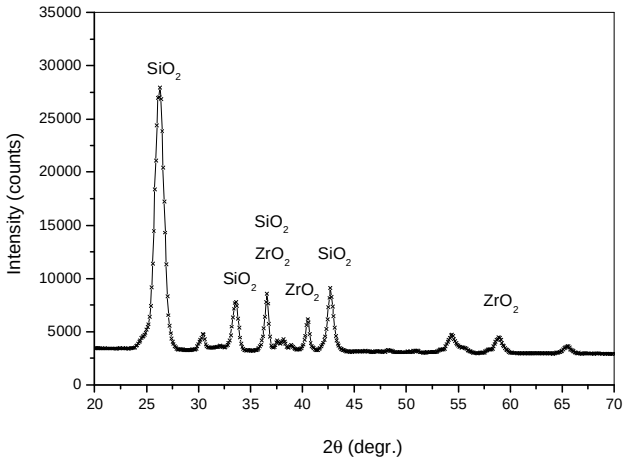

Fig. 2. Diffractogram for SiO_2-ZrO_2 filler thermal treated at 1000 ^{0}C.

The diffractogram of the SiO_2-ZrO_2 compound (Fig. 2) presents a main maximum at 26.3^0, in accordance with a crystalline matrix of SiO_2. The thermal treatment at the temperature of 1000°C determined the appearance of ZrO_2 crystallites (PDF 7-337). For the SiO_2 crystalline compound (PDF 11-695) the main diffraction maxima are at 26.15^0, with interplanar distance of 4.04 Å, at 33.65^0, with interplanar distance of 2.84 Å, and at 42.75^0 for interplanar distance of 2.45 Å. The sizes of crystallites estimated from the diffraction maxima width are in the range 4-50 nm.

BET measurements show for the ZrO_2 nanostructured particles the specific surface area of 58 m^2/g and for SiO_2 – ZrO_2 nanostructured particles a specific surface area of 78m^2/g.

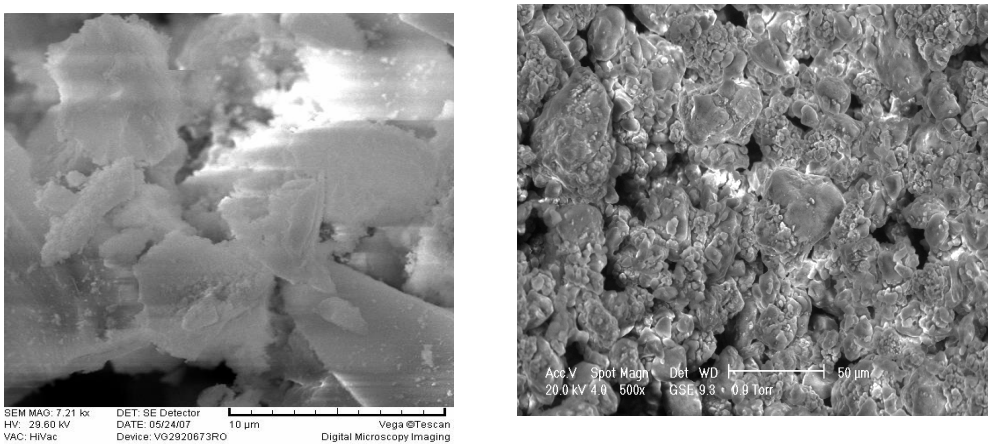

(a) (b)

Fig. 3. Electron micrographs of F3 and F4 composite films containing ZrO_2 (a), SiO_2-ZrO_2 (b) fillers.

The SEM images presented in Figure 3 for ZrO_2 and ZrO – SiO fillers indicate an irregular morphology on the surface of the samples. The crystalline forms are most pronounced for the ZrO_2 containing filler, in agreement with the X ray diffraction results.

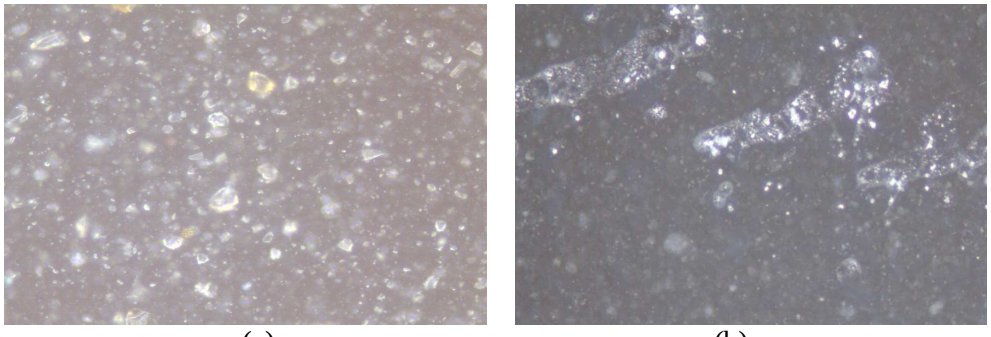

(a) (b)

Fig. 4. Optic microscopies of the F3 and F4 polymeric composites with ZrO_2 (a) and SiO_2-ZrO_2 (b) fillers

Due to these irregular forms, the approaching of the particles at the dispersal of the inorganic filler in the organic matrix is encumbered and between particles will occur uneven spaces which can be filled with much smaller size particles (Fig. 4), that will lead to a better package of the fillers in the polymer matrix.

The ZrO_2-SiO_2 based films show a better adherence than the SiO_2 based films on the dental device substrates. This behavior is directly related to the structure, porosity and specific surface area of the polymeric composite films used in thin dental coatings.

Conclusions

According to the results obtained by X-ray diffraction analysis, both ZrO_2 and ZrO_2-SiO_2 inorganic phase introduced into the investigated dental composite films are nanostructured The electron microscope images point out that the composite films with ZrO_2 fillers present large micropores, while by adding of ZrO_2-SiO_2 fillers, with higher specific surface area, the micropores are much finer. The adherence tests of these films on dental device substrates prove that the ZrO_2-SiO_2 fillers ensure an increased adherence compared to the thin films reinforced with ZrO_2 fillers.

REFERENCES

1. F. Kaeble, ed., Handbook of X-Rays, Ed. Emmelt, McGraw-Hill Book Company, New York,1967
2. P. Behrens, Trends Anal. Chem., 11, 237 (1992)
3. M. Vallet–Regi, J. Mater. Chem., 7, 1017 (1997)
4. P.D. Batista, M. Mulato, C. F. de O. Graeff, F. J. R. Fernandez, F. das C. Marques, Braz. J. Phys., 36, 478, (2006)
5. W. Huang, J. Shi, J. Sol-Gel Sci. Techn., 20, 145 (2001)
6. A.K. Tyagi, G. Mangamma, M. Kamruddin, S. Dash, B. Raj, J. Nanosci. Nanotechnol., 7, 2005 (2007)
7. J.D. Woodward, J.M. Pickel, L.M. Anovitz, W.T. Heller, A.J. Rondinone, J. Phys. Chem. B, 110, 19456 (2006)
8. O.V. Sakhno, L.M. Goldenberg, J. Stumpe, T.N. Smirnova, Nanotechnology, 18, 105704 (2007)
9. Y. Yang, M. Guo, M. Yang. Z. Wang, G. Shen, R. Yu, Int. J. Environ. An. Chem., 85, 163 (2005)
10. L.M. Seaverson, J.D. Corbett, Inorg. Chem., 22, 3202 (1983)
11. T.C.W. Mak, Can. J. Chem., 46, 3491 (1968)
12. N. Schoenberg, Acta Chem. Scand., 8, 627 (1954).